Breaking Barriers: Evaluating GSK-3 Inhibition as a Dual Therapeutic Strategy in Diffuse Midline Glioma Models

Jasmine Sharee Clark

B.S., Old Dominion University, 2020

A dissertation submitted in partial fulfillment of the requirements for the degree of Doctor of Philosophy in the Division of Therapeutic Sciences at Brown University

Providence, Rhode Island

May 2026

This dissertation by Jasmine S. Clark is accepted in its present form by the Molecular Pharmacology and Physiology program, as satisfying the dissertation requirement for the degree of Doctor of Philosophy.

Date: _____

DocuSigned by:
Sean Lawler
6A2688E8BBC5498...
Sean Lawler, PhD, Advisor

Recommended to the Graduate Council

Date: _____

Signed by:
Sarah Delaney
7542E0BF637D433...
Sarah Delaney, PhD, Reader

Date: _____

Signed by:
Carolina Haass-koffler
802CAB0C4E3C408...
Carolina Haass-Koffler, PharmD, PhD, Reader

Date: _____

Signed by:
Diane Hoffman-kim
7F133B86F8544C9...
Diane Hoffman-Kim, PhD, Reader

Date: _____

Signed by:
Anke Bruning-Richardson
B4D45F627E98493...
Anke Brüning-Richardson, PhD, Reader

Approved by the Graduate Council

Date: _____

David Lindstrom, PhD, Dean of the Graduate School

Curriculum Vitae

EDUCATION

Ph.D. Candidate | *Brown University, Providence, RI*

Legorreta Cancer Center, Department of Pathology and Laboratory Medicine, Molecular Pharmacology and Physiology Program | 2021-Anticipated 2026

Mentor: Sean Lawler

B.S. in Chemistry | *Old Dominion University, VA* | 2018-2020

B.S. in Chemistry | *Norfolk State University, VA* | 2016-2018

SKILLS

Communication & Leadership:

- Experienced in leading graduate student organizations, coordinating large-scale events, and managing executive board activities.
- Skilled in mentoring undergraduate and master's students, guiding independent research projects from design through data analysis.
- Designed and delivered curriculum for a summer Stem Cell and Regenerative Biology course over three consecutive years, blending lecture and lab instruction.
- Collaborated effectively in cross-functional, interdisciplinary research teams
- Skilled at translating complex scientific concepts into accessible presentations for diverse audiences.

Data Analysis & Software:

- Proficient in GraphPad Prism, FlowJo, ImageJ/Fiji, SynergyFinder, and Python for data visualization and analysis.

- Experienced in large-scale data interpretation (RNA-seq, kinase arrays) and quantitative imaging analysis.

Research & Technical Writing:

- Authored/co-authored peer-reviewed publications and abstracts presented at national conferences.
- Skilled in experimental design, protocol optimization, and manuscript preparation.
- Experienced in developing grant/fellowship applications and scientific presentations tailored to different audiences.

Laboratory Techniques:

- **Cell culture**: Adherent, suspension, and co-culture systems (BBB/BTB spheroids); plasmid DNA transfection, and lentiviral transduction.
- **Molecular biology techniques**: RNA extraction, Western blotting, and protein expression analysis
- **Imaging**: Confocal, live-cell, and fluorescence microscopy.
- **Specialized assays**: Scratch and Transwell migration/invasion, tube formation, viability (CellTiter-Glo, IncuCyte Cytotox, MTT), BBB/BTB permeability (dextran/antibody uptake), and ECIS for barrier integrity.
- ***In Vivo* models**: Zebrafish vascular formation, blood flow dynamics, and small-molecule pharmacological testing.

RESEARCH EXPERIENCE

Ph.D. Researcher | *Brown University, Providence, RI* | 2021-Present

Dissertation Focus: Targeting the Blood-Brain Barrier for the Treatment of Pediatric High-

Grade Glioma.

- Characterized the effects of GSK3 inhibition on mechanisms driving therapeutic resistance, invasion, angiogenesis, and blood–brain barrier permeability to identify potential therapeutic strategies for pediatric high-grade glioma.
- Designed and optimized assays across multiple platforms, including cell viability assays (CellTiter-Glo, MTT, IncuCyte), scratch and Transwell migration/invasion assays, 3D BBB/BTB spheroid development, and angiogenic tube formation.
- Applied molecular techniques such as western blotting, kinase arrays, and RNA-seq to probe mechanisms of therapy response.
- Collaborated with clinicians and translational scientists to align preclinical models with therapeutic goals and contributed to manuscripts and presentations at national conferences.
- Mentored undergraduate and master's students in independent projects, training them in cell culture, assay design, and data interpretation.
- Contributed to manuscripts and abstracts presented at national conferences and prepared figures for peer-reviewed publication.

Clinical Trial Research Rotation | *Rhode Island Hospital, Providence, RI* | 2024

- Completed a clinical research rotation under physician mentorship, observing patient engagement during treatment decisions, trial option discussions, and overall clinical trial operations.
- Gained firsthand understanding of how trial protocols are communicated to patients and how physicians navigate treatment and trial options.

Summer Research Intern | *Naval Research Laboratory, Washington, DC* | 2020

- Investigated 2D materials for quantum sensing and computing applications through literature reviews and computational data analysis.
- Assisted in summarizing and evaluating material properties to guide future experimental directions.

Summer Undergraduate Researcher | *Stony Brook University, Long Island, NY* | 2019

- Conducted *in vitro* cytotoxicity assays to evaluate the anticancer potential of novel vanadium-based complexes.
- Gained proficiency in mammalian cell culture, compound preparation, and dose-response analysis.
- Generated data on compound efficacy and toxicity that contributed to ongoing projects in transition metal-based drug development.

Undergraduate Researcher | *Old Dominion University, Norfolk, VA* | 2018-2020

- Synthesized and structurally characterized novel vanadium antibacterial complexes for chemotherapeutic development.
- Conducted cytotoxicity assays and *in vitro* drug studies in triple-negative breast cancer cell lines.
- Presented findings at national meetings and contributed to a peer-reviewed publication in the *Journal of Inorganic Biochemistry*.

TEACHING EXPERIENCE

Instructor | *Brown University, Providence, RI* | 2022-Present

- Designed and taught a summer course on stem cell and regenerative biology for high school students.

- Balanced lecture, lab-based experiments, and discussion-based learning to engage ~20 students annually.
- Provided individualized feedback and mentorship, fostering student engagement and mastery of complex biological concepts.

Teaching Assistant | *Brown University, Providence, RI* | Fall 2022

- Supported instruction in an introductory undergraduate physiology course, providing academic support to ~60 undergraduate students.
- Led review sessions, clarified core concepts, and supported assessment through exam proctoring and grading.
- Contributed to creating an engaging and supportive learning environment for diverse student learners.

Tutor | *Norfolk State University, Norfolk, VA* | 2017-2018

- Delivered one-on-one tutoring in chemistry and math for Honors College peers, strengthening student understanding and academic performance.
- Cultivated skills in personalized instruction, adapting approaches to diverse learning needs.

LEADERSHIP & OUTREACH

Commencement Graduate Assistant | *Brown University* | 2025

- Supported the coordination and delivery of Master's and PhD commencement ceremonies by managing event logistics, student services, and guest engagement.
- Collaborated with university staff and faculty to ensure an organized, professional, and inclusive ceremony experience for graduates and their families.

President | *Samuel M. Nabrit Black Graduate Student Association, Brown University* | 2023-2024

- Led an executive board and oversaw organizational strategy, planning, and execution of initiatives to strengthen the graduate student community and foster inclusivity.
- Chaired general body meetings to engage members, communicate organizational priorities, and encourage active participation.
- Organized large-scale campus events and networking programs that enhanced community engagement and aligned with graduate student needs.
- Built collaborations with other graduate student organizations, faculty, the Student Activities Office, and the Office of Diversity, Equity, and Inclusion to co-sponsor programming and expand organizational reach.
- Advocated for diversity, equity, and accessibility within the graduate community by partnering with university leadership and external speakers.

Education Chair | *Samuel M. Nabrit Black Graduate Student Association, Brown University* | 2024-2025

- Developed and implemented academic support programs, including structured study halls, to promote graduate student success.
- Coordinated speaker events and workshops that highlighted educational and professional pathways for underrepresented students in STEM.
- Delivered academic and professional resources to peers, reinforcing the organization’s mission to promote student success and equitable opportunities.

- Collaborated with other student groups, faculty, and university offices to expand programming reach and strengthen institutional support for diversity and inclusion.

Graduate Orientation Assistant | *Brown University* | 2023-2025

- Assisted with planning, organization, and execution of orientation events, supporting the successful transition of incoming graduate students into academic and social communities.
- Served as a point of contact for new students, providing guidance on resources and fostering a welcome and inclusive environment.

Therapeutic Sciences Graduate Program Diversity and Inclusion Action Plan (DIAP) Committee Member | *Brown University* | 2022

- Collaborated with faculty and students to develop initiatives promoting diversity, equity, and inclusion across the graduate program.
- Contributed to the development of program climate surveys, student engagement strategies, and inclusive academic and social programming.
- Proposed and supported initiatives such as peer mentoring, cross-program activities, and outreach to underrepresented student groups.

AWARDS & HONORS

- NIH Research Supplement Award, Brown University, 2022-2024
- Helen Fitzgerald Cserr Memorial Fund Pre-doctoral Fellow, 2022-2023
- NIH T32 Training Grant, Therapeutic Sciences Graduate Program, Brown University, 2021-2022
- Undergraduate Researcher of the Month, Old Dominion University, 2020

- Maximizing Access to Research Careers (MARC) Trainee (NIH-funded), Old Dominion University, 2018-2020
- Honors College Scholar, Norfolk State University, 2016-2018

PUBLICATIONS

- Jimenez-Macias, J.L.; Vaughn-Beaucaire, P.; Bharati, A.; Xu, Z.; Forrest, M.; Hong, J.; Sun, M.; Schmidt, A.; **Clark, J**.; Hawkins, W.; Mercado, N.; Real, J.; Huntington, K.; Zdioruk, M.; Nowicki, M.O.; Cho, C.F.; Wu, B.; Li, W.; Logan, T.; Manz, K.E.; Pennell, K.D.; Fedeles, B.I.; Brodsky, A.S.; Lawler, S.E. "Modulation of blood-tumor barrier transcriptional programs improves intra-tumoral drug delivery and potentiates chemotherapy in GBM." *Sci. Adv.* 2025, 11(9), eadr1481. https://doi.org/10.1126/sciadv.adr1481
- Beebe, S.J.; Celestine, M.J.; Bullock, J.L.; Sandhaus, S.; Arca, J.F.; Cropek, D.M.; Ludvig, T.A.; Foster, S.R.; **Clark, J.S**.; Beckford, F.A.; Tano, C.M.; Tonsel-White, E.A.; Gurung, R.K.; Stankavich, C.E.; Tse-Dinh, Y.-C.; Jarrett, W.L.; Holder, A.A. "Synthesis, characterization, DNA binding, topoisomerase inhibition, and apoptosis induction studies of a novel cobalt(III) complex with a thiosemicarbazone ligand." *J. Inorg. Biochem.* 2020, 203, 110907. https://doi.org/10.1016/j.jinorgbio.2019.11090
- Jimenez-Macias, J.L.; Vaughn-Beaucaire, P.; Yan, J.; **Clark, J.**; Lawler, S.E. "Decoding the biology of the blood-brain tumor barrier in brain cancer." Submitted to *Mol. Cancer Res.* (AACR)

- **Clark, J**; Vaughn-Beaucaire, P; Lawler, S.E. “Investigating GSK3 Inhibition as a Therapeutic Strategy in Pediatric High-Grade Glioma Models.”

CONFERENCES AND SYMPOSIUMS

- 2025 Society of Neuro-Oncology Annual Meeting, Honolulu, HI (P)
- 2025 Therapeutic Sciences Graduate Program Annual Retreat, Providence, RI (P)
- 2024 Society of Neuro-Oncology Annual Meeting, Houston, TX (P)
- 2024 American Association for Cancer Research Annual Meeting, San Diego, CA (P)
- 2024 Therapeutic Sciences Graduate Program Annual Retreat, Providence, RI (P/T)
- 2023 Society of Neuro-Oncology Pediatric Research Conference, Washington, DC (P)
- 2022 Therapeutic Sciences Graduate Program Annual Retreat, Providence, RI (T)
- 2020 Old Dominion University Undergraduate Research Symposium, Norfolk, VA (P)
- 2019 Annual Biomedical Research Conference for Minority Students (ABRCMS), Anaheim, CA (P)
- 2019 American Chemical Society National Meeting & Exposition, Orlando, FL (P)
- 2019 Old Dominion University Undergraduate Research Symposium, Norfolk, VA (P)

Preface and Acknowledgments

To my undergraduate mentor, Dr. Holder, thank you for opening the door to research and showing me the joy of discovery. Your mentorship, patience, and belief in me were the roots of everything that followed. You taught me how to think like a scientist, and I am grateful for your continued support and guidance.

To Sean and my current lab, thank you for your support, guidance, and encouragement through every late night, experiment, and brainstorming session. I've grown immensely under your mentorship, and I'm so grateful for my time with you all at Brown. A huge shout-out to Pip and Michelle, my lab girlies! I'm incredibly grateful to have been able to complete this journey alongside both of you. Thank you for all the laughs and chaotic experiment crossovers, you both have made even the hardest days lighter.

To my parents, thank you for providing Sonny and me with every opportunity possible. You always stressed the importance of education and hard work, and I am so blessed that God chose the two of you to be my parents. Everything I am is because of your never-ending love and support. To my favorite brother Sonny, thank you for being my built-in best friend for as long as I can remember. I wouldn't have wanted to go through life with any other brother but you. Thanks for all the laughs and adventures, and I can't wait to see what else we get into. I love you guys so much.

To Marcus, my love and partner, you have been the best part of this journey. You were the very first person I met at orientation, and you've seen me through this from

beginning to end. You make life exciting and fun with your humor and spontaneity, and I love waking up every morning next to you. Thank you for always believing in me and encouraging me throughout this entire journey, even when I have doubted myself. Thank you for loving me just as I am and for your endless support as my greatest friend and the love of my life. You've shown me what it truly means to be loved unconditionally. I love you, baby.

To my Stedman Loft baddies, Fiji, Lawrenzo, Morgan, and Gaddy, you turned this last year into something I'll never forget. The game nights, spontaneous adventures, and pure chaos make every day interesting and fun. I love you all more than you know. My girls, Morg and Gaddy, I love you both deeply, even though you are both much more dramatic than I am (truly a skill). You're both stuck with me for life, so congratulations... we really found each other and made it everyone else's problem.

To my lab neighbor and my girl Anna, thank you for being such an incredible friend and for always being there. You have been an incredible addition to my time here at Brown. To my sisters, my forever support system, thank you for your endless love and belief in me.

And finally, to all my friends from every stage of life: thank you for keeping me grounded, reminding me to laugh, and helping me hold onto myself through it all. You made this journey bearable and beautiful, and I carry your love with me always.

This dissertation is dedicated to my late Nana, my angel, and my sweet Papa. Your love, warmth, and wisdom continue to guide every step I take. I love you both so much, and I hope I've made you proud.

Table of Contents

Curriculum Vitae iv

Preface and Acknowledgments xiii

List of Illustrations and Figures xviii

List of Tables xx

CHAPTER 1: INTRODUCTION 1

1.1 Pediatric high-grade gliomas 2

1.2 Diffuse Midline Glioma 3
1.2.1 Epidemiology, clinical features, and prognosis 3
1.2.2 Diffuse Midline Glioma H3K27M: Biology and molecular drivers 5
1.2.3 Therapeutic challenges and unmet clinical needs 7

1.3 Mechanisms driving therapeutic resistance in glioma 8
1.3.1 Proliferation, invasion, and vascular remodeling 8

1.4 Glycogen synthase kinase-3 (GSK-3) signaling in glioma biology 10
1.4.1 GSK-3 and Canonical Pathways of Cancer 11
1.4.2 GSK-3 inhibitors 13

1.5 Indirubin derivatives as multi-kinase inhibitors 15

1.6 Rationale for GSK-3 as a therapeutic target for Diffuse Midline Glioma 17

1.7 BBB and BTB in glioma therapy 18
1.7.1 BBB 18
1.7.2 The BTB in high-grade brain tumors 19
1.7.3 Biology of endothelial cell-adhesion molecules in the BTB 20
1.7.4 The biology of the BTB in DMGs 22

1.8 Project Rationale, aims, and objectives 25
1.8.1 Rationale/Gap Summary 25
1.8.2 Central hypothesis 26

CHAPTER 2: MATERIALS AND METHODS 27

2.1 Cell lines and culture media 28
2.1.1 High-grade glioma cell lines 28
2.1.2 Endothelial and supporting cell lines 31
2.1.3 Cell culture and passaging 31

2.2 Compounds, reagents, and antibodies 32
2.2.1 Compounds and reagents 32
2.2.2 Antibodies 35

2.3 Experimental methods for Chapter 3 36

2.4 Experimental methods for Chapter 4 41

2.5 Experimental methods for Chapter 5 44

2.6 Data Analysis and Quantification 49

CHAPTER 3: DIFFUSE MIDLINE GLIOMA BIOLOGY 50
3.1 Overview and Significance 51
3.2 Results 52
3.3 Chapter 3 Summary and Discussion 69
CHAPTER 4: ENDOTHELIAL CELL BEHAVIOR AND BBB PERMEABILITY 73
4.1 Overview and Significance 74
4.2 Results 75
4.3 Experimental models of the BTB 84
4.4 3D BBB/BTB co-culture models 91
4.5 Chapter 4 Summary and Discussion 99
CHAPTER 5: DRUG SCREENING AND MECHANISTIC STUDIES 102
5.1 Overview and Significance 103
5.2 Results 104
5.3 Chapter 5 Summary and Discussion 114
CHAPTER 6: OVERALL DISCUSSION AND CONCLUSIONS 117
6.1 Overall Discussion and Conclusions 118
Appendices 125
References 144

List of Illustrations and Figures

Figure 1.1: Mutation landscape of pediatric high-grade gliomas. 3

Figure 1.2: MRI imaging of an 8 year-old girl with a DIPG tumor (white arrows). 5

Figure 1.3: Diagram of the H3K27M mutation and H3G34R/V mutation. 7

Figure 1.4: Diagram of GSK-3β pathway inactivation 13

Figure 1.5: Schematic of the contrasting cellular composition of the BBB and the BTB in CNS malignancies. 21

Figure 1.6: Schematic of the overall central hypothesis. 26

Figure 2.1: Immunofluorescence staining of pediatric high-grade glioma (pHGG) cell lines (SU-DIPG XXXVI, SF8628, and KNS42). 29

Figure 2.2: Schematic of the Scratch wound-healing assay 40

Figure 3.1: Real-time proliferation kinetics on pHGG cell lines. 54

Figure 3.2: 72-hour endpoint dose-response comparison reveals BIA's superior potency across pHGG subtypes. 56

Figure 3.3: IncuCyte Phase-contrast images of pHGG cell lines. 59

Figure 3.4: Proliferation IC_{50} curves in pHGG cell lines. Real 60

Figure 3.5: CTG viability IC_{50} curves across pHGG cell lines. 62

Figure 3.6: Cell cycle analysis using propidium iodide via flow cytometry 64

Figure 3.7: Wound-healing Scratch assay Images. 66

Figure 3.8: Wound-healing Scratch assay 67

Figure 3.9: Transwell migration assay of DMG cell lines. 68

Figure 4.1: CTG viability IC_{50} curves for hCMECs with BIA and C91 compared to pHGG cell lines. 77

Figure 4.2: Scratch and Transwell migration assays on hCMEC/D3. 80
Figure 4.3: Tube Formation assay on HBMEC cells at 12 hours. 82
Figure 4.4: Barrier function assay on monolayer hCMEC/D3 cells using ECIS. 84
Figure 4.5: Experimental models of the BTB. 91
Figure 4.6: BBB/BTB Spheroid Cell Organization. 94
Figure 4.7: FITC-conjugated dextran (70kDa) and AlexaFluor-488 IgG permeability assay in BBB spheroids. 96
Figure 4.8: FITC-conjugated dextran (70kDa) and AlexaFluor-488 IgG permeability assay in BTB spheroids. 98
Figure 5.1: Schematic of High-throughput drug screening of the FDA-approved drug library in combination with 1 μM BIA. 105
Figure 5.2: High-throughput drug screening of 176 FDA-approved chemotherapeutics in combination with 1 μM BIA. 106
Figure 5.3: CTG viability IC_{50} curves for pHGG cell lines with BIA in combination with Vorinostat (SAHA). 108
Figure 5.4: CTG viability IC_{50} curves for pHGG cell lines with BIA in combination with Gemcitabine. 109
Figure 5.5: Canonical WNT/β-Catenin Signaling pathway active with BIA and C91 treatment. 112
Figure 5.6: Canonical WNT/B-Catenin Signaling pathway active with BIA and C91 treatment. 113
Supplementary Figure 5.1 Full Drug Screen Reports 126

List of Tables

Table 1: Tumor Stem Medium (TSM) Base 29

Table 2: Working TSM 1X (TSM base + Growth Factors) 30

Table 3: Compounds and reagents 34

Table 4: Primary and Secondary Antibodies 35

CHAPTER 1: INTRODUCTION

Blood-brain and blood-tumor barrier content adapted from Jimenez-Macias JL, Vaughn-Beaucaire P, Yan J, **Clark J**, Lawler SE. "Decoding the biology of the blood-brain tumor barrier in brain cancer." Accepted, Molecular Cancer Research (AACR), 2026, on which I contributed to figure generation and writing of the DMG/BTB background section.

1.1 Pediatric high-grade gliomas

Central nervous system (CNS) tumors are the most common solid neoplasms and the leading cause of cancer-related deaths in children, resulting in the highest morbidity and mortality compared to any other pediatric tumor type [1-4]. Pediatric gliomas are biologically distinct from their adult counterparts, which are typically characterized by IDH mutations (isocitrate dehydrogenase) that alter cellular metabolism, EGFR amplifications, and PTEN deletions, whereas pediatric high-grade gliomas are primarily driven by histone H3 mutations [5-7]. Pediatric high-grade gliomas (pHGGs) account for 20% of pediatric CNS malignancies however, despite their low incidence, they account for over 40% of all fatalities due to their aggressive biology [4,8]. The 2021 WHO Classification of Tumors of the Central Nervous System (CNS) defined 4 distinct subtypes of pHGG based on their own epigenetic mutations and modifications, all CNS Grade IV (Infant type: Grade 3 or 4) (**Fig.1.1**): 1. Diffuse Midline Gliomas, H3K27-altered, 2. Diffuse Hemispheric Glioma, H3G34-mutant, 3. Diffuse pediatric -type high-grade glioma, H3-wildtype and IDH -wildtype, and 4. infant-type hemispheric glioma [9-11]. Diffuse hemispheric gliomas, H3G34-mutant, are found predominantly in adolescents and young adults [12]. Diffuse pediatric-type high-grade glioma, H3-wildtype, and IDH-wildtype occur in both children and young adults, typically in the brainstem and cerebellum (3 subtypes: RTK1, RTK2, and MYCN) [13-15]. Infant-type hemispheric glioma typically arises in the first year of life and occurs in the cerebral hemisphere [16]. Lastly, diffuse midline glioma, H3 K27-altered, most commonly affects children with tumors appearing mainly in the thalamus and spinal cord, driven by oncohistone alterations (4 subtypes: H3.3 p.K28M (K27M)-mutant, H3.1/H3.2 p.K28M (K27M)-mutant, H3-wildtype with EZHIP overexpression, and EGFR-mutant) [15].

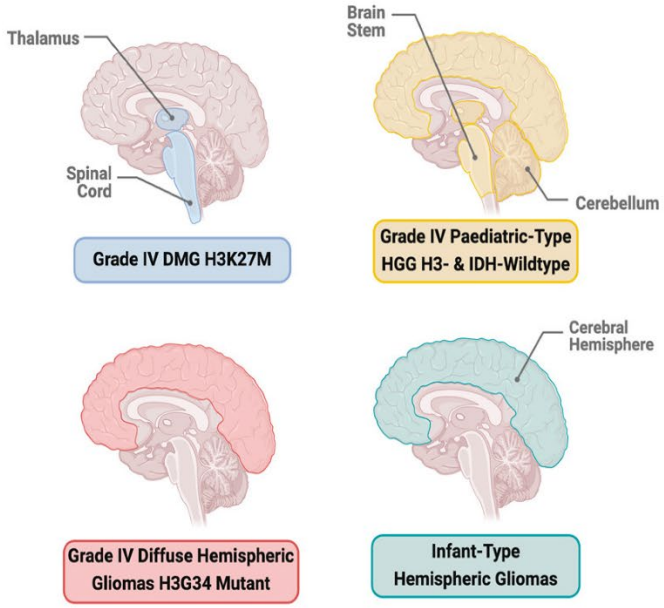

Mutation	Percentage of Occurence
ATRX	± 17% of all pHGGs
ACVR1	20% of DMG cases
BRAF V600E	6-15% of all pHGGs
TP53	80% of DMG samples
NTRK	10% of pHGGs
NF1	0.28-5% of pHGGs
FGFR, EGFR, PDGFR	60% of DMGs

Figure 1.1: Mutation landscape of pediatric high-grade gliomas. Description of the different mutations present in pediatric high-grade gliomas and their incidence [17].

1.2 Diffuse Midline Glioma

1.2.1 Epidemiology, clinical features, and prognosis

Among pHGGs, diffuse midline gliomas (DMGs) represent the most lethal and debilitating subtype, comprising approximately 50% of cases (**Fig. 1.2**) [18,19]. Formerly referred to as diffuse intrinsic pontine gliomas (DIPG) because of their typical origin from glial cells in the pons of the brainstem, these tumors were histologically classified as WHO grades II-IV [4,6,19-24]. This region of the brainstem is critical for vital functions such as respiration, motor function, and cranial nerve control, limiting surgical intervention. These tumors were also found to harbor a distinct histone mutation (H3K27M), distinguishing them from their adult glioma counterparts, and subsequent studies identified the same mutation in other high-grade gliomas that diffusely infiltrate midline structures such as the thalamus, cerebellum, and spinal cord, prompting a 2016 WHO reclassification from DIPG to diffuse midline glioma H3K27M-mutant [4,6,19-26]. In 2021, the WHO updated its classification to diffuse midline

glioma, H3K27-altered, to incorporate additional molecular alterations beyond the main H3K27M mutation, which leads to global H3K27 trimethylation loss [8,10]. Although DMGs tend to remain localized within the CNS without distant metastases, they are classified exclusively as WHO grade IV, reflecting their highly invasive nature and poor outcomes [8,10]. Children are typically diagnosed with DMG at a median age of 6-7 years old, with a median survival of only 9-11 months [27-30]. Clinical manifestations depend on lesion size and tumor location; however, in over 50% of cases, typical symptoms include cranial nerve deficits, cerebellar signs, or long-tract signs [31,32]. Due to the manifestation of these symptoms, quality of life is significantly impacted, with a rapid decline and a survival rate of less than 10% beyond 2 years from diagnosis [31,33,34]. The lack of effective therapies that improve outcomes highlights an urgent need for novel therapeutic strategies to enhance patient survival.

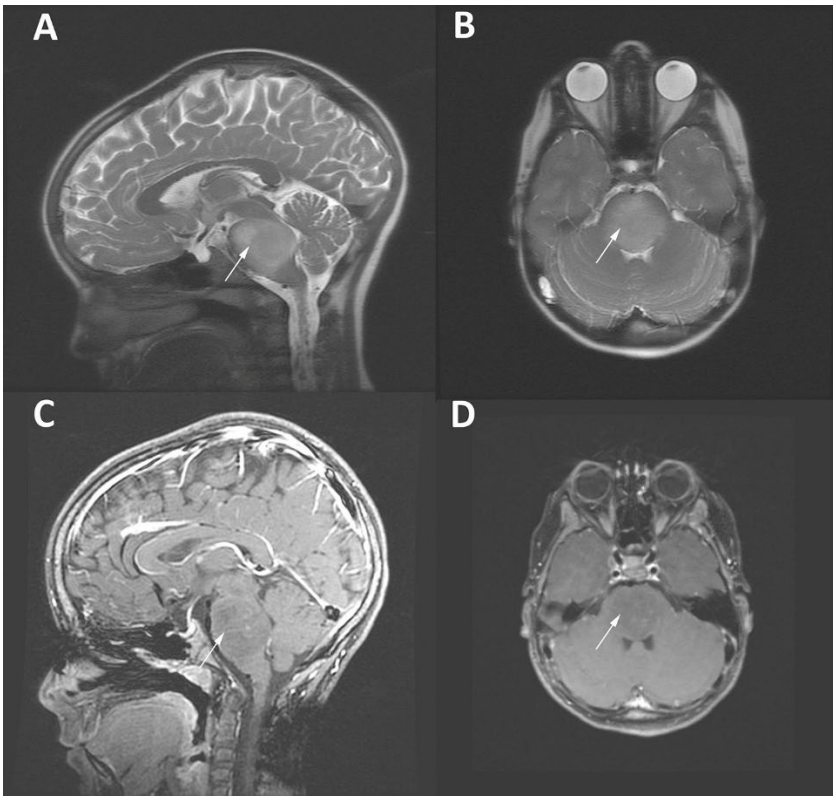

Figure 1.2: MRI imaging of an 8 year-old girl with a DIPG tumor (white arrows). T2-weighted sagittal (**A**) and axial (**B**) images demonstrate the enlargement of the brainstem and highlight the diffuse infiltrative characteristic of DIPG tumors. (**C,D**) Gadolinium-enhanced T1-weighted MRI images of the same patient demonstrating scant patchy enhancement [35].

1.2.2 Diffuse Midline Glioma H3K27M: Biology and molecular drivers

The majority of DMG cases harbor a characteristic lysine to methionine substitution at position 27 of histone H3 affecting either the H3F3A (H3.3) or HIST1H3B (H3.1) genes resulting in a distinct point mutation (H3K27M) [36-38]. This change disrupts chromatin structure by inhibiting the activity of PRC2 (Polycomb Repressive Complex 2), a multi-protein complex responsible for regulating the addition of the repressive histone marker H3K27me3 (**Fig. 1.3**) [39-42]. This global loss of H3K27me3 results in epigenetic reprogramming, leaving chromatin in a more “open” state, thereby increasing transcription factor and RNA polymerase access to DNA, and promoting aberrant gene expression and overall tumor progression [21,22,43,44]. Mutations in TP53, PDGFRA (platelet-derived growth factor alpha), and ACVR1 are typically

associated with DMGs, impairing genomic stability and developmental signaling, thereby activating pro-survival pathways and perpetuating gene dysregulation [38,45,46]. These additional mutations, combined with epigenetic dysregulation, create a distinct form of oncogenesis. Small-molecule targeted therapies are currently being evaluated as strategies to overcome these hurdles. A notable small molecule currently undergoing early-phase clinical trials is ONC201, which activates the integrated stress response and dopaminergic pathways while reducing the expression of epigenetic regulators such as EZH2, the catalytic subunit of PRC2, thereby increasing H3K27me3 [47]. Treatment with ONC201 has shown considerable success for the treatment of H3K27M DMG tumors, with some patients experiencing greater than 70% regression in tumor size [48]. Another approach that has shown great success and is currently being evaluated in preclinical and early-phase trials is chimeric antigen receptor T-cell (CAR T) therapies, particularly targeting GD2. In a 2024 study, GD2-CAR T cells significantly reduced tumor size in over half of the patients and increased median survival to nearly 2 years after treatment [49].

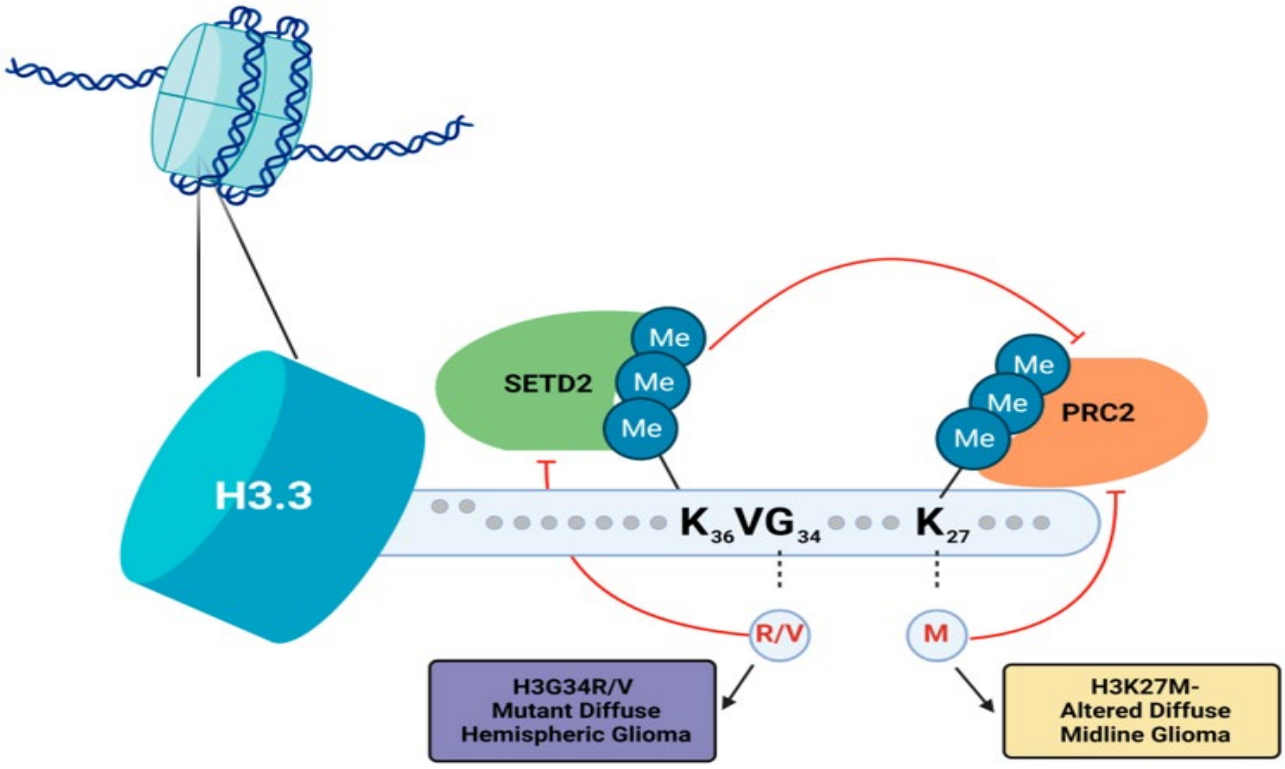

Figure 1.3: Diagram of the H3K27M mutation and H3G34R/V mutation. H3K27M/H3G34R/V disrupt H3K27me3. H3K27M inhibits PRC2, resulting in reduced histone trimethylation; H3G34R/V inhibits SETD2, resulting in reduced H3K36me3 [50].

1.2.3 Therapeutic challenges and unmet clinical needs

Currently, DMGs are mainly diagnosed radiologically, with biopsies recently becoming more common due to advancements in surgical techniques to enable molecular diagnosis and immunotherapy development [51-53]. Additional studies have suggested that a non-surgical molecular diagnostic approach can be achieved through liquid biopsies in which tumor-derived nucleic acids found in cerebrospinal fluid (CSF) are collected and analyzed using digital droplet PCR (ddPCR) [54]. This has been shown to successfully characterize H3K27 mutations and predict tumor progression before radiological detection [54]. Additional strategies for diagnosing and tracking tumor progression are critical due to the unique anatomical location and the highly invasive nature of these tumors, limiting surgical resection

and leaving focal radiation as the current and only standard of care treatment [55]. The current radiotherapy protocol for patients is to receive 54-59.4 Gy in 30-33 fractions of 1.8 Gy daily, with the corticosteroid dexamethasone also typically administered alongside to help reduce neurological symptoms [31,56]. However, this regimen is only partially effective, with most patients experiencing only a temporary delay in tumor growth, and a mean progression-free survival of approximately 6 months before inevitable disease recurrence [57]. Conventional chemotherapies have shown limited efficacy in extending survival, largely due to the blood-brain barrier (BBB) and blood-tumor barrier (BTB), which restrict the delivery of many chemotherapeutic agents into the brain [58,59]. Clinical trials of chemotherapies confirm poor accumulation and no significant survival benefit compared with radiotherapy alone [34,60,61]. Novel therapeutic strategies that effectively target tumor migration and enhance drug delivery across the BBB are urgently needed to improve long-term outcomes for children with DMG.

1.3 Mechanisms driving therapeutic resistance in glioma

1.3.1 Proliferation, invasion, and vascular remodeling

One of the main challenges in treating gliomas is their ability to invade healthy brain tissue, making curative surgery impossible and driving tumor recurrence. Histologically, this invasion is characterized by preferential spread along white matter tracts and perivascular growth [62]. This behavior is thought to be driven by the secretion of proteolytic enzymes by tumor cells that degrade the extracellular matrix (ECM), a major regulator of cell and tissue function, and facilitate their migration into normal brain parenchyma [62,63]. Many glioma cells exhibit an intrinsic stem-like phenotype, exhibiting high self-renewal potential and motility. Because of these cells' ability to rapidly proliferate and their intrinsically infiltrative nature, they can diffusely colonize distant regions of the brain, evading localized therapies and

further driving tumor progression and subsequent recurrence [64]. Given the lack of effective standard-of-care therapies and the intact BBB/BTB, which limits drug delivery, identifying strategies to effectively combat their uncontrolled proliferation and migration is imperative for improving DMG therapy.

Another important mechanism driving therapeutic resistance in high-grade gliomas is angiogenesis, although DMG exhibits a vascular phenotype distinct from that of its other high-grade glioma counterparts [65]. Angiogenesis is the formation and development of new blood vessels through the remodeling of existing vessels, and it occurs in three distinct steps. First, to form new blood vessels, glioma cells disrupt the normal contact between endothelial cells and the basement membrane by targeting astrocytic foot processes, thus destabilizing the vessel wall [66,67]. Next, this degradation of the vessel membrane and surrounding ECM allows endothelial cells to invade and initiate new vessel formation in different areas of the brain. These endothelial cells then invade toward glioma cells that express pro-angiogenic factors, thereby enhancing cell adhesion and migration and allowing the process to self-maintain [67,68]. In GBM and other high-grade gliomas, tumor growth is strongly associated with robust vascularization, leading to abnormal, leaky blood vessels and a disrupted BBB. However, in DMG, the tumor microenvironment is less vascularized, and the BBB is more intact, with a relatively organized vascular network compared with GBM [67,69,70].

1.4 Glycogen synthase kinase-3 (GSK-3) signaling in glioma biology

GSK-3 is a serine/threonine protein kinase that consists of two mammalian isoforms, GSK-3α and GSK-3β [71]. These isoforms are highly homologous, sharing 98% identity in their kinase domains [72]. Their differences arise from their N- and C-terminal sequences, with the insertion of a glycine-rich domain in GSK-3α, which also contributes to their size, with GSK-3α at 51 kDa and GSK-3β at around 47 kDa [73]. Although they possess similar structural identities, their functions are distinct. A previous study by Hoeflich et al. (2000) reported functional differences using knockout (KO) mouse models for each isoform. Mice with the GSK-3β (KO) die late in development, around embryonic day 16, and those with the GSK-3α KO, although surviving, exhibit a shortened lifespan and male infertility, highlighting the functional differences between these isoforms [74]. Despite these differences, most attention has focused on GSK-3β, as reports suggest a more specific role in regulating cellular function [75]. Initially, GSK-3β was reported to inhibit glycogen synthesis by phosphorylating glycogen synthase; however, subsequent investigations have also revealed its regulatory role in a wide range of cellular functions. GSK-3β negatively regulates downstream signaling pathways, and inhibition of this kinase stimulates many cellular functions otherwise suppressed by its activity [76]. Its activity is controlled by post-translational phosphorylation, in which inhibition of GSK-3β is regulated by the phosphorylation of S9, and its activation is regulated by the phosphorylation of Tyr216, whereas GSK-3α inhibition is controlled by S21 [77].

Aberrant gene expression is a well-established hallmark of DMG, leading to uncontrolled proliferation and its invasive phenotype. Amplifications in the PI3K/AKT, WNT/β-catenin, and MAPK pathways are frequently found in DMG, contributing to their growth and therapeutic resistance [78-80]. GSK-3 is a central regulatory kinase within these signaling

cascades, contributing to glioma cell proliferation and migration, and has emerged as a promising therapeutic target due to its multifaceted role in glioma biology [78-83]. Inhibition of GSK-3 represents a promising strategy to improve DMG therapy by limiting tumor cell migration and motility, enhancing drug delivery by modulating the BBB, and reducing off-target toxicity, compared with broad-spectrum kinase inhibitors. Despite these findings, GSK-3 is critically understudied in DMG, and whether GSK-3 inhibition simultaneously alters tumor behavior and endothelial barrier function in pediatric glioma models has not been systematically examined.

1.4.1 GSK-3 and Canonical Pathways of Cancer

Molecular profiling of pHGG has identified several alterations in both epigenetic and kinase signaling pathways [84]. Mutations and amplifications in the PI3K-AKT are one of the major contributions to tumor growth, survival, and migration of pediatric high-grade gliomas, leading to treatment resistance and poor outcomes [85]. Alterations in platelet-derived growth factor receptor alpha (PDGFRA) are also frequently associated with the H3.3K27M mutation in DMG, driving downstream signaling through the PI3K-AKT pathway (**Fig. 1.4**) [86,87]. Through this pathway, GSK-3α/β are constitutively active kinases that are inactivated through phosphorylation with Serine 21 phosphorylating GSK-3α and Serine 9 phosphorylating GSK-3β [77]. This inactivation leads to increased mTOR activity, which promotes the expression of pro-survival and angiogenic proteins, such as VEGF.

Another signaling pathway associated with GSK-3 inhibition in cancer is the WNT/β-catenin pathway [88]. Typically, WNT signaling is suppressed when GSK-3 is active because it phosphorylates β-catenin, targeting it for ubiquitination and subsequent proteolytic

degradation [89]. When GSK-3 is inactivated through AKT-mediated phosphorylation at sites S9/S21, β-catenin cannot be phosphorylated, allowing its nuclear accumulation and increased transcription of pro-oncogenic genes such as c-MYC and cyclin D1 [90,91]. Despite the potential of β-catenin driven pro-oncogenic signaling, in glioma, GSK-3 has been shown to function in a tumor-suppressing fashion through inhibition of proliferation, increased apoptotic signaling, and decreased VEGF expression [83,91-93]. Studies have implicated GSK-3β in the pathway that promotes nuclear factor-κB-mediated cell survival, and that dysregulated GSK-3β maintains the survival and proliferation of colon cancer cells, and that inhibition of this kinase leads to apoptosis [94]. This suggests that the role of GSK-3 in cancer is highly context-dependent and that, in glioma, it may be a promising target for inhibiting tumorigenesis by arresting tumor cell growth, promoting apoptosis, and reducing the motility and migration of glioma cells.

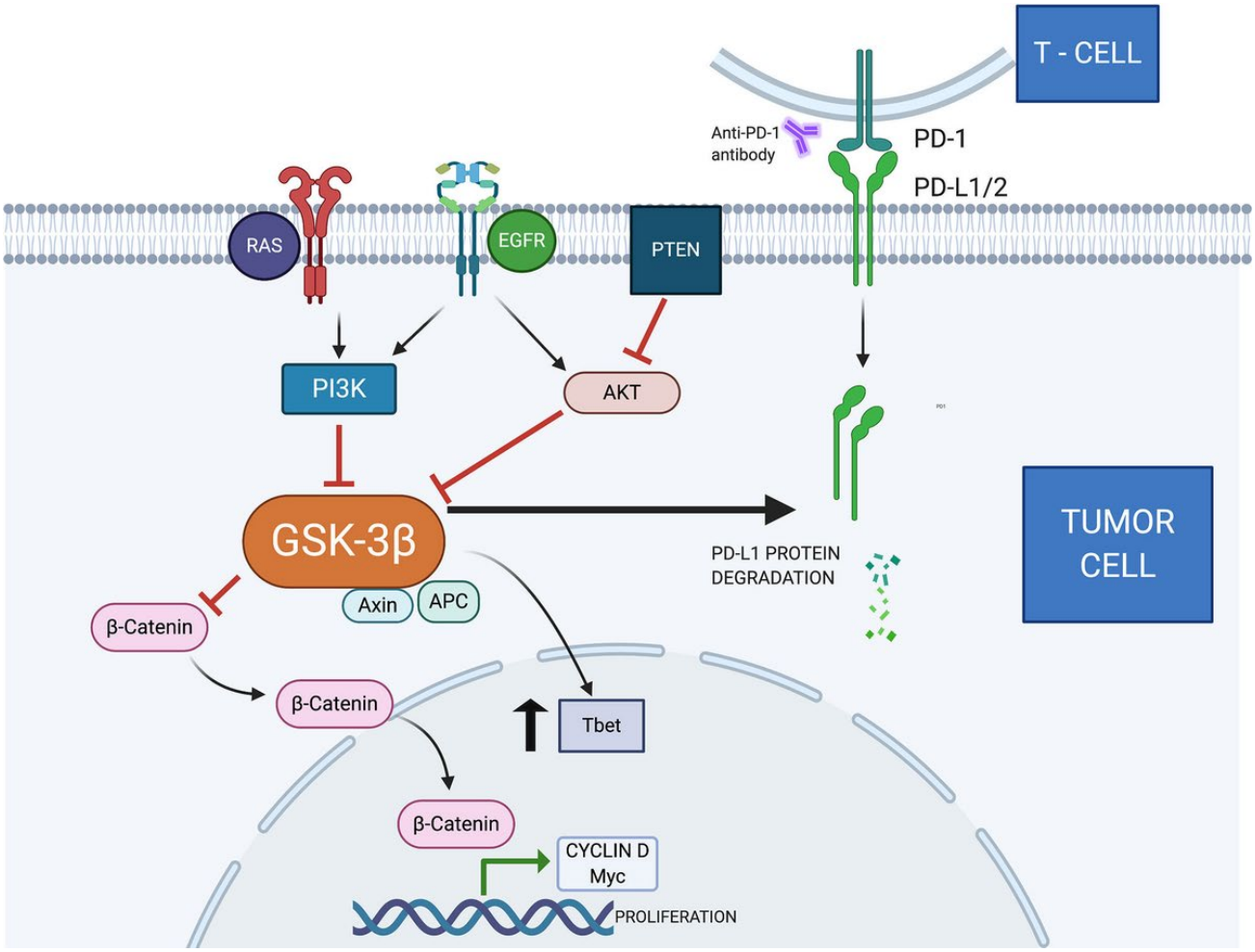

Figure 1.4: Diagram of GSK-3β pathway inactivation. PI3K and AKT phosphorylate GSK-3β inactivating it, blocking the Axin/APC destruction complex from targeting β-catenin for ubiquitination. β-catenin translocates to the nucleus driving cyclin D1 and c-Myc expression and aberrant proliferation [87].

1.4.2 GSK-3 inhibitors

Over the past three decades, there have been tremendous efforts focused on developing GSK-3 inhibitors as potential therapeutics for treating type 2 diabetes, Alzheimer's disease, bipolar disorders, and cancer [95]. This rising interest in GSK-3 as a cancer therapeutic arises from its diverse roles in regulating critical cellular processes that are typically dysregulated in cancer cells, leading to cell cycle arrest, reduced proliferation, and increased apoptosis [96]. In 2008, Rinnab et al. observed that treatment with the GSK-3

inhibitor SB216763 decreased androgen receptor function and cancer cell proliferation in prostate cancer cells [97]. This was followed up by the first clinical study of LY2090314, another potent and selective GSK-3 inhibitor, in which partial responses and stable disease were observed in some participants[98]. Other GSK-3 inhibitors, including AZD-1080 and Tideglusib, which were originally designed and tested for the treatment of Alzheimer's disease, are also under investigation for their potential in cancer therapy [99]. In a study by Chen et al. (2016), ovarian carcinoma cells treated with AZD-1080 showed a significant downregulation of GSK-3β and arrested cell-cycle progression [100]. Ding et al. (2019) observed that the GSK-3 inhibitor 9-ING-41 prevented gemcitabine-induced DNA damage repair and induced apoptosis in chemo-resistant pancreatic cancer cells [101]. Although there has been a surge in the development of GSK-3 inhibitors, their clinical potential remains under evaluation due to their ability to increase β-catenin levels and the transcription of proto-oncogenes [89]. Despite their role in the WNT signaling pathway, in which inhibition leads to nuclear β-catenin accumulation and increased proliferation and expression of pro-survival genes, no studies have reported an increase in cancer incidence with GSK-3 inhibitor treatments [89].

1.5 Indirubin derivatives as multi-kinase inhibitors

Apart from the classic H3K27M mutation observed in DMG, aberrant kinase signaling within the receptor tyrosine kinase (RTK)-PI3K-MAPK pathway was observed in approximately 62% of cases [102]. A molecular meta-analysis by Mackay et al. (2017) revealed that most H3.3-G34R/V tumor mutations were observed at the RTK level, whereas those in H3.1-K27M and H3-WT tumors mainly exhibited PI3K/mTOR alterations and MAPK aberrations, respectively [102]. This dysregulation contributes to a pro-tumorigenic microenvironment that drives migration and decreases the expression of tumor suppressor genes, leading to overall therapeutic resistance. Indirubins, bisindole alkaloids, and one of the main bioactive components of *Indigo naturalis* are known to possess anti-inflammatory, antiviral, immunoregulatory, and anticancer activities through various studies [103,104]. Several indirubin derivatives have been synthesized and have emerged as potent multi-kinase inhibitors, and studies have reported that they possess even greater antitumor and anti-inflammatory effects with less toxicity than indirubin [105]. These derivatives have been shown to inhibit cancer cell proliferation, induce apoptosis, and inhibit cancer cell migration and invasion in various cancers [106-108].

In general, indirubin and its derivatives are potent cyclin-dependent kinase (CDK) and GSK-3β inhibitors possessing high affinity for CDK ATP-binding sites [105]. This inhibition of CDKs, which are important regulators of the cell cycle and are dysregulated in various cancers, promotes suppression of cancer cell proliferation. Inhibition of CDK2 by indirubin-3'-monoxime (I3M) has been observed to induce G2/M cell cycle arrest in Jurkat cells and has been shown to inhibit CDK1/cyclin B binding in MCF-7 cells, inducing cell cycle arrest in the G1 and G2/S phases [109,110]. Indirubin derivatives are also known to inhibit the expression

of several NF-κB-related genes, including Bcl-2, c-MYC, and MMP-9, which are involved in anti-apoptosis, proliferation, and invasion, promoting a pro-tumorigenic environment that indirubins counteract [111]. Another well-known target of indirubins is the aryl hydrocarbon receptor (AhR). In glioma cells, the indirubin derivatives E804 and 7BIO act as AhR agonists, binding to AhR, activating its signaling pathway, and inhibiting STAT3 expression, thereby decreasing glioma cell proliferation and promoting apoptosis [105,112].

Given the central role of GSK-3 in regulating different cellular processes related to tumor growth and progression, indirubin derivatives that target this node represent a compelling multi-kinase strategy for targeting this pathway. Previous studies have investigated the indirubin derivative 6-bromoindirubin-3′-acetoxime (BIO-acetoxime/BIA), as a small-molecule kinase inhibitor that possesses activity against GSK-3β and other signaling pathways. BIA acts as an ATP-competitive protein kinase inhibitor by binding to the conserved ATP-binding pocket of different kinases, preventing phosphorylation [113,114]. Due to the structural conservation of this ATP-binding pocket across many different kinases, BIA exhibits broad activity across several kinase pathways, including CDKs, and has also been reported to be a potent inhibitor of GSK-3 [107,108,115,116]. However, due to BIA's ability to target several kinases, the specific mechanisms underlying the biological effects of BIA are unclear and defining the contributions of GSK-3 dependent mechanisms represent a critical next step.

Consistent with its multi-kinase activity, these studies have shown that BIA possesses anti-invasive properties, decreases tumor cell growth in glioma cells, and enhances survival in GBM xenograft models [93,106,113,117,118]. It has also been shown to enhance BBB

permeability by disrupting tight junction formation, leading to increased uptake in *in vitro* BBB models and reduced trans endothelial electrical resistance (TEER) [93]. This dual mechanism has therapeutic potential for the treatment of DMG, which is known to diffusely infiltrate structures of the brain and exhibit inadequate CNS penetration of chemotherapeutic agents. The effects of indirubin derivatives on glioma motility and migration have also been shown in a study by Nowicki et al. (2008) in which indirubins blocked glioma tumor cell invasion and decreased endothelial cell motility and angiogenesis [83]. Another study by Cockle et al. (2015) demonstrated the efficacy of the indirubin derivative, BIO, in inhibiting migration and invasion in pHGG cell lines [92]. They observed significant reductions in migration, as well as morphological changes associated with decreased cellular motility [92]. Together, these findings emphasize the therapeutic potential of indirubin derivatives for targeting GSK-3 mediated signaling and related signaling pathways in glioma.

1.6 Rationale for GSK-3 as a therapeutic target for Diffuse Midline Glioma

Inhibition of GSK-3 represents a promising strategy to improve DMG therapy, with several studies highlighting its impact on GBM. Kotliarova et al. (2008) used a panel of small-molecule GSK-3 inhibitors (LY2064827, 705701, 708244, and 709125) and showed that these inhibitors significantly reduced glioma cell survival and clonogenicity by activating c-MYC, which subsequently increased the expression of Bax, Bim, DR4/DR5, and TRAIL, promoting cytotoxicity [91]. They also showed that GSK-3 inhibition resulted in a significant decrease in intracellular nuclear factor-κB (NF-κB) activity, as well as mitochondrial destabilization due to dissociation of hexokinase-II (HKII), leading to decreased glioma cell survival and inhibition of tumor growth *in vivo* [91]. Another study by Korur et al. (2009) showed that GSK-3 inhibition reduced colony formation and cell migration, and induced apoptosis in

GBM cells through G2/M phase accumulation and arrest [119]. Miyashita et al. (2009) showed that GBM tumors exhibited higher expression of GSK-3β, and its active form phosphorylated at Tyr216 [94]. Treatment with the GSK-3 inhibitor AR-A014418 suppressed proliferation, chemosensitivity, and radiotherapy sensitization, and decreased the viability of glioma cells [94]. Several studies have also shown that LiCl, a well-known inhibitor of GSK-3β and therapeutic treatment of bipolar disorder and depression, can inhibit glioma cell migration and invasion and facilitate apoptotic signaling [120,121]. This was further shown in a comparative study with LiCl and an indirubin derivative, BIO where they pharmacologically inhibited the migration of both adult and pediatric glioma cells [92,106]. Despite the promising success of GSK-3 inhibitors in suppressing GBM tumorigenesis by inhibiting proliferation, reducing migration, and attenuating angiogenic signaling, their potential as therapeutic targets remains critically understudied in pediatric high-grade gliomas and diffuse midline glioma.

1.7 BBB and BTB in glioma therapy

1.7.1 BBB

CNS-related pathologies represent around 6% of the total global disease burden, according to the WHO [122]. Most of these conditions remain incurable or extremely challenging to treat, as a result, current therapies are largely limited to symptom management due to the BBB severely restricting drug delivery [123]. CNS diseases hold the BBB as a major factor for neglecting appropriate therapies to reach target areas in the brain parenchyma. About 90% of small molecule inhibitors and majority of macromolecules are unable to cross the BBB [123].

The BBB is a highly specialized layer of capillary endothelium forming the boundary between the circulating blood and the brain parenchyma [124]. It maintains CNS homeostasis

by tightly regulating the exchange of ions, nutrients, and oxygen, while restricting the entry of circulating neurotoxic molecules and pathogens. Structurally, the BBB is composed of human brain microvascular endothelial cells (hBMECs), supported by pericytes embedded within the basement membrane, and astrocytic end-feet enriched in aquaporin-4 that ensheathe the vasculature and interface with neurons and other glial cells [124]. The BBB, along with the extracellular matrix (ECM), make up the neurovascular unit (NVU), a fundamental anatomical node relevant for CNS function. BBB impermeability is a result of paracellular tight junctions (TJs) and adherens junctions (AJs) that block the passage of large macromolecules (>400 Da) by creating bridge-like formations and reducing the physical space between hBMECs. Tight junctions form through interactions with claudins (CLDN-1, -3, -5, and -12), zonula occludens-1 (ZO-1), and occludin to create the highly restrictive paracellular barrier that is essential for maintaining BBB integrity. Disruption or downregulation of these junctional components compromises barrier function and has been implicated in neurological pathologies, including ischemic stroke [125,126]. On the other hand, AJs mainly involve vascular endothelial (VE)-cadherin and β-catenin [126]. A functional hallmark of the BBB endothelium is the augmented expression of drug efflux pumps, which are members of the ATP-binding cassette transporter family [127]. These include P-glycoprotein 1 (P-gp1), members of the ATP-binding cassette sub-family C (ABCC), and ATP-binding cassette sub-family G member 2 (ABCG2), which prevent the entry of small molecules, including pharmaceuticals, into the brain, thereby establishing the BBB as the central obstacle to effective CNS drug delivery [127].

1.7.2 The BTB in high-grade brain tumors

In the context of brain cancer, the role of the BBB in tumor pathogenesis remains an

active field of research. In most high-grade gliomas, the BBB's molecular and cellular composition is altered, shifting several components of its biology to promote an angiogenic and tumor-permissive microenvironment known as the BTB [128]. Vascularization in high-grade brain tumors occurs through multiple mechanisms, including angiogenesis, vasculogenesis, vessel co-option, and vascular mimicry, each reflecting distinct tumor–vascular interactions [129]. Angiogenesis refers to the formation of new blood vessels from pre-existing vasculature, whereas vasculogenesis involves the *de novo* assembly of vascular structures from endothelial progenitor cells. In contrast, vessel co-option enables tumor cells to hijack and grow along existing host vessels, while vascular mimicry describes the formation of perfusable, vessel-like networks by tumor cells themselves, collectively reshaping the BTB landscape. Further mechanistic studies are required to determine the contribution of these vascularization mechanisms to functional tumor vasculature in brain neoplasms. Despite this information, the role of the BTB in remodeling the tumor microenvironment of high-grade tumors and the therapeutic potential of targeting the BTB to improve drug delivery and efficacy remain understudied aspects of brain tumor biology.

1.7.3 Biology of endothelial cell-adhesion molecules in the BTB

In contrast to the homeostatic BBB, the BTB exhibits disrupted tight junctions. Paracellular adhesion molecules at the endothelium, such as claudin-1, -5, -11, occludins, and ZO-1, all show reduced expression or aberrant architecture in high-grade gliomas [128 130]. Interestingly, AJs, such as β-catenin, have shown increased expression in high-grade gliomas and their associated vasculature, suggesting a potential role for tumor pathogenesis [131]. The heterogeneity of this junctional profile within the BTB increases the biological complexity of endothelial barrier function in brain cancer (**Fig. 1.5**).

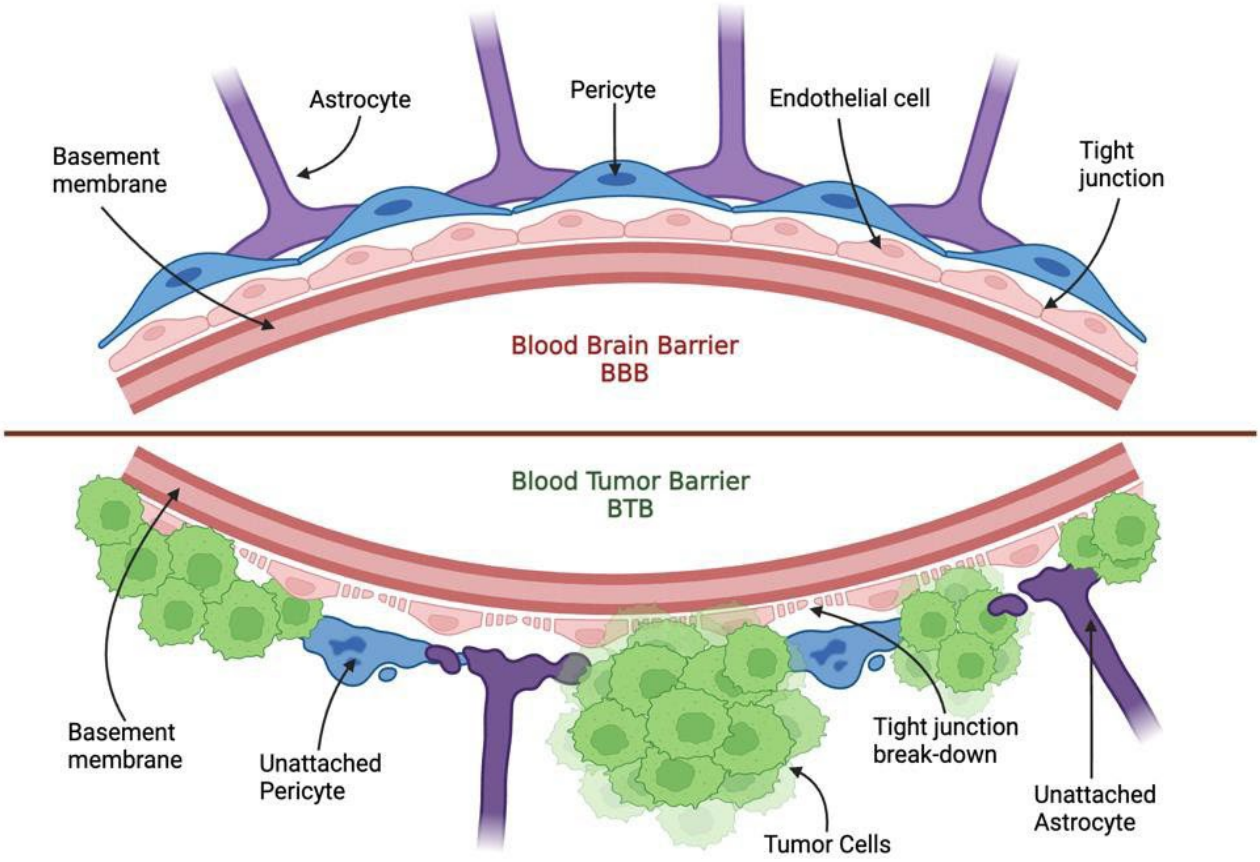

Figure 1.5: Schematic of the contrasting cellular composition of the BBB and the BTB in CNS malignancies. The normal BBB architecture is highlighted above, showing intact tight/AJs, pericyte coverage, and astrocytic end feet. The BTB architecture (below) shows junctional breakdown, pericyte detachment, and loss of astrocytic end feet, highlighting the vast phenotypic heterogeneity between the healthy BBB and the tumor-associated barrier [132].

Post-translational modifications of tight junctions and AJs critically influence tumor-associated vasculature, reshaping the TME to promote tumor growth and invasion. For example, hypoxic and necrotic core areas of the tumor present high levels of vascular endothelial growth factor A (VEGFA) secretion, which binds to and activates the VEGFR1/VEGFR2-SRC axis, subsequently phosphorylating VE-cadherin at Tyr685 of its cytoplasmic domain, which promotes vascular leakage and endothelial permeability [133]. On the other hand, VE-cadherin phosphorylation at Tyr731 facilitates leukocyte diapedesis [133], which is potently triggered by IL-1β signaling, a highly expressed cytokine in (GBM).

Additional reports indicate that VE-cadherin junctions are directly relevant to GBM invasion and survival. VE-cadherin-expressing tumor cells exhibit enhanced capacities for vascular co-option and mimicry, allowing for enhanced tumoral interaction with the vasculature via VE-cadherin physical association with Focal Adhesion Kinase (FAK) and β-catenin to modulate transcription factor 4 (TCF-4) transcriptional activity [134]. In addition, VE-cadherin interacts and upregulates programmed death-ligand 1 (PD-L1), promoting an immunosuppressive microenvironment [135]. This data supports the role of endothelial adhesion molecules in driving the immune conditions of brain tumors, highlighting their relevance as therapeutic targets.

1.7.4 The biology of the BTB in DMGs

In contrast to their cortical high-grade glioma counterparts, DMGs maintain an intact BBB, making drug delivery even more difficult. Despite their lethality, few studies have examined DMG vasculature or the role of the BTB in DMG tumor growth and progression.

DMGs characteristically exhibit low gadolinium contrast enhancement and reduced peritumoral edema compared to cortical gliomas, such as GBM, supporting clinical observations of preserved BBB structural integrity [136,137]. However, DMG biopsies and autopsies have revealed downregulation of tight junction molecules Claudin-5 and ZO-1, reduced basement membrane laminin, decreased the efflux pump Pg-P1, and lower platelet-derived growth factor receptor beta, PDGFRβ, a marker associated with pericytes [138]. Reduced vessel density relative to the healthy brain was also observed, suggesting that although DMG vasculature may be structurally altered, this does not result in the pronounced leakiness typically observed in cortical high-grade gliomas.

These clinical observations of preserved BBB integrity are further supported by patient-derived DMG xenograft murine models that showed tight junction and Glut1 expression, and whose blood vessels were not significantly different from those of healthy controls [133]. Endothelial cells isolated from murine DMG models have also been shown to be more closely associated with healthy endothelium than with high-grade glioma endothelium, as evidenced by maintenance of ECM organization, vascular adhesion, transmembrane support, and WNT/Hippo signaling [137]. A 2018 study by Shaik et al. (2018) found that RE1 Silencing Transcription Factor (REST) expression in DMG tumors promotes vascularization through Gremlin-1 and VEGFR2/AKT signaling, and that REST knockdown reduced tumor growth and vascular density [139]. Aberrant type 2 microvascular proliferation (MVP), characterized by elevated vascular garlands, glomerular tufting, and reduced microvascular sprouting, significantly correlated with tumor grade and progression, with higher expression resulting in worse prognosis and overall survival [140]. Deeper molecular studies of the vasculature and the neurovascular unit in DMGs are needed to elucidate their relevance to

DMG biology and their potential as therapeutic targets.

1.8 Project Rationale, aims, and objectives

1.8.1 Rationale/Gap Summary

Treatment of DMG has remained unchanged in the past 40 years since radiotherapy has become the standard of care, and it remains a universally fatal CNS tumor with a less than 2% 5-year survival rate. One major challenge in treating DMG is the BBB, which restricts the delivery of chemotherapeutics into the brain. This challenge is exacerbated by epigenetic histone mutations (H3K27M) and amplifications in key signaling pathways (PI3K/AKT, WNT/β-Catenin, and MAPK), that lead to therapeutic resistance and overall tumor progression. GSK-3 has been considered a promising therapeutic target for DMG due to its role in regulating glioma cell migration, angiogenesis, and endothelial function. Indirubin derivatives, multi-kinase inhibitors with potent GSK-3 selectivity, have shown promise as therapeutic agents for treating glioma; however, translation to the clinic for treatment of DMG remains difficult due to their multi-kinase activity, which may cause off-target effects. Elucidating BIA’s underlying mechanisms and the full scope of GSK-3 inhibition's role in its anticancer activity remains an obstacle to enhancing its translational impact. Unlike the broader kinase-inhibitory profile of indirubins, selective GSK-3 inhibitors may produce similar effects while reducing off-target toxicity. Developing dual-action therapies that simultaneously counteract DMG progression by inhibiting proliferation, migration, and invasion, whilst modulating barrier permeability to enhance chemotherapeutic uptake, is imperative to improve DMG therapy.

1.8.2 Central hypothesis

We hypothesized that GSK-3 inhibition could be an effective therapeutic approach for DMG by targeting tumor invasion and angiogenesis, and by improving drug delivery through modulation of endothelial barrier function. We sought to investigate this and address this therapeutic gap through three specific aims: First, we sought to characterize the effects of GSK-3 inhibition on tumor cell biology. Next, we assessed the effects of GSK-3 inhibition on endothelial cell behavior and barrier permeability. Lastly, we identified potential combinations for the therapeutic treatment of DMG.

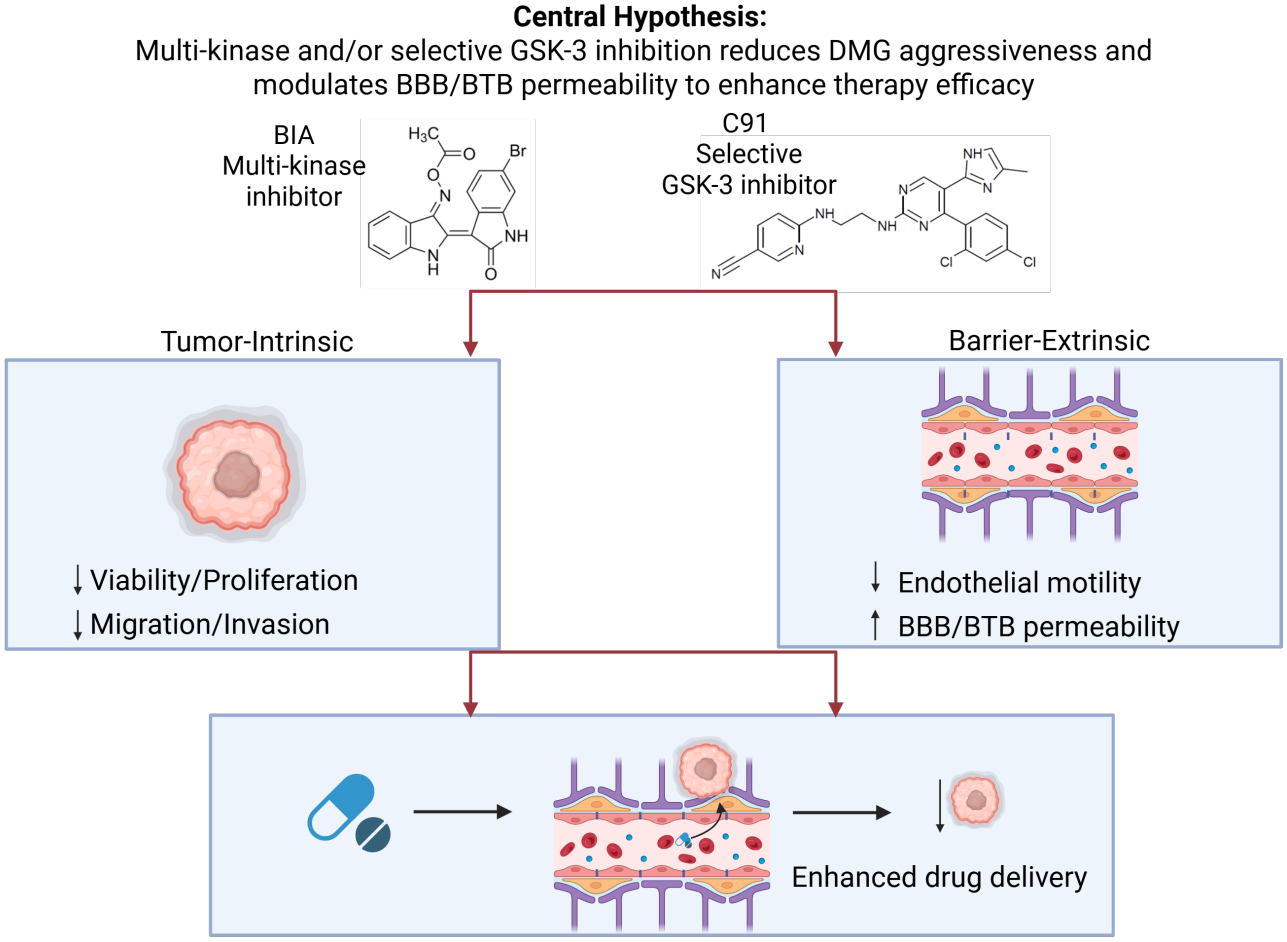

Figure 1.6: Schematic of the overall central hypothesis. Created in https://BioRender.com.

CHAPTER 2: MATERIALS AND METHODS

2.1 Cell lines and culture media

2.1.1 High-grade glioma cell lines

Primary human pediatric high-grade glioma (pHGG) cell line SF8628 (H3.3K27M DIPG) was purchased from Sigma-Aldrich (SCC127M). These cells were maintained in High Glucose DMEM (Sigma-Aldrich, Cat# D6546) supplemented with 10% heat-inactivated fetal bovine serum (HI-FBS, ThermoFisher Scientific Cat# A3840201), 1X GlutaMAX, 1X penicillin–streptomycin (P/S, ThermoFisher Scientific, Cat# 10378016), and sodium pyruvate solution (ThermoFisher Scientific, Cat# 11360-070). The patient-derived SU-DIPG-XXXVI cell line (SU-DIPG-36, H3.1K27M) was initially established at Stanford University by Dr. Michelle Monje. These cells were maintained in a working medium made from the Tumor Stem Medium (TSM) Base (Tables 1 and 2). The pHGG cell line KNS-42 was generously provided by Nikos Tapinos. These cells were maintained in D-MEM/F-12 (ThermoFisher Scientific, Cat# 1320033) supplemented with 10% HI-FBS and 1X P/S. Human G9-pCDH cells were obtained from OSU Ohio and maintained in Neurobasal medium (ScienCell) supplemented with 20ug/mL of human recombinant EGF (Peprotech), 20ug/mL FGF-B (Peprotech) and 0.1% P/S. All cell lines (**Fig. 2.1**) were STR profiled and free of mycoplasma contamination.

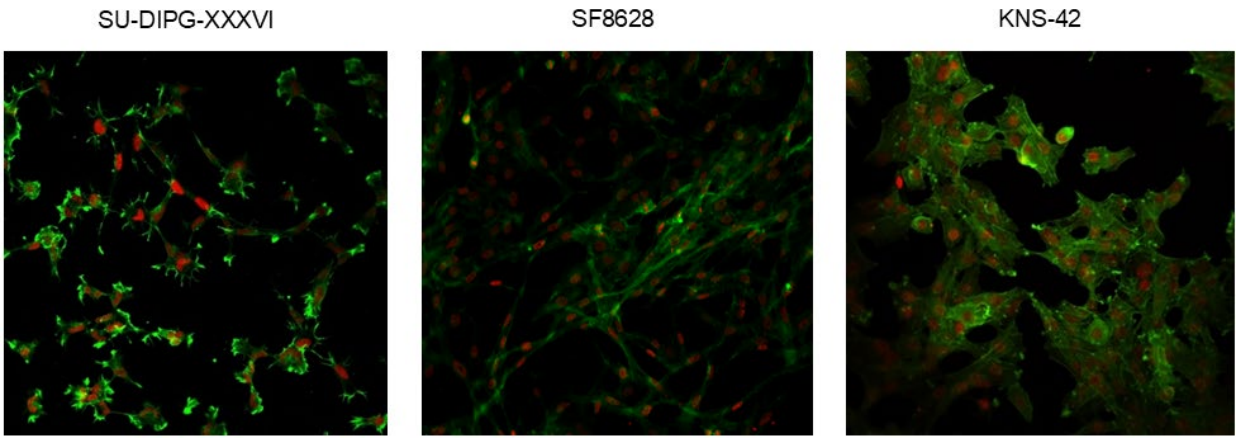

Figure 2.1: Immunofluorescence staining of pediatric high-grade glioma (pHGG) cell lines (SU-DIPG XXXVI, SF8628, and KNS42). Confirming expression of the H3K27M (SU-DIPG-XXXVI/SF8628; red=H3K27M, green=phalloidin) and H3G34V (KNS-42; red=H3G34V, green=phalloidin) mutations.

Table 1: Tumor Stem Medium (TSM) Base

Reagent	Vendor	Catalog No.	Volume
Neurobasal-A Medium (1X), liquid 1:1	ThermoFisher Scientific	10888-022	237.5 mL
D-MEM/F-12 (1X), liquid 1:1	ThermoFisher Scientific	11330-032	237.5 mL
HEPES Buffer Solution (1M)	ThermoFisher Scientific	15630-080	5 mL
Sodium Pyruvate Solution 100mM (100X), liquid	ThermoFisher Scientific	11360-070	5 mL
MEM Non-Essential Amino Acids Solution 10mM (100X), liquid	ThermoFisher Scientific	11140-050	5 mL
GlutaMAX-I Supplement	ThermoFisher Scientific	35050-061	5 mL
Penicillin–streptomycin	ThermoFisher Scientific	15140-122	5 mL

Table 2: Working TSM 1X (TSM base + Growth Factors)

Reagent	Vendor	Catalog No.	Working Conc.	Stock Conc.	Volume
TSM base					48.65 ml
Recombinant human EGF	FUJIFILM Biosciences	100-26	20ng/ml	20µg/ml	100 µL
Recombinant human FGF-basic-154	FUJIFILM Biosciences	100-146	20ng/ml	20µg/ml	100 µL
Human PDGF-AA	FUJIFILM Biosciences	100-16	10ng/ml	20µg/ml	50 µL
Human PDGF-BB	FUJIFILM Biosciences	100-18	10ng/ml	20µg/ml	50 µL
B-27 supplement minus Vitamin A (50x) liquid	ThermoFisher Scientific	12587-010	1X	50X	1 ml
Heparin solution 0.2%	StemCell Technologies	07980	2µg/ml	2mg/ml	50 µL

2.1.2 Endothelial and supporting cell lines

Immortalized human cerebral microvascular endothelial cells (hCMEC/D3, Sigma-Aldrich) were purchased from Sigma-Aldrich. These cells were maintained in basal endothelial cell media (ScienCell, Cat #1001) supplemented with FBS (Cat #0025), endothelial cell growth supplement (ECGS, Cat #1052), and P/S (Cat #0503) as provided by the company. Human primary astrocytes were purchased from Lonza Biosciences. These cells were maintained in basal astrocyte medium (ScienCell, Cat #1801) supplemented with FBS (Cat #0010), astrocyte growth supplement (AGS, Cat #1852), and P/S (Cat #0503) as provided by the company. Human primary pericytes were purchased from ScienCell. These cells were maintained in basal pericyte medium (ScienCell, Cat ##1201) supplemented with FBS (Cat #0010), pericyte growth supplement (PGS, Cat #1252), and P/S (Cat #0503) as provided by the company. Human primary pericytes and astrocytes were not used past passage 10 and hCMEC/D3 cells were not used past passage 15. All cell lines were STR profiled and free of mycoplasma contamination.

2.1.3 Cell culture and passaging

Suspension and adherent cells were passaged once or twice a week, respectively, and an automated cell counter (Invitrogen Cat# A49865) was used to quantify cell viability. For adherent cells, once cells were ready to be passaged, the media was aspirated from the flask, and the flask was washed with PBS to remove any residual FBS. After washing, 2 mL of Accutase or Trypsin-EDTA was added to the flask to detach the cells. Once the cells were detached, 5 mL of media was added to the flask to stop the reaction and collect the detached cells. Cells were added to a 15 mL conical tube and centrifuged (Sorvall ST Plus Series) at 300 × g for 3 minutes. After cells were spun down, the supernatant was aspirated, and cells

were resuspended in 2 mL of media for counting with the Cell Countess.

For suspension cells, the media and cells were collected from the flask, transferred to a 15 mL conical tube, and spun at 300 × g for 3 minutes. After cells were spun down, supernatant was aspirated, and 1 mL of Accutase was added to the cell pellet. The tube was incubated at 37 °C in the bead bath for 5 min to allow spheroid clumps to dissociate into single cells suspension. Once adequately dissociated, cells were spun down again and resuspended in 2 mL of media for cell counting using the Cell Countess.

Cells were frozen at 1-2 million cells per mL in Bambanker cell freezing medium (Fisher Scientific, Cat# NC2960954) in a Mr. Frosty (Nalgene) at -80 °C overnight, then stored in liquid nitrogen for long-term storage. To retrieve the cells, cryovials were quickly thawed in a 37 °C bead bath, 1 mL of the appropriate cell culture medium was added dropwise to the cells, and the cells were then centrifuged at 300 × g for 5 minutes. The cell-freezing culture medium mixture was removed, and cells were resuspended in the associated medium and placed into a T-75 cell culture flask (Nunc) to allow for expansion.

2.2 Compounds, reagents, and antibodies

2.2.1 Compounds and reagents

All compounds were reconstituted in dimethyl sulfoxide (DMSO) to 10 mM, aliquoted into single-use volumes, and stored at either -20 °C or -80 °C. Working concentrations, storage conditions, and additional information on each compound and reagent are detailed in Table 3. The Approved Oncology Drugs Set XI (AOD XI) was obtained from the National Cancer Institute Developmental Therapeutics Program (NCI/DTP) Open Chemical

Repository. This plate contains 176 FDA-approved anticancer agents, each at 10 mM in 20 µl per well in DMSO. Plates were shipped frozen with dry ice and stored at -80 °C until use. All compounds were found to have satisfactory purity and identity by the NCI/DTP through NMR and LC-MS analysis or a supplier Certificate of Analysis. The author wishes to thank the National Cancer Institute Developmental Therapeutics Program (NCI/DTP) for providing compounds present in this dissertation. Specifically, Approved Oncology Drugs Set XI (AOD XI).

Table 3: Compounds and reagents

Compound/Reagent	Vendor	Catalog No.	Stock Conc.	Working Conc.	Storage
Bio-acetoxime (BIA)	Fisher	38-741-0	10 mM	0-10 µM	-80 °C
Chiron99021 (C91)	MedChem Express	HY-10182	10 mM	0-10 µM	-80 °C
Gemcitabine	MedChem Express	HY-17026	10 mM	0-200 nM	-80 °C
Vorinostat	MedChem Express	HY-10221	10 mM	0-10 µM	-80 °C
FITC-dextran (70 kDa)	Sigma Aldrich	T1162-100MG	5 mg/mL	10 µg/mL	4 °C
Matrigel Growth Factor Reduced (GFR)	Corning	354230	Undiluted	50 µL/well	-20 °C
CellTiter-Glo 3D	Promega	G9683	----------	100 µL/well	-20 °C
Propidium Iodide	ThermoFisher Scientific	P3566	1 mg/mL	50 µg/mL	4 °C
RNaseA	ThermoFisher Scientific	EN0531	10 mg/mL	100 µg/mL	-20 °C

2.2.2 Antibodies

Antibodies were stored at 4 °C, -20 °C, or -80 °C, and working concentrations were determined according to the manufacturer's instructions. Working concentrations, vendor information, catalog numbers, and storage conditions for all antibodies are detailed in Table 4. These antibodies were used for immunofluorescence staining.

Table 4: Primary and Secondary Antibodies

Target	Dilution	Catalog #	Vendor	Host species
β-catenin	WB: 1/1000 IF: 1:100	51067-2-AP	Cell Signaling	rabbit
Total GSK3β	WB: 1/1000	9832S	Cell Signaling	mouse
H3K27M	IF: 1:1600	74829S	Cell Signaling	rabbit
H3K27me3	IF: 1:1600	9733S	Cell Signaling	rabbit
H3G34V	IF: 1/1000	Ab254401	Abcam	rabbit
b-actin	WB: 1/1000	4967L	Cell Signaling	mouse
Hoechst	IF: 1/2000	H21486	ThermoFisher Scientific	N/A
Phalloidin	IF: 1/800	8878	Cell Signaling	N/A
Anti-rabbit AlexaFluor-594	IF: 1/500	A32740	ThermoFisher Scientific	Goat

2.3 Experimental methods for Chapter 3

2.3.1 IncuCyte live-imaging and CellTiter-Glo (CTG) Viability

Live-cell proliferation assays were performed using the IncuCyte S3 Live-Cell Imaging and Analysis System (Sartorius, Cat# 4647). Pediatric HGG cells (SF8628, SU-DIPG-36, and KNS-42) were maintained in their appropriate culture medium according to the protocol in section 2.1.3 (Cell culture and passaging). Cells were seeded in triplicate in 96-well, black-walled, clear-bottomed tissue culture-treated plates (Corning, Cat# 3603) at a density of 3 × 10^3 cells per well in 50 µL. Plates were incubated overnight at 37°C with 5% CO_2 to allow for adherence. The next day, cells were treated with serial dilutions (1:2) of BIA or C91 or vehicle control (0.1% DMSO) in complete growth medium. Edge wells were avoided to minimize any variations arising from evaporation and edge-effect-driven variability.

For IncuCyte live-cell imaging assays, plates were transferred to the IncuCyte S3 (37°C with 5% CO_2) directly after treatment for phase-contrast, live-cell imaging at 10x magnification. Images were acquired every 2-4 hours over 72 hours, with 5 fields of view per well. %Confluence was calculated automatically via the IncuCyte software as the percentage of cells covering the well area. %Confluence growth curves represent mean ± SEM of n=3 independent experiments. Each independent experiment had n=3 technical replicate wells per condition. To calculate %Proliferation, %confluence values were normalized to their respective vehicle controls, and IC_{50} values were determined by using a 4-parameter logistic nonlinear regression. Statistical significance between cell compound conditions and cell lines was assessed using two-way ANOVA with Dunnett's multiple comparisons test vs vehicle control (α=0.05). All data were plotted using GraphPad Prism v10.6.1.

For the CellTiter-Glo (CTG) viability assays, at the assay endpoint, CTG 3D reagent was added to each well per the manufacturer's protocol, and the plate was placed on a plate shaker for 5 minutes at room temperature. Plates were then placed in the Molecular Devices SpectraMax M2 plate reader (Molecular Devices) to measure luminescence in each well. Viability curves represent mean ± SEM from n=3 independent experiments. Each independent experiment had n=3 technical replicate wells per condition. To calculate %viability, luminescence values were normalized to the vehicle control luminescence, and IC_{50} values were determined by using a 4-parameter logistic nonlinear regression. Statistical significance between cell compound conditions and cell lines was assessed using two-way ANOVA with Dunnett's multiple comparisons test vs vehicle control (α=0.05). All data were plotted using GraphPad Prism v10.6.1.

2.3.2 Flow Cytometry Cell Cycle Analysis

Cell cycle analysis was performed using propidium iodide (PI) DNA staining and flow cytometry. SU-DIPG-36s were maintained in their appropriate culture medium according to the protocol in section 2.1.3. Cells were seeded in 6-well TC plates (Corning, Cat# 3603) at a density of 3×10^4 cells per well in 2 mL of Working TSM. Plates were incubated overnight at 37°C with 5% CO_2 to allow for adherence.

Cells were treated with BIA or C91 diluted in Working TSM and incubated for 24 hours. After 24 hours of treatment, cells were washed with 1x PBS, lifted using a cell scraper or trypsin-EDTA (5 min, 37°C), centrifuged at 300xg for 3-5 minutes and then fixed in 70% ice-cold ethanol (2 hours at 4°C to overnight at -20°C). Fixed cells were washed twice with 1x PBS and then resuspended in PI/RNase A staining solution (50 µg/mL propidium iodide

(ThermoFisher, Cat# P3566) and 250 µg/mL RNase A (Qiagen, Cat#19101) and incubated at 37 °C for 30 minutes in the dark. Flow cytometry analysis was performed on the CytoFlex flow cytometer (Beckman Coulter) using the B610 channel (488 nm excitation, 610/20 nm emission). At least 20,000 events were recorded per sample, and the flow rate was set to low. FlowJo V10 flow cytometry analysis software, with Watson pragmatic modeling, was used to determine the percentages of cells in G1, S, and G2/M. Results are expressed as the percentage of cells per phase, mean ± SEM of n=3 biological replicates.

2.3.3 Transwell Migration

Transwell cell migration assays were performed in 24-well plates containing 6.5 mm-diameter, 5.0 µm pore polycarbonate membrane inserts (Corning, Cat# 3421). Diffuse midline glioma cells (SF8628 and SU-DIPG-36) were maintained in their appropriate culture medium according to the protocol in section 2.1.3. Cells were seeded in serum-free media at a density of 5×10^4 cells per well in 200 µL volumes, with +/- BIA/C91/vehicle control. Complete media containing 10% FBS was added to the lower chambers to serve as a chemoattractant (600 µL). Cells were incubated for 6 hours at 37°C with 5% CO_2 to allow for migration. After the 6-hour incubation, a cotton-tipped applicator was used to gently remove any non-migrated cells from the inner side of the transwell insert membrane. Cells that migrated to the basal side of the membrane were fixed in 70% ice-cold methanol/ethanol for 15 minutes and stained with DAPI (Thermo Fisher, Cat# 62248) for 10-15 minutes in the dark. Membranes were mounted to coverslips for imaging, and images of the full transwell membranes were acquired with an Olympus VS200 Slide Scanner and analyzed in ImageJ to count migrated nuclei. Results are expressed as % migrated (normalized to the control), with mean ± SEM from at least two independent experiments. Each independent experiment

had n=2-3 technical replicate wells per condition.

2.3.4 Wound Healing Scratch Assay

Cell migration of pediatric HGG cells was additionally assessed using the 2D wound-healing scratch assay. Pediatric HGG cells (SF8628, SU-DIPG-36, and KNS-42) were maintained in their appropriate culture medium according to the protocol in section 2.1.3. Cells were seeded in triplicate in either 6-well (Corning, Cat# 3603) or 24-well TC-treated plates (Corning, Cat# 3603) at an appropriate density to achieve 90-100% confluence within 24 hours and incubated overnight at 37°C with 5% CO_2 to allow cell adherence.

Confluent cell monolayers were scratched along the center of each well using a sterile 1mm P200 pipette tip. Each well was gently washed with 1x PBS twice to remove detached cells, and 2 mL of fresh medium containing vehicle or BIA/C91 was added. Plates were immediately transferred to the IncuCyte S3 live-cell imaging and analysis system for real-time imaging, capturing the entire well at 4x magnification for 24 hours. Results are expressed as the percentage of wound closure, with mean ± SEM, from 2-3 independent experiments. Each biological replicate had n=2-3 technical replicate wells per condition. One-way ANOVA with Dunnett's multiple comparisons vs vehicle test (α=0.05) and two-way ANOVA with Sidak's to compare between cell lines.

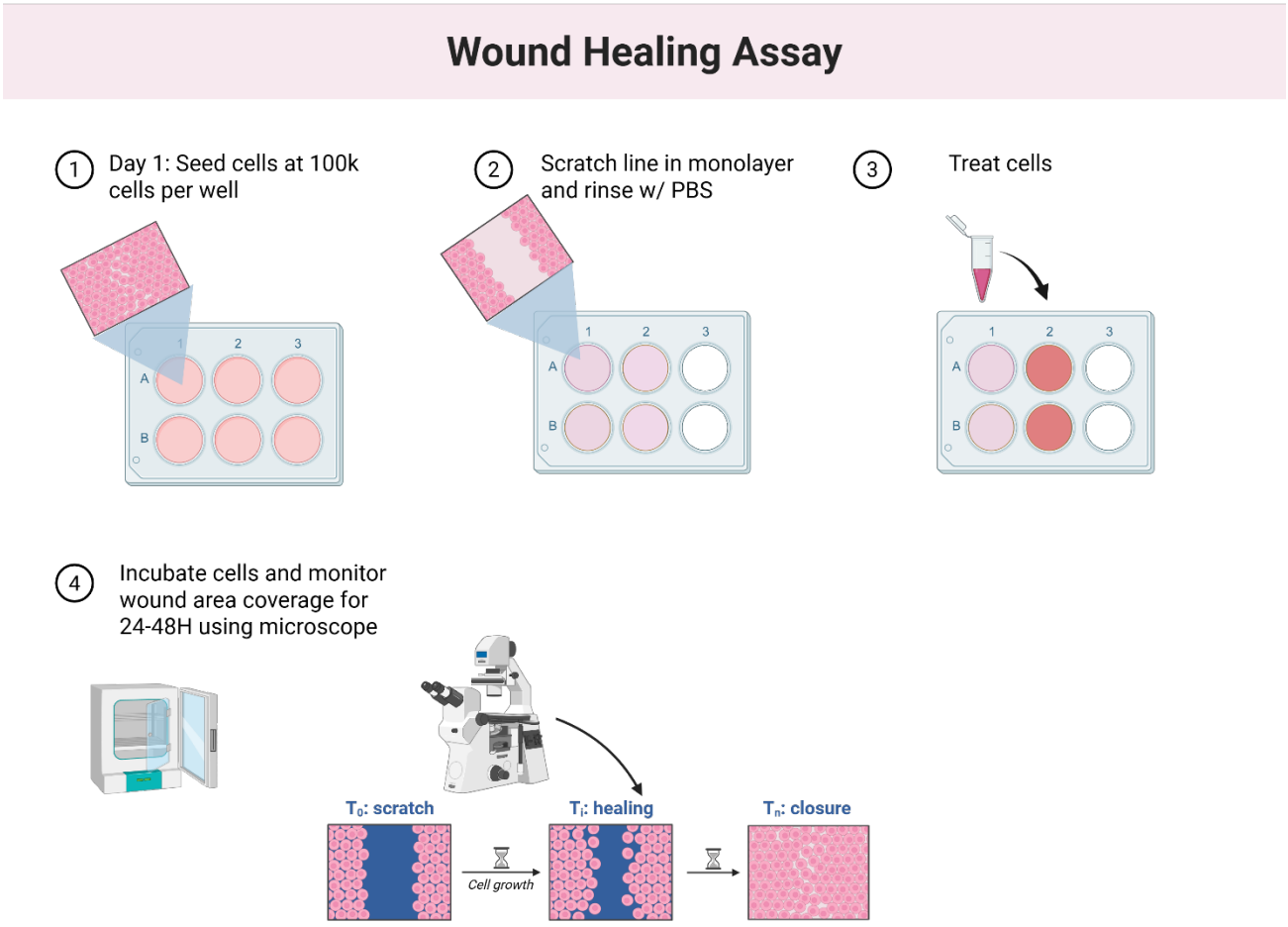

Figure 2.2: Schematic of the Scratch wound-healing assay. Wound healing assay used to measure collective migration after scratch in a confluent monolayer. T_0 shows uniform scratch, T_i shows wound closure beginning, T_n shows complete wound closure. Created in https://BioRender.com.

2.4 Experimental methods for Chapter 4

2.4.1 BBB/BTB spheroid model culture and setup

BBB/BTB barrier co-culture spheroids were created using hCMEC/D3s, astrocytes, and pericytes plated together in equal amounts (1000 cells per well) in BBB working medium (**Table 5**). All cell lines were cultured according to Section 2.1.3 and grown in their respective media: hCMEC/D3- basal endothelial cell medium (ScienCell, Cat #1001), human primary astrocytes- basal astrocyte medium (ScienCell, Cat #1801), and human primary pericytes- basal pericyte medium (ScienCell, Cat #1201).

BBB cells (hCMEC, astrocyte, and pericyte) were grown in low-adherent round-bottom 96-well plates at 1,000 cells per well each (3,000 cells total) and allowed to form for over 48 hours before drug treatments were added. For BTB spheroids, DMG cells were plated at 500 cells per well and allowed to form for 24 hours before the addition of the BBB co-culture. Once hCMECs, astrocytes, and pericytes were added to each well, spheroids were allowed to form for over 48 hours before drug treatment was initiated.

Table 5: Working BBB Medium

Reagent	Vendor	Catalog No.	Volume
Basal Endothelial Medium	ScienCell	1001	500 mL
Endothelial growth supplements	ScienCell	1052	5 mL
Heat Inactivated Human Serum 2%	GeminiBio	100-512-100	10 mL

2.4.2 Dextran and antibody uptake assays

BBB/BTB spheroids were grown for 48 hours and then treated with BIA or C91 at the indicated doses for 24 hours. After 24 hours, spheroids were collected and cultured with a 70 kDa fluorescein isothiocyanate (FITC)–conjugated fluorescent dextran (Millipore Sigma, Cat# 90718) at a concentration of 10 µL/mL for 4 hours or with an Alexa Fluor 488-conjugated IgG secondary antibody (ThermoFisher, Cat #A32814) at a concentration of 8 µL/mL for 24 hours. Once incubation with dextran or antibody was complete, spheroids were fixed in 10% formalin and imaged using confocal microscopy. Each independent experiment had n=5 spheroids per condition imaged and analyzed. Fluorescent dextran or AF488 mean fluorescent intensity was quantified using ImageJ (National Institutes of Health).

2.4.3 Trans-endothelial electrical resistance

Real-time endothelial barrier function was assessed using the Electric Cell-substrate Impedance Sensing (ECIS) system. HCMEC/D3 cells were cultured as described in Section 2.1.3. Cells were plated in 8W10E+ PET eight-well arrays (Applied Biophysics) at a density of 30,000 cells per well in 400 µL. These arrays were placed in a pre-stabilized ECIS Z-Theta instrument. Using the ECIS Z-Theta software (Applied Biophysics), trans endothelial electrical resistance (TEER) was measured every 30 minutes at 4000 and 64,000 Hz (to reflect overall barrier integrity and tight junction changes, respectively). Barrier formation of the hCMECs was monitored until a resistance plateau was reached, at which point capacitance was ~10 nF at 64,000 Hz (48 to 72 hours). Drug treatments began once the plateau was reached, and cells were treated with BIA or C91 directly into each well. Cells received daily replenishments of fresh drug-containing media over 5 days. Resistance (ohms) and capacitance (nF) were recorded. Plots of resistance values at 4,000 Hz were

generated using GraphPad Prism v10.6.1.

2.4.4 Tube Formation Assay

Matrigel growth factor-reduced (GFR) basement membrane matrix (Corning, Cat # 354230) was used for the tube formation assay. GFR-Matrigel was thawed overnight on ice at 4 °C. The product was kept on ice and dispensed using pre-cooled pipette tips and tubes into 300µL aliquots (VWR, Cat # 76322-154). These aliquots were frozen immediately to avoid multiple freeze thaws. Flat-bottom, tissue-treated, 96-well plates (Corning, Cat # CLS3599) were coated with GFR Matrigel. After thawing the appropriate number of GRF-Matrigel aliquots overnight on ice at 4 °C, the GFR-Matrigel was mixed to homogeneity and kept on ice. Pipette tips (VWR, Cat # 76322-152) were pre-cooled as GFR-Matrigel gels extremely quickly. Making sure to avoid air bubbles, 50 µL of the GFR-Matrigel was added to each well, and incubated at 37 °C for at least 30 minutes. The remaining liquid was removed from the plate without disturbing the GRF-Matrigel. HBMEC's were cultured in complete ECM, and a cell suspension was prepared by trypsinizing the cells and resuspending them in complete ECM. VEGF (ThermoFisher, Cat # 100-20-10UG) was added to the culture medium at 50 ng/mL. HBMECs were counted, and 15,000 cells were added per well in a 100 µL suspension of ECM or ECM+VEGF, then incubated for 6 hours at 37 °C.

2.5 Experimental methods for Chapter 5

1.5.1 Drug Screen

High-throughput drug screening was conducted using an NIH FDA-approved drug panel. pHGG cells (SF8628, SU-DIPG-36, and KNS-42) were maintained in their appropriate culture medium according to the protocol in section 2.1.3. Cells were seeded in triplicate in 96-well, black-walled, clear-bottomed tissue culture-treated plates (Corning, Cat# 3603) at a density of 3×10^3 cells per well in 50 µL volumes. Plates were incubated overnight at 37°C with 5% CO_2 to allow for adherence. The next day, cells were treated with a single dose (1 µM) of the NIH FDA-approved drug library, with or without 1 µM BIA, and incubated for 72-96 hours at 37°C with 5% CO_2. Cell viability was evaluated using the CellTiter Glo 2.0 (Promega, Cat# G9242) luminescent assay reagent and quantified by measuring luminescence with a Molecular Devices SpectraMax M2 plate reader. Top hits were plotted using GraphPad Prism v10.6.1.

2.5.2 Combination IC_{50}

Cell viability assays were performed using the CellTiter-Glo 3D cell viability assay (Promega, Cat# G9683). Pediatric HGG cells (SF8628, SU-DIPG-36, and KNS-42) were maintained in their appropriate culture medium according to the protocol in section 2.1.3. Cells were seeded in triplicate in 96-well, black-walled, clear-bottomed tissue culture-treated plates (Corning, Cat# 3603) at a density of 3×10^3 cells per well in 50 µL volumes. Plates were incubated overnight at 37°C with 5% CO_2 to allow for adherence.

The next day, cells were treated with serial dilutions (1:2) of Gemcitabine (0.6-10 µM), Vorinostat (0.6-10 µM), or vehicle control (0.1% DMSO) with or without BIA/C91 (BIA:

500nM/1 μM and C91: 1 μM) in complete growth medium. Plates were incubated for 72 hours at 37°C with 5% CO_2. At the assay endpoint, CellTiter-Glo 3D reagent was added, and luminescence was obtained using the SpectraMax M2 plate reader. Viability curves represent mean ± SEM from n=3 biological replicates. Each biological replicate had n=3 technical replicate wells per condition. To calculate %viability, luminescence values were normalized to the vehicle control luminescence, and IC_{50} values were determined by using a 4-parameter logistic nonlinear regression. Statistical significance between cell compound conditions and cell lines was assessed using two-way ANOVA with Dunnett's multiple comparisons test vs vehicle control (α=0.05). All data were plotted using GraphPad Prism v10.6.1.

2.5.3 TOPFlash WNT reporter assay

To confirm canonical WNT/β-catenin pathway activation of our GSK-3 inhibitors, BIA and C91, the TCF/LEF reporter plasmid TOPflash assay was performed using G9-pCDH (G9) cells. G9-TCF cells were engineered by overexpressing a luciferase gene (Luc2) controlled by a TCF7-recognized promoter in the G9 cell line. G9 -TCF cells were maintained in their appropriate culture medium according to the protocol in section 2.1.3. G9-TCF cells were seeded in 96-well, black-walled, clear-bottomed tissue culture-treated plates (Corning, Cat# 3603) at a density of 1×10^4 cells per well with or without BIA or C91 in 200 μL volumes. Cells were incubated for 24 hours at 37 °C with 5% CO_2. After 24 hours, the supernatant from each well was removed, and cells were lysed with 20 μL of lysis buffer (ThermoFisher Scientific, Cat# 89900) per well. Plates were incubated with the lysis buffer on a plate shaker at room temperature for 15 minutes, protected from light. After 15 minutes, 100 μL of the luciferase assay reagent (Promega, Cat # E151A) was added to each well, and luminescence was read immediately using the Spectra Max M2 plate reader. Data was plotted as fold

change normalized to the control and plots were made using GraphPad Prism v10.6.1.

2.5.4 Lysate Collection

Cells were harvested, spun down, and the old supernatant was aspirated. Cells were counted and plated at 500,000 cells per well in a 6-well plate with 2 wells per condition. Cells were seeded overnight, then treated the next day with compounds at the desired concentrations for their designated time points, and stored in the incubator at 37 °C. Once the time point was reached, the cells were harvested, spun down, and the supernatant was aspirated. Cells were then washed twice with cold DPBS (Gibco, Cat # 14190250) and lysed with RIPA buffer.

2.5.5 RIPA Lysis

Complete RIPA buffer was prepared by diluting protease/phosphatase inhibitors (Cell Signaling, Cat # 5872S) 1:100 in RIPA buffer (ThermoFisher Scientific, Cat # 89900), added to the cell pellets, and then pipetted up and down vigorously or vortexed to resuspend the pellet. Eppendorf tubes (Eppendorf, Cat # 0030123611) containing the cell suspension remained on ice for 25 minutes, with 5-minute vortexing intervals. The tubes were then centrifuged at 14,000 × g for 15 minutes to pellet the cell debris, and the supernatant was collected into a new tube for protein quantification using the Pierce assay.

2.5.6 Pierce Assay

To prep the samples for the Pierce assay, 6 µL of sample lysate was diluted into 24 µL of RIPA buffer and vortexed. A serial dilution was then prepared to create a standard curve using BSA (Sigma Aldrich, Cat # 1003419901) and RIPA buffer (standards ranged

from 2,000 µL/mL to 0 µL/mL). 10 µL of each standard and diluted sample was pipetted in duplicate into the respective wells of a clear 96-well plate (Corning, CLS3599). 150 µL of Pierce assay reagent was added to each well, and the plate was covered with aluminum foil and placed on a plate shaker for 5 minutes. Once the 5 minutes were complete, the absorbance of each well was taken using a plate reader (SpectraMax M2, Molecular Devices) at 660nm.

2.5.7 Western Blot

Lysates were prepared by adding β-Mercaptoethanol (EMD Millipore, Cat # 444203), 4x Laemmli Buffer (Bio-Rad, Cat # 1610747), and Milli-Q water. The samples were then heated for 10 minutes at 99°C (USA Scientific, Dry Bath BSH1002). Samples were centrifuged (Eppendorf, Cat # 5425R), vortexed (Fisher Scientific, Cat #12-812), and then placed on ice. Running buffer was prepared by diluting 10x Tris/Glycine/SDS Buffer (Bio-Rad, Cat # 1610772) 1:10 with Milli-Q water. Samples were loaded in Mini-Protean TGX gels (Bio-Rad, Cat # 4561033) in a Mini-Protean Tetra Cell (Bio-Rad, Cat # 1658004). The gels were run at 90V for the first 15 minutes, then at 120V for 60 minutes (Bio-Rad, Cat # 1645052), or until the samples reached the bottom of the gel.

To transfer samples from the gel to a PVDF membrane, the Trans-Blot Turbo Transfer system (Bio-Rad, Cat #1704150) was used on the mixed MW setting, running at 1.3A, 25V for 7 minutes. The membrane was then placed in TBST to rehydrate and condition it for 5 minutes. Once the membrane was rehydrated, a Ponceau S stain (Cell Signaling, 59803) was used to confirm complete transfer, and then the membrane was rinsed with TBST. 1x TBST was prepared using a 1:10 dilution of 10x TRIS-buffered saline with 0.5% Tween 20

(ThermoFisher Scientific, Cat # J60448-K2) and Milli-Q water (EMD-Millipore, Q-Pod Cat # ZIQP0D000). After washing, the membrane was blocked with 5% BSA-TBST (Sigma Aldrich, Cat # 1003419901) for 30 minutes. After blocking the membrane, it was washed three times, rocking in TBST for 10 minutes each. The membrane was incubated overnight at 4 °C with the primary antibody, rocking in 5% BSA-TBST (Sigma, Cat # 1003419901). The next day, the membrane was washed three times by rocking in TBST for 10 minutes, then incubated at room temperature in 5% BSA-TBST with the secondary antibody for 30 minutes [Jackson ImmunoResearch: Anti-Rabbit (Cat # 111-035-003), Anti-Mouse (Cat # 115-035-003)]. The membrane was washed three times, rocking in TBST for 10 minutes each. Reactive bands were visualized with an ECL substrate, SuperSignal West Pico (ThermoFisher Scientific, Cat # 34577), using the Bio-Rad Gel imaging system (Biorad ChemiDoc MP imaging system) To strip the membrane, stripping buffer (ThermoFisher Scientific, Cat # 46430) was placed on the membrane for 10 minutes, then washed 3x with TBST for 10 minutes each to remove residual reagent.

2.5.8 Immunofluorescence staining

Cells were grown on 8-well chamber slides (Millicell EZ Slide, Cat# PEZGS0816) and treated with either 1 μM BIA or 3 μM C91 for 24 hours. After 24 hours, the cells were fixed with 10% formalin (Sigma Aldrich Cat # HT501128-4L) for 15 minutes at room temperature. The formalin was removed, and fixed cells were permeabilized for 20 minutes using 0.1% Triton X-100 in PBS (ThermoFisher Scientific, Cat# AAA16046AP). After permeabilization, cells were washed 3x with PBS, then blocked in 1% bovine serum albumin (BSA) in PBS for 1 hour. Once blocking was complete, cells were then stained with primary antibodies prepared in blocking solution (**Table 2**) and incubated overnight at 4 °C on a rocker. The next

day, cells were washed with PBS 3x, and the corresponding secondary antibody (anti-rabbit) AlexaFluor-594 (1:500) prepared in blocking solution was added, and cells were incubated at room temperature for 1 hour. Once secondary antibody incubation was complete, slides were mounted using Fluoromount (ThermoFisher Scientific, Cat# 00-4958-02) and allowed to dry for at least 24 hours and stored at room temperature until imaging. Cells were imaged using a Zeiss LSM800 confocal microscope, and fluorescence was detected by illuminating the samples with a laser adjusted to the excitation wavelength of the individual dyes (Alexa Fluor-594, Phalloidin-488, and Hoechst). The same settings (exposure, laser power) were applied to all conditions for direct comparison.

2.6 Data Analysis and Quantification

All quantitative data were analyzed using GraphPad Prism v10.6.1. Continuous variables are expressed as mean ± SEM from n≥3 independent biological replicates unless otherwise stated. Confluence and viability curves were fit to a 4-parameter logistic nonlinear regression, and IC_{50} values were calculated using the inhibitor vs response (variable slope) model. Cell cycle distributions were compared using one-way ANOVA with Dunnett's post hoc test vs vehicle control. For the scratch assay, migration/invasion was quantified as % wound closure using ImageJ to measure wound area. For the transwell assay, migration was quantified as % migrated, and all conditions were normalized to the vehicle control using ImageJ to count the number of migrated cells.

CHAPTER 3: DIFFUSE MIDLINE GLIOMA BIOLOGY

3.1 Overview and Significance

pHGGs are the second most common childhood CNS malignant tumors and the leading cause of cancer-related deaths in children [2,3]. Among these DMGs are rare, aggressive, and debilitating tumors that represent a particularly devastating subtype with a median survival of less than a year [6,20]. Traditional chemotherapeutics have been shown to be ineffective, and the current standard of care, focal radiation therapy, only helps to mitigate symptoms and partially extend progression-free survival for 5-7 months; however, tumor growth recurrence is inevitable [58,65].

Previous studies from the Lawler lab and others have shown that the indirubin derivative BIA possesses anti-invasive properties, decreased tumor cell growth in glioma cells, and enhanced survival in glioblastoma xenograft models [93,106,113]. Among the known targets of BIA, GSK-3 is a particularly encouraging therapeutic target for DMG treatment, and its inhibition represents a promising strategy to improve DMG therapy by limiting tumor cell survival, migration, and motility [78-83]. In this chapter, I sought to address these gaps and elucidate the underlying mechanisms of BIA by investigating the pharmacological effects of selective GSK-3 inhibition on pHGG biology and behavior by comparing it with CHIR99021 (C91), a selective GSK-3 inhibitor [141]. My hypothesis was that GSK-3 inhibition could be an effective therapeutic approach for DMG by targeting tumor cell proliferation, viability, and migration, and that, unlike BIA's broader kinase-inhibition profile, selective GSK-3 inhibitors such as C91 may produce effects similar to BIA while mitigating off-target toxicity.

3.2 Results

3.2.1 BIA and C91 inhibit cell proliferation in pHGG cell lines

Uncontrollable proliferation is a well-established feature of DMG, driving disease progression and limiting the efficacy of chemotherapeutic and radiotherapeutic treatments [142]. Previous studies have implicated GSK-3 in the regulation of cell motility and proliferation in many cell types, including glioma cells [106,117]. To assess the role of GSK-3 inhibition on pHGG tumor cell proliferation and growth dynamics over time, I used the IncuCyte S3 automated live-cell imaging system to image three patient-derived pHGG cell lines. Cells were treated with either BIA or C91 at a 1:2 serial dilution, prepared from a 10 mM DMSO stock, or with 0.1% DMSO vehicle control. Plates were transferred to the IncuCyte S3 immediately after treatment for phase-contrast imaging (10x magnification, 5 fields of view/well) every 4 hours over a 72-hour treatment period. Conditions were repeated in triplicate. % Confluence was calculated as the percentage of cells covering the well area, and the data was plotted using GraphPad Prism v10.6.1.

3.2.2 Time-course confluence demonstrates differential growth kinetics between pHGG cell lines

The vehicle-treated control cells were used to determine the baseline growth curve for each cell line. The H3.3K27M bearing cells (SF8628) grew the fastest and were approximately 85% confluent after 72 hours, the H3.1K27M bearing cells (SU-DIPG-36) grew at a moderate rate and reached approximately 60% confluence after 72 hours, and the H3.3G34V bearing KNS-42 cells grew the slowest and reached approximately 41% confluency at the 72-hour time point. The varying growth rates indicate that the histone mutations exhibit distinct growth kinetics and properties that may influence cell growth. BIA

showed a drastic effect on the growth of all three lines, with effects beginning at 12 hours in the SU-DIPG-36s, 24 hours in the SF8628s, and 36 hours in the slower-growing KNS-42 cell line (**Figure 3.1A-C**). These responses were dose-dependent, as lower doses (0-1.25 μM) exhibited more modest effects on confluence, and higher concentrations (5-10 μM) resulted in a near complete inhibition of growth. In the case of the SU-DIPG-36s, all BIA concentrations resulted in a complete halt of proliferation, holding a plateau of 12-19% confluence between 12-72 hours, indicating possible strong cytotoxic effects or cell cycle arrest. This was not observed in cells treated with the specific GSK-3 inhibitor C91, with a marked reduction in the effect across all three lines (**Figure 3.1D-F**). This was illustrated in the timing of growth arrest, which in SU-DIPG-36 cells began 24 hours post-treatment, in SF8628 cells began 36 hours post-treatment, and in KNS-42 cells began 48 hours post-treatment, whereas decreases in confluence were still observed in a dose-dependent manner but were less severe overall than BIA treatment, which may indicate that BIA's broader multi-kinase activity may be also accessing other mechanisms of cellular growth and proliferation that enables BIA to have more profound effects than the more specific activity of C91.

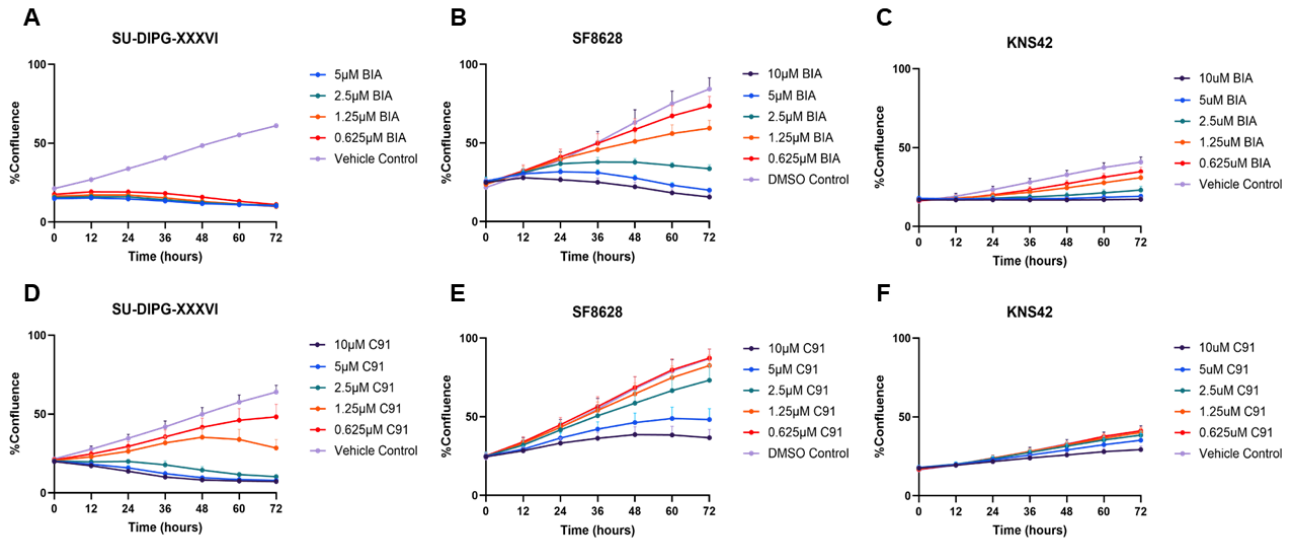

Figure 3.1: Real-time proliferation kinetics on pHGG cell lines. Cells were seeded at 3x10^3 cells/well SU-DIPG-36 **(A/D),** SF8628 **(B/E), and** SF8628 **(C/F)** in a flat-bottom 96-well plate and allowed to adhere overnight. Cells were then treated with culture medium or drugs (BIA or C91 at 10, 5, 2.5, 1.25, and 0.63 μM in DMSO). %Confluence over time was determined by the percentage of cells covering the well area at each time point. Graphs show mean ± SEM of n=3 individual experiments performed with each condition in triplicate.

3.2.3 72h endpoint analysis showed drug and concentration effects

To assess the effects of BIA and C91 at our 72-hour endpoint, we quantified proliferation effects using grouped bar plots and normalizing each condition to the vehicle control (%confluence). Statistical analysis using two-way ANOVA (Sidak's multiple-comparison post hoc test, α = 0.05) was used to enable direct comparisons among cell lines (**Fig. 3.2 A-C**). This allowed us to quantify the effects of BIA and C91 in each cell line and compare mutation-specific growth-inhibition effects. In the SF8628s, two-way ANOVA revealed significant main drug and concentration effects were observed (****p<0.0001 for both), however no significant interaction between the two was seen, indicating that overall they possessed a parallel reduction trend with BIA outperforming C91 in terms of overall

potency, with the first observed divergence in response beginning at 2.5 μM and the highest concentration (10 μM) reducing %confluence to ~17% with BIA and ~39% with C91 emphasizing their potency differences. Significant concentration-dependent effects were observed at 2.5 μM and 5 μM (**p=0.0002, *p=0.0112).

Consistent with their full-time course analysis profile, the SU-DIPG-36s showed the most dramatic response to both BIA and C91 treatments, emphasizing their mutation-specific (H3.1K27M) vulnerability to GSK-3 inhibition. Similar to the SF8628s, significant main drug and concentration effects were observed, with an additional interaction effect found between the two (****p<0.0001, for all effects). These drastic effects on proliferation were apparent as low as 0.625 μM treatment and 1.25 μM (****p=0.0001, **p=0.0083). BIA treatment resulted in complete growth arrest at the lowest tested concentration (0.625 μM), whereas much higher concentrations of C91 (2.5 μM) were necessary to achieve a similar reduction of proliferation to <20%. Lastly, two-way ANOVA statistical analysis of the pediatric hemispheric glioma cell line, KNS-42s, also showed significant main effects on the drug and concentration and an interaction between the two (****p<0.0001, ****p<0.0001, and *p=0.0485, respectively), mirroring the observed effects on the SF8628 cell line. Differences between BIA and C91 in growth inhibition were observed beginning at the midpoint dose of 2.5 μM (**p=0.0023) and continued through the final two tested concentrations, 5 μM (**p=0.0013) and 10 μM (*p=0.0235).

The significant drug x concentration interaction seen in both the SU-DIPG-36s and KNS-42s, but not the SF8628s, may reflect the differences in their baseline growth rates or signaling pathway interactions, though further mechanistic studies are needed to clarify these

relationships. Altogether, these results highlight BIA's superior potency across pHGG cell lines, with hypersensitivity observed in the H3.1K27M-bearing cell line SU-DIPG-36, suggesting a potential mutation-specific vulnerability that should be further explored to assess clinical exploitability.

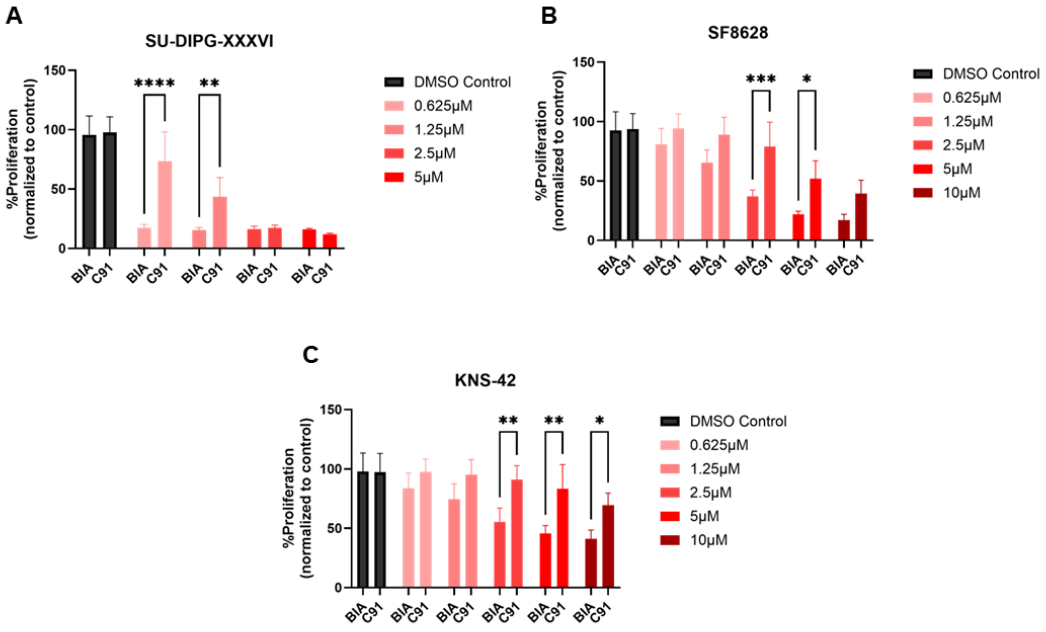

Figure 3.2: 72-hour endpoint dose-response comparison reveals BIA's superior potency across pHGG subtypes. Cells were seeded at 3x10^3 cells/well SU-DIPG-36 **(A),** SF8628 **(B),** and KNS-42 **(C)** in a flat-bottom 96-well plate and allowed to adhere overnight. Cells were then treated with culture medium or drugs (BIA or C91 at 10, 5, 2.5, 1.25, and 0.63 μM in DMSO). %Proliferation = % confluence normalized to the vehicle control. Graphs show mean ± SEM of n=3 individual experiments performed with each condition in triplicate.

3.2.4 Proliferation IC_{50} analysis reveals DMG-specific sensitivity to GSK-3 inhibition

To better understand the cytostatic effects of our GSK-3 inhibitors on the pHGG cell lines, we compared the highest tested concentrations between the cell lines. At the 72-hour endpoint, the highest tested BIA concentration, 10 μM for SF8628/KNS-42 and 5μM for SU-DIPG-36, reduced mean confluence to 17.2% in the SF8628 (H3.3K27M), 16% in the SU-DIPG-36 (H3.1K27M), and 41.2% in the KNS-42s (H3.3G34V) (**Fig. 3.3A-C**). These showed much stronger endpoint confluence reduction than C91 at the same concentration, with reductions of 39.4%, 12.%, and 69.4%, respectively (n=3 individual experiments, 3 wells/condition). These drastic differences at the maximal tested concentrations highlight BIA's ability to nearly completely arrest proliferation in the diffuse midline glioma cell lines (SU-DIPG-36, SF8628) vs the more resistant hemispheric glioma cell line, KNS-42.

We further explored the full potency of these inhibitors by deriving confluence IC_{50} values from these endpoint values normalized to the vehicle controls. We fitted these values to a 4-parameter logistic model using GraphPad Prism v10.6.1. Consistent with the overall response in confluence inhibition observed across the previous endpoints, the SU-DIPG-36s continued to be the most responsive cell line, exhibiting strong sensitivity to BIA treatment with a submicromolar IC_{50} value of 0.21 μM and an IC_{50} value for C91 of 1.00 μM (**Fig. 3.4A).** Although not as sensitive as their H3.1K27M counterpart, the SF8628s still exhibited high sensitivity to BIA treatment, with an IC_{50} of 1.77 μM and an IC_{50} of 3.56 μM for the selective GSK-3 inhibitor, C91 (**Fig. 3.4B**). An IC_{50} for the KNS-42s could not be determined within the tested concentration range because the highest dose only achieved a maximal reduction in proliferation of 41% with BIA treatment and 69% with C91 treatment. This resulted in a poor fit of the analysis, making the IC_{50} calculations inaccurate. Despite not being able to calculate

a specific confluence IC_{50} for the KNS-42s, this drastic difference in response between the DMG cell lines and the KNS-42s highlights the vulnerability of the H3K27M-bearing cell lines to the effects of both BIA and C91 on proliferation. This is likely due to the highly dysregulated proliferative nature of DMG that drives its resistance to SOC treatments, contributing to their aggressive and ultimately fatal progression. BIA demonstrating consistently greater potency than C91 across all cell lines indicates that GSK-3 inhibition is not the only mechanism driving its antiproliferative effects and that its multi-kinase activity could provide a unique approach to DMG treatment.

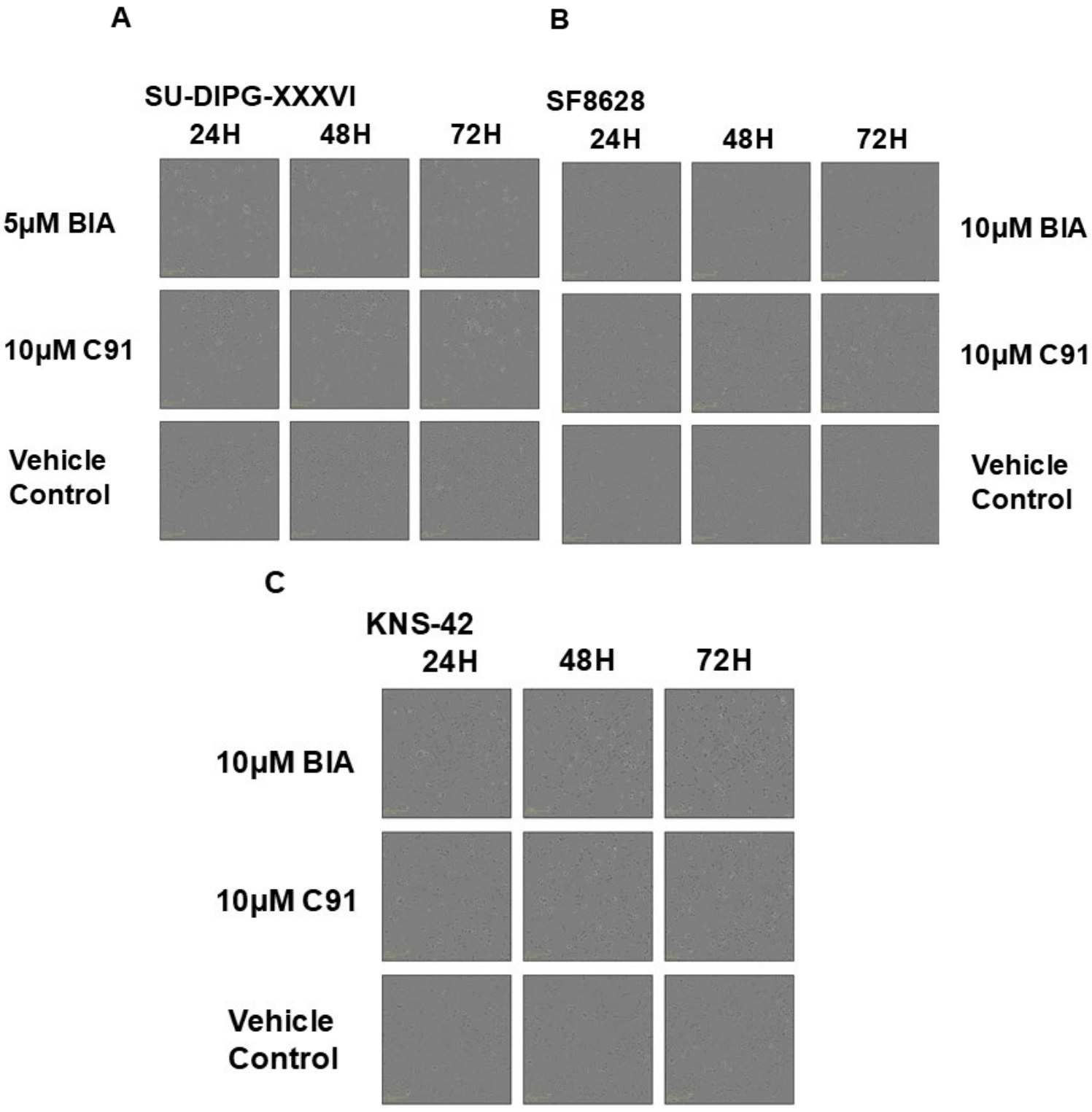

Figure 3.3: IncuCyte Phase-contrast images of pHGG cell lines. (**A**) Images of SU-DIPG-36s, (**B**) SF8628s, and (**C**) KNS-42s at the highest BIA/C91 concentrations at 24, 48, and 72H time points. Cells seeded 3×10^3/well. IC_{50} from nonlinear regression. Representative images of confluence (n=3 individual experiments, with technical triplicates).

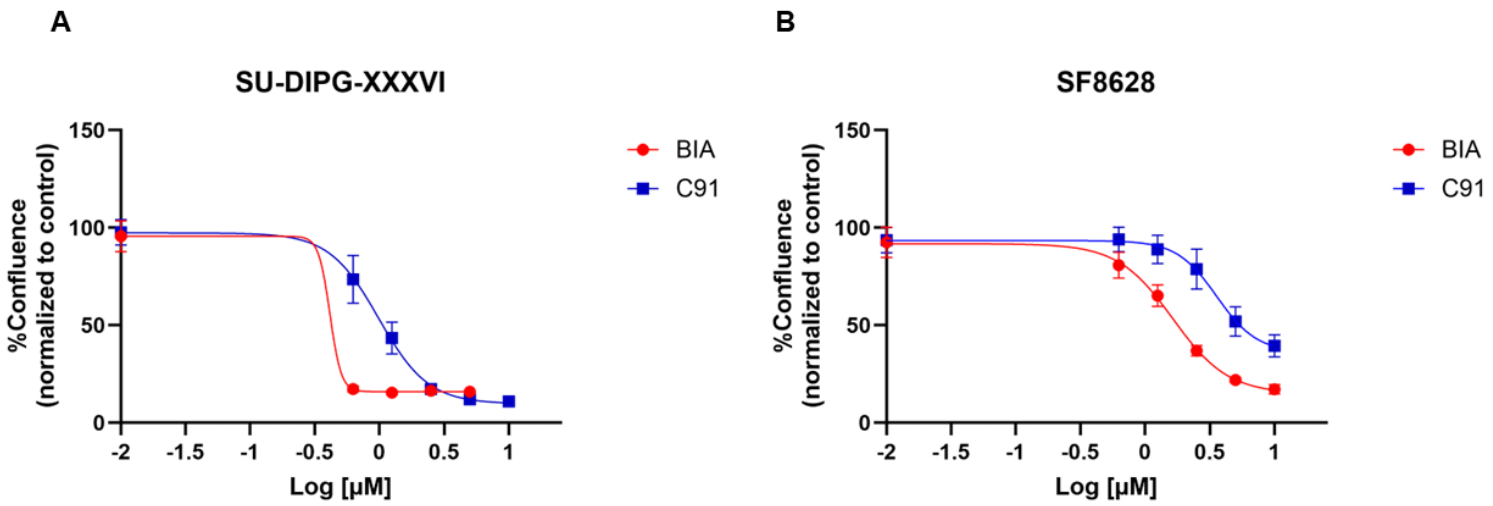

Figure 3.4: Proliferation IC_{50} curves in pHGG cell lines. Real-time IncuCyte kinetics post-drug treatment. (**A**) SU-DIPG-36 Proliferation IC_{50} curve and (**B**) Images of SU-DIPG-36s at 5 μM BIA and 10 μM C91 at 24, 48, and 72H time points. (**C**) SF8628 Proliferation IC_{50} curve and (**D**) Images of SF8628s at 10 μM BIA/C91 at 24, 48, and 72H time points. Cells seeded 3×10^3/well. IC_{50} was generated using nonlinear regression. Graphs show mean ± SEM of n=3 individual experiments performed with each condition in triplicate.

3.2.5 GSK-3 inhibition reduces viability in pHGG cell lines

Another hallmark driving pediatric high-grade glioma recurrence and resistance is post-radiation compensatory proliferation, making it important to identify therapeutic treatments that not only suppress growth but also effectively kill tumor cells [142]. To complement the effects of these inhibitors on inhibiting proliferative growth observed in the live-cell imaging assay, we evaluated the cytotoxic efficacy of our compounds using the luminescent ATP-based CellTiter-Glo assay. This helped to differentiate between the cytostatic and cytotoxic effects of the same dose-response curve tested above at the established 72-hour endpoint. Cells were treated with serial dilutions of BIA, C91, or a 0.1% DMSO vehicle control for 72 hours, and the conditions were repeated in technical triplicate to increase statistical rigor. Once the 72-hour endpoint was reached, cells were lysed using the CellTiter-Glo assay reagent, and luminescence was measured using a SpectraMax

spectrometer. Luminescence values were normalized to the mean vehicle-control luminescence and fitted using a 4-parameter logistic nonlinear regression model in GraphPad Prism v10.6.1 to generate IC_{50} values (**Fig. 3.5A-C**).

Similarly to the proliferation results, the SU-DIPG-36s remained the most sensitive line to both BIA and C91 treatment, with IC_{50}s of 1.4 μM and 2.45 μM, respectively, with this trend in sensitivity followed by its H3K27M counterpart, SF8628, with IC_{50}s of 1.84 μM and 4.6 μM, respectively. The KNS-42s remained the most resistant to both inhibitors, with IC_{50}s of 4.08 μM for BIA and 6.14 μM for C91, consistent with their high resistance observed in the proliferation assays. In the SF8628s and SU-DIPG-36s, two-way ANOVA revealed significant main drug x concentration effects, indicating a parallel overall trend in viability reduction, with BIA outperforming C91 in potency and showing a significantly more sensitive response than the KNS-42s. Notably, the more pronounced effect on viability in the KNS-42s, despite their strong proliferation resistance response, reveals the differences of the different mutations and their responses to GSK-3 inhibition as they relate to tumor growth and viability. The continued enhanced potency of BIA over C91 suggests that its multi-kinase activity may engage additional pathways beyond GSK-3 inhibition. Additionally, the shift toward higher IC_{50} values from the IncuCyte proliferation assays to CTG viability confirms that the effects observed at the lower concentrations of both BIA and C91 were primarily cytostatic, with higher doses needed for any observed cytotoxic effects. While C91 effectively inhibited proliferation and increased cell viability, it could not fully recapitulate the potent effects of BIA, highlighting the potential value of multi-kinase targeting for pHGG treatment.

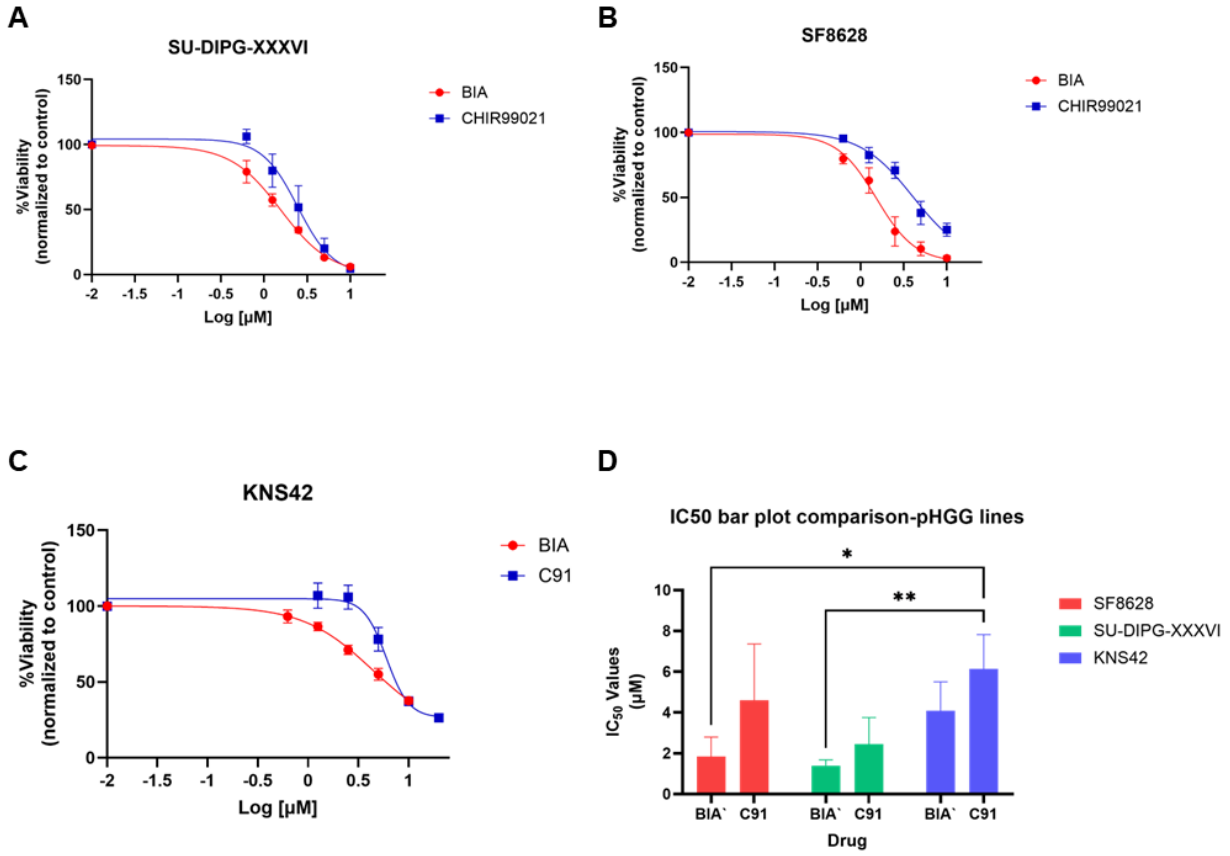

Figure 3.5: CTG viability IC_{50} curves across pHGG cell lines. Dose-response curves from CellTiter-Glo endpoint assay (72h) in **(A)** SU-DIPG-36, **(B)** SF8628, and **(C)** KNS-42. Nonlinear regression (log[inhibitor] vs response) yields IC_{50} values. **(D)** IC_{50} comparisons between pHGG cell lines. Mean ± SEM, n=3 triplicates.

3.2.6 BIA and C91 effects on cell cycle phase progression

To determine if the anti-proliferative effects observed in the pHGG cell lines by BIA and C91 operate through GSK-3-mediated cell cycle regulation or another regulatory pathway, we investigated cell cycle progression using propidium iodide (PI) staining via flow cytometry. In addition to being GSK-3 inhibitors, indirubin derivatives have been established as potent CDK inhibitors with high affinity for CDK ATP-binding sites [105]. This is seen through arrest in the G1, G2/S, or G2/M phases [109,110]. Selective GSK-3 inhibitors are known to inhibit cell cycle progression by arresting cells in either G1 or G2/M phases by preventing cyclin D1

degradation and inducing apoptosis [143]. PI cell cycle analysis was performed in the SU-DIPG-36 cell line as they were the most responsive line from our proliferation and viability studies. The cells were treated with either BIA (500 nM, 1 μM) or C91 (1 μM, 3 μM) for 24 hours before fixation with ice-cold 70% ethanol, RNaseA incubation (100 μg/mL), and PI staining (50 μg/mL) for analysis of DNA content using a Beckman Coulter flow cytometer. Data was analyzed using FlowJo v10 for cell-cycle phase (G1, S, G2/M) gating. Vehicle-treated cells exhibited a typical cell cycle distribution with 30.8% in G1, 39.7% in S, and 23.3% in G2/M with both inhibitors producing subtle changes in the cycle distribution of G1 and S at 24 hours, with G2/M distribution remaining stable. 500 nM BIA increased G1 to 34.9% and reduced S to 36.4%, 1 μM BIA increased G1 to 32.1% and reduced S to 37.6%, 1 μM C91 increased G1 to 33.9 and reduced S to 36.4%, and 3 μM C91 resulted in a slight decrease of G1 to 29.9% and reduced S to 37.95% (**Fig. 3.6**). These modest fluctuations are consistent with the reported behavior of GSK-3 inhibitors on cell cycle progression, showing slightly delayed G1/S transition [143].

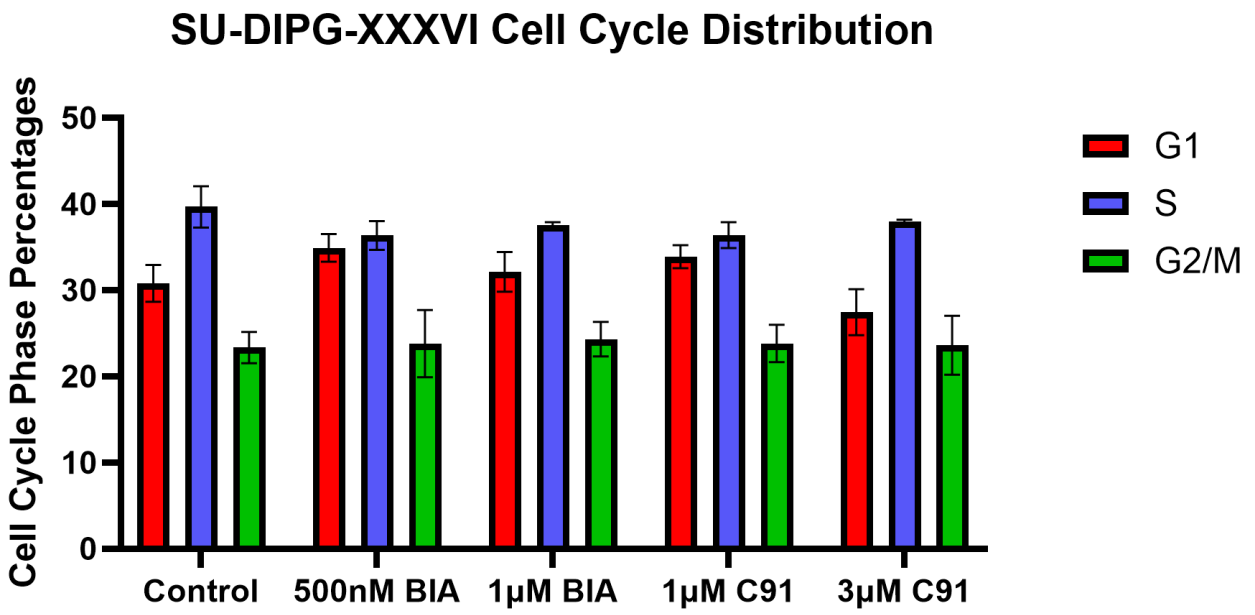

Figure 3.6: Cell cycle analysis using propidium iodide via flow cytometry. Cells were seeded at $3x10^4$ cells/well in a flat-bottom 6-well plate and allowed to adhere overnight. Cells were then treated with culture medium or BIA/C91 for 24 hours. Cell cycle phase distribution was determined using FlowJo V10 Watson modeling. Bar plot shows mean ± SEM of n=3 individual experiments performed.

3.2.7 Migration of DMG cells was inhibited after BIA and C91 treatment in 2D Wound-Healing and Transwell assays

A key driver of pHGG progression and recurrence is their ability to invade healthy brain tissue. Previous studies have shown that both small-molecule selective GSK-3 inhibitors and indirubin derivatives can effectively block migration in adult glioblastoma and pediatric high-grade glioma cell lines [83,92,106]. To confirm these effects of BIA and C91 on pHGG cell lines, I used two assays that measure migration. The scratch wound-healing assays assess collective cell migration patterns and wound closure, while the transwell evaluates individual endothelial cell invasion/migration through a membrane in response to a chemoattractant. With these experiments, I hoped to differentiate the effects of BIA and C91 on glioma migration patterns and assess whether they can sufficiently impair wound closure and overall migration. To conduct the scratch wound-healing assay, confluent

monolayers of all pediatric cell lines (SU-DIPG-36, SF8628, and KNS-42) were scratched with a sterile 1mm pipette tip and treated with either BIA, C91, or vehicle control in their appropriate culture medium. Plates were immediately transferred to the IncuCyte S3 live cell imaging system, and phase-contrast images of the wounds were acquired every hour for 24 hours at 4x magnification to capture the entire well (**Fig. 3.7A-C**). SU-DIPG-36s and SF8628s tested 2 concentrations of BIA and C91 to assess if there is a dose-dependent effect on migration, and the KNS-42s received single doses of both BIA and C91.

Both BIA and C91 significantly impaired wound closure in a dose-dependent manner in both the SU-DIPG-36s and SF8628s over 12 and 24h, respectively (**Fig. 3.7D-E**). Lower dose BIA/C91 (500nM BIA/1μM C91) reduced 12 hour wound closure in the SU-DIPG36s to 48.74 and 49.09%, (*p=0.0187 and *p=0.0212, respectively) and higher dose BIA/C91 (1 μM BIA/3 μM C91) reduced wound closure to 28.82 and 37.71% (vs vehicle 64.74%, ****p<0.0001 and ***p=0.0005, respectively). Interestingly, KNS-42s showed significant migration suppression with the higher BIA/C91 doses (7.46% and 7.32% vs 32.16% closure of vehicle, both **p=0.0026, **Fig. 3.7F**) despite their resistant phenotype observed in the proliferation and cytotoxicity assays shown above. These results could be due to their slower-growing nature, as evidenced by the baseline growth kinetics established in the proliferation time-course assay conducted above, and the treatment with BIA/C91 could compound that. Nonetheless, these results indicate that both inhibitors significantly impact the migratory ability of these cells. Two-way ANOVA revealed that both BIA and C91 possessed greater migration inhibition in the DMG cell lines compared to the KNS-42s. However, the observed robust anti-migratory response of the KNS-42s suggests that the effects of GSK-3 inhibition on migration/invasion are not directly correlated with proliferative arrest and may instead

reflect cytoskeletal reorganization or other factors modulated by the Wnt/β-catenin pathway [92].

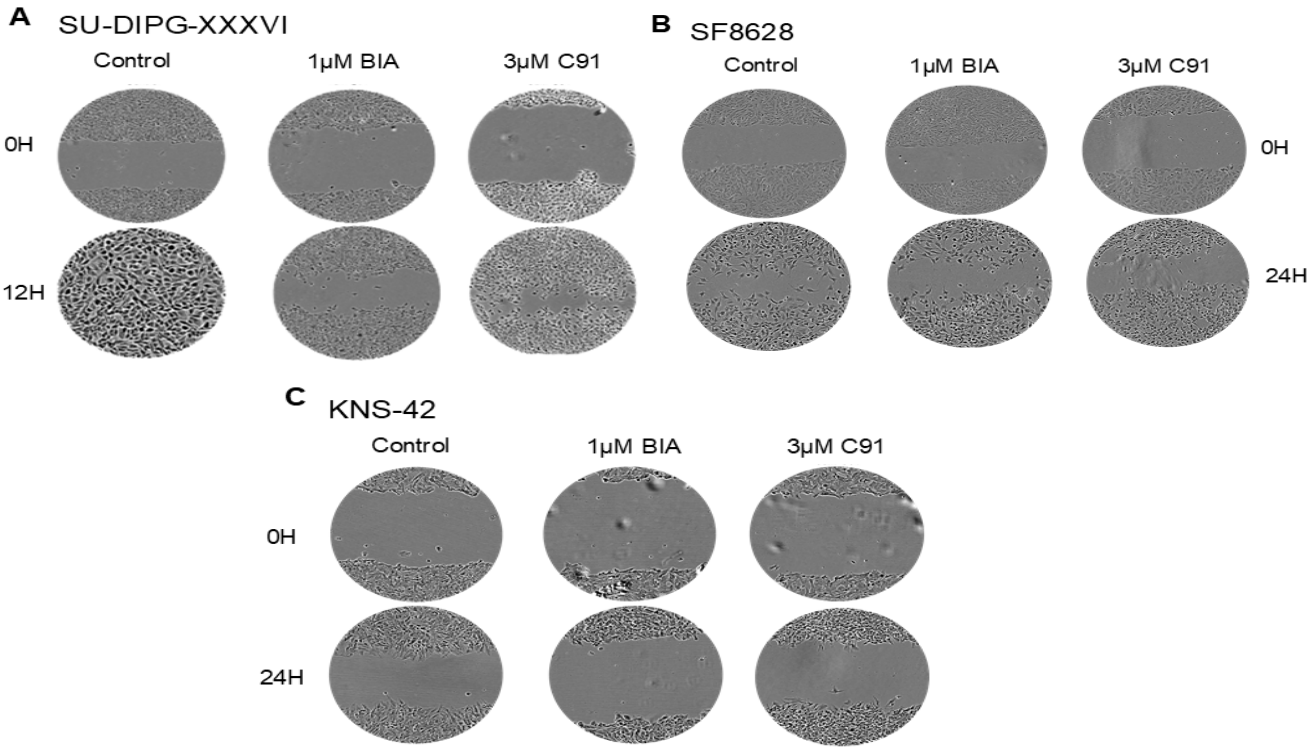

Figure 3.7: Wound-healing Scratch assay Images. 4x magnification, phase-contrast representative images of wounds at t_0 and the endpoint (12 or 24H) of **(A)** SU-DIPG-36, **(B)** SF8628, and **(C)** KNS-42. n=3 individual experiments performed with each condition in triplicate, with 3 length measurements per technical triplicate.

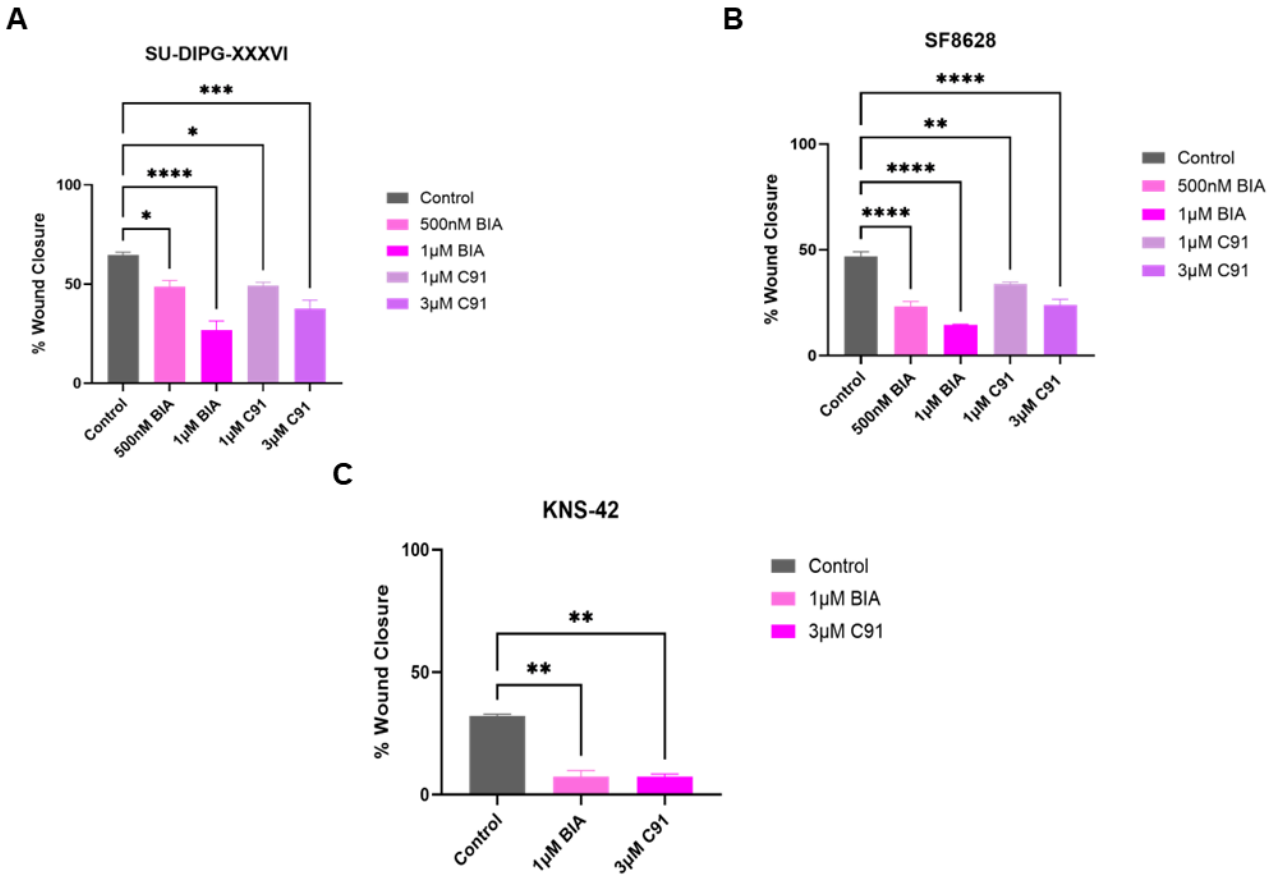

Figure 3.8: Wound-healing Scratch assay. Cells were seeded at $3x10^3$ cells/well **(A)** SU-DIPG-36, **(B)** SF8628, and **(C)** KNS-42 in a 6 or 24-well plate and allowed to adhere overnight. Confluent cell monolayers were scratched with a p200 pipette tip, and wound healing was captured using the IncuCyte S3 Live-Imaging System. % Wound closure was calculated as the length of the wound at t_n/t_0 *100. Bar plots show mean ± SEM of n=3 individual experiments performed with each condition in triplicate, with 3 length measurements per technical triplicate.

Complementary transwell assays were also conducted to validate these findings in a more physiologically relevant system by seeding DMG cell lines (SF8628, SU-DIPG-36) at 50,000 cells per transwell insert in media containing either BIA, C91, or the vehicle control. Media containing 10% FBS was placed in the well beneath the insert to serve as a chemoattractant, driving pediatric glioma cell migration through the membrane, and cells were left to migrate for 6 hours. Pediatric glioma cells that migrated to the basal side of the insert were fixed in ice-cold 70% methanol or ethanol and stained with DAPI. Membranes

were affixed to coverslips for imaging using the Olympus VS200 Slide Scanner, and migrated cells, as identified by nuclear stain, were counted using Image J. Image J analysis of the coverslip affixed membranes showed similar results to the scratch assay. Migrated cells were normalized to control conditions to measure the degree of migration relative to the control, with both BIA- and C91-treated cells exhibiting slower migration rates than the control (**Fig. 3.9A- B**). Remaining consistent with the scratch, BIA had a more potent effect than C91 in inhibiting migration in both glioma cell lines, suggesting that BIA's multi-kinase activity might offer a greater therapeutic advantage for pediatric glioma treatment. To determine whether there was any significant inhibition between the two cell lines, a two-way ANOVA was conducted. This analysis revealed a shared sensitivity across conditions between both the SF8628s and the SU-DIPG-36s, with neither cell line exhibiting enhanced sensitivity over the other.

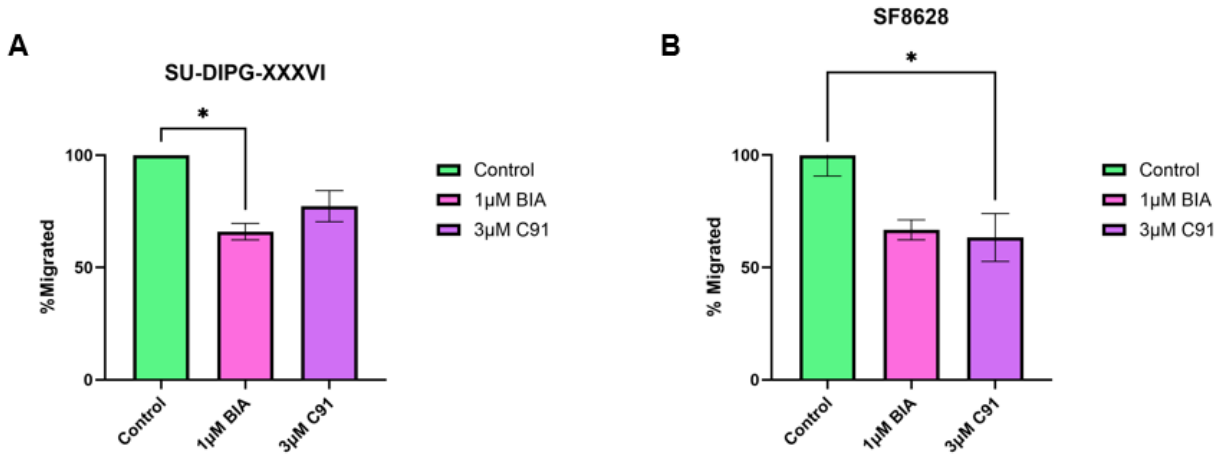

Figure 3.9: Transwell migration assay of DMG cell lines. Cells were seeded at $5x10^4$ cells/well SU-DIPG-36 **(A) and** SF8628 **(B)** in 24-well transwell inserts. Cells were treated with BIA or C91 (1 μM/3 μM, respectively). Migration was measured over 6 hours, and % migrated was calculated as the number of migrated cells normalized to the vehicle control (vehicle control = 100%). Graphs show mean ± SEM of n=2 individual experiments performed with each condition in triplicate.

3.3 Chapter 3 Summary and Discussion

pHGGs and DMGs are devastating pediatric brain tumors with a poor prognosis and less than 2% patient survival beyond 5 years, despite attempts to improve therapies over the past 3 decades [31,144]. These tumors exhibit high rates of recurrence due to their ability to diffusely infiltrate midline brain structures, as well as their high resistance to radiotherapy and chemotherapies [57]. Their aggressive phenotype warrants further identification and the development of novel therapeutic approaches to target their resistance mechanisms and halt their growth. In this chapter, a comprehensive phenotypic analysis of two GSK-3 inhibitors, BIA, a multi-kinase indirubin derivative, and C91, a selective GSK-3 inhibitor, was conducted to assess their ability to halt the progression of key cancer hallmarks across pediatric high-grade glioma cell lines.

Uncontrolled proliferation is a hallmark that promotes resistance and tumor recurrence in several cancer types. Gliomas, such as diffuse midline glioma, are characterized by their ability to rapidly proliferate, driven by epigenetic alterations (Ex: H3K27M mutation) and metabolic reprogramming. The motility and growth of pediatric high-grade glioma cells were examined using live-cell imaging, highlighting differences in growth rates associated with their individual mutations. The live-cell IncuCyte imaging demonstrated that both BIA and C91 act as potent suppressors of proliferation, as seen by a dose-dependent induction of cytostatic growth in the pediatric glioma cell lines. This was especially evident in the SU-DIPG-36 (H3.1K27M) cell line, where all tested concentrations of BIA kept confluence low, maintaining a plateau of 12-19% as early as 12 hours after treatment. Higher concentrations of BIA (5 μM-10 μM) in the SF8628s and KNS42s induced the same effects on growth, with induction of a growth plateau beginning at 24 and 36 hours post-treatment, respectively. This

was not observed in cells treated with the specific GSK-3 inhibitor C91, which exhibited an overall less potent effect on confluence across all three pediatric glioma cell lines. This was further illustrated by a shift in the timing of growth arrest diverging from the observed effect of BIA in these same cells, with the SU-DIPG-36 cells beginning at 24 hours post-treatment, the SF-8628 cells at 36 hours post-treatment, and the KNS-42 cells at 48 hours post-treatment. However, decreases in confluence were still observed in a dose-dependent manner across all lines, but were less severe overall compared to BIA treatment, which may indicate that BIA's broader multi-kinase activity could affect additional mechanisms of cellular growth and proliferation, enabling BIA to have more profound effects than the more specific activity of C91.

These effects extended to my cytotoxicity assays, in which 72-hour endpoint analysis using CellTiter-Glo confirmed that both inhibitors were, in fact, inducing true cytotoxicity, resulting in cell death rather than strict cytostasis. The H3K27M mutation-bearing DMG cell lines (SU-DIPG-36 and SF8628) exhibited a significantly higher sensitivity to BIA treatment compared to the KNS42s, indicating a mutation-specific vulnerability that could be advantageous in developing effective therapies for DMG. Notably, although both compounds were less potent against the KNS-42s overall than against the DMG lines, they had a more pronounced effect on viability in the KNS-42s, despite their strong proliferation resistance. The continued higher efficacy of BIA over C91 shows that its additional kinase activity contributes to its potency and is not strictly mediated by GSK-3 inhibition. Although treatment with C91 alone across DMG cell lines successfully inhibited proliferation and reduced cell viability, it cannot fully recapitulate the potent effects of BIA in these cell lines. This suggests that multi-kinase inhibition may be a more effective approach to reducing DMG resistance.

Also examined in this chapter were the effects of GSK-3 inhibition on cell cycle perturbations, as both inhibitors have known effects on cell cycle phase progression, as examined in prior studies [110,143]. PI cell-cycle analysis was performed in the most responsive cell line, SU-DIPG-36s, after 24 hours of treatment with either inhibitor or vehicle control. Slight fluctuations with the compound treatments were observed, consistent with the reported behavior of these inhibitors. There was no overall significant effect on phase distribution at this time point. This helped establish that any observed effects on migration and invasion were not due to cytotoxicity or cell-cycle dysregulation.

The anti-migratory and anti-invasive effects of both BIA and C91 on pediatric glioma cell lines appear to be selective mechanisms unrelated to any cytotoxic effects of these compounds. This has been established in prior studies in which they observed that the anti-migratory effects of the GSK-3 inhibitors tested, LiCl and BIO, were reversible following washout of the drug [83,106]. Potent anti-migratory effects in pediatric high-grade glioma cell lines were observed with both compounds in wound-healing scratch assays. This response was dose-dependent, with higher concentrations of both inhibitors having more potent effects on the collective migration of each cell line. This anti-migratory effect of these compounds also extended to the more resistant KNS-42s, suggesting that their effects are not mediated through proliferation or viability reduction and that these mechanisms inhibiting migration are specific. One speculative mechanism could be cytoskeletal reorganization or other factors modulated by activation of the WNT/β-catenin pathway, as GSK-3 inhibition can stabilize β-catenin, causing it to localize in the nucleus through canonical WNT signaling [92].

Complementary transwell assays further confirmed the anti-migratory effects of these inhibitors in DMG cell lines, both BIA- and C91-treated cells exhibiting slower migration rates than the control. Remaining consistent with the scratch, BIA had a more potent effect than C91 in inhibiting migration in both glioma cell lines, suggesting that BIA's multi-kinase activity and compensatory pathway modulation may offer a greater therapeutic advantage for pediatric glioma treatment. This could prove especially relevant for DMG as it is characterized by aberrant gene expression that leads to uncontrolled proliferation and its invasive phenotype, driving resistance and tumor recurrence [78-80].

To conclude, this chapter provided a comprehensive profiling of the effects of GSK-3 inhibition on tumor cell biology and behavior across several characteristic hallmarks such as proliferation, viability, cell cycle dysregulation, and migration/invasion. These results provide a compelling argument for further investigation into GSK-3-mediated effects on tumor cell biology and the potential of GSK-3 inhibitors as candidates that possess anti-proliferative and anti-migrative properties in diffuse midline glioma. Further investigation into these compounds and their effects is encouraged, as they offer an intriguing pathway to combat DMG resistance.

CHAPTER 4: ENDOTHELIAL CELL BEHAVIOR AND BBB PERMEABILITY

BBB/BTB model content adapted from Jimenez-Macias JL, Vaughn-Beaucaire P, Yan J, **Clark J**, Lawler SE. "Decoding the biology of the blood-brain tumor barrier in brain cancer." Accepted, Molecular Cancer Research (AACR), 2026, on which I contributed to figure generation and writing of the DMG/BTB background section.

4.1 Overview and Significance

One of the major barriers to improving the delivery of chemotherapeutic treatments in DMG is the BBB/BTB. In brain cancer, the BBB is influenced by cancer cell behavior programs and altered into what is known as the BTB. In some CNS tumors, BTB integrity is disrupted in certain areas, creating a heterogeneously permeable environment. In the case of DMG, the integrity of the BTB is not disrupted; in fact, in the pons and brainstem, the BTB is more unyielding, making delivery of chemotherapeutic agents even more difficult. This issue is further compounded by the tumor's ability to influence existing and develop new vessels that work to provide nutrients and oxygen for the tumor, otherwise known as angiogenesis, facilitating the migration of glioma cells [145,146]. A previous study in the Lawler lab investigated the effects of BIA on BBB permeability in hCMECs. In this study, BIA was observed to reduce the expression of CDH5 and ZO-1, tight junction markers associated with the brain endothelium, and to decrease the TEER in endothelial monolayers [93]. BIA was also observed to enhance *in vitro* GBM sensitivity to cisplatin (a commonly used chemotherapeutic agent), increase cisplatin accumulation in tumor tissue, and prolong survival in murine xenograft models [93]. These findings of enhanced permeability show great promise for expanding treatment options for gliomas, but it is unclear whether BIA's ability to modulate BBB permeability is due to its inhibition of GSK-3 or its other multi-kinase activity.

Therefore, in this chapter, I sought to determine whether GSK-3 inhibition could disrupt the intact BBB and the DMG-associated BTB by modulating endothelial cell behavior and the permeability of 3D BBB/BTB spheroids. Endothelial viability, collective motility, angiogenic tube formation, and barrier permeability were assessed to evaluate GSK-3's therapeutic potential in DMG. I hypothesized that GSK-3 inhibition could increase

permeability while reducing endothelial angiogenic and migrative capacity, thereby enhancing therapeutic delivery into the brain.

4.2 Results

4.2.1 Potency of BIA and C91 in endothelial cells

Prior RNA sequencing and tight junction protein profiling in our lab characterized BIA's effects on BBB integrity and revealed the downregulation of key junctional components, including CDH5 and ZO-1 [93]. In this study, we aimed to determine whether the effects of BIA on tight junction instability and BBB integrity were GSK-3-mediated through its inhibitory activity or through its other multi-kinase activity. To do this, BIA and C91 were compared in a series of functional assays that worked to assess their effects on BBB integrity, endothelial cell motility, and angiogenic inhibition. Initially, the viability of the endothelial cells in response to BIA or C91 treatment was examined to directly compare whether the drug concentrations used in the DMG tumor biology investigative assays were more tumor-specific or if they exhibited an equal toxic profile to brain endothelial cells.

To do this, brain endothelial cells (hCMEC/D3) were treated with BIA or C91 for 72 hours and viability was quantified via CellTiter-Glo as discussed in Chapter 3, Section 3.6 under the same conditions as the pHGG cell lines. The results were similar to those of Chapter 3, shown by two-way ANOVA in which there was a significant main effect of both the drug and cell line, with BIA exerting a stronger cytotoxic effect than C91 across the cell lines. Interestingly, the hCMECs exhibited a similar sensitivity to BIA as the SF8628s and the SU-DIPG-36s with an IC_{50} of 1.86 μM, whereas with C91 treatment, they portrayed a similar resistance as the KNS-42s with an IC50 of 5.92 μM, indicating a more robust resistance to

C91 treatment than the DMG cell lines (**Fig. 4.1A**). Additional Two-way ANOVA analysis comparing the drug specific IC_{50} values for the endothelial cells and the pHGG cell lines revealed significant differences, highlighting BIAs potency and confirming its stronger cytotoxic effects on the DMG cell lines, SU-DIPG-36 and SF8628, and the hCMECs compared to the KNS-42s (**p=0.0076, *p=0.0206, *p=0.0154, respectively). This analysis also revealed that C91 had a significantly more potent effect on the SU-DIPG-36s (H3.1K27M) compared to all other cell lines, with the most dramatic difference observed when compared with the KNS-42s (**Fig. 4.1B-D**; *p=0.0425). This observation could reflect a mutation-specific sensitivity that should be further explored. The hCMECs also showed a significant dose-response effect of viability reduction for both compounds, with BIA continuing to demonstrate a stronger effect as seen in the rest of the cell lines suggesting that although both compounds reduced the viability of the hCMECs BIA may offer an edge on reducing DMG tumor viability while C91 offers a more selective approach that at higher doses can reduce tumor cell viability without harm to endothelial cells.

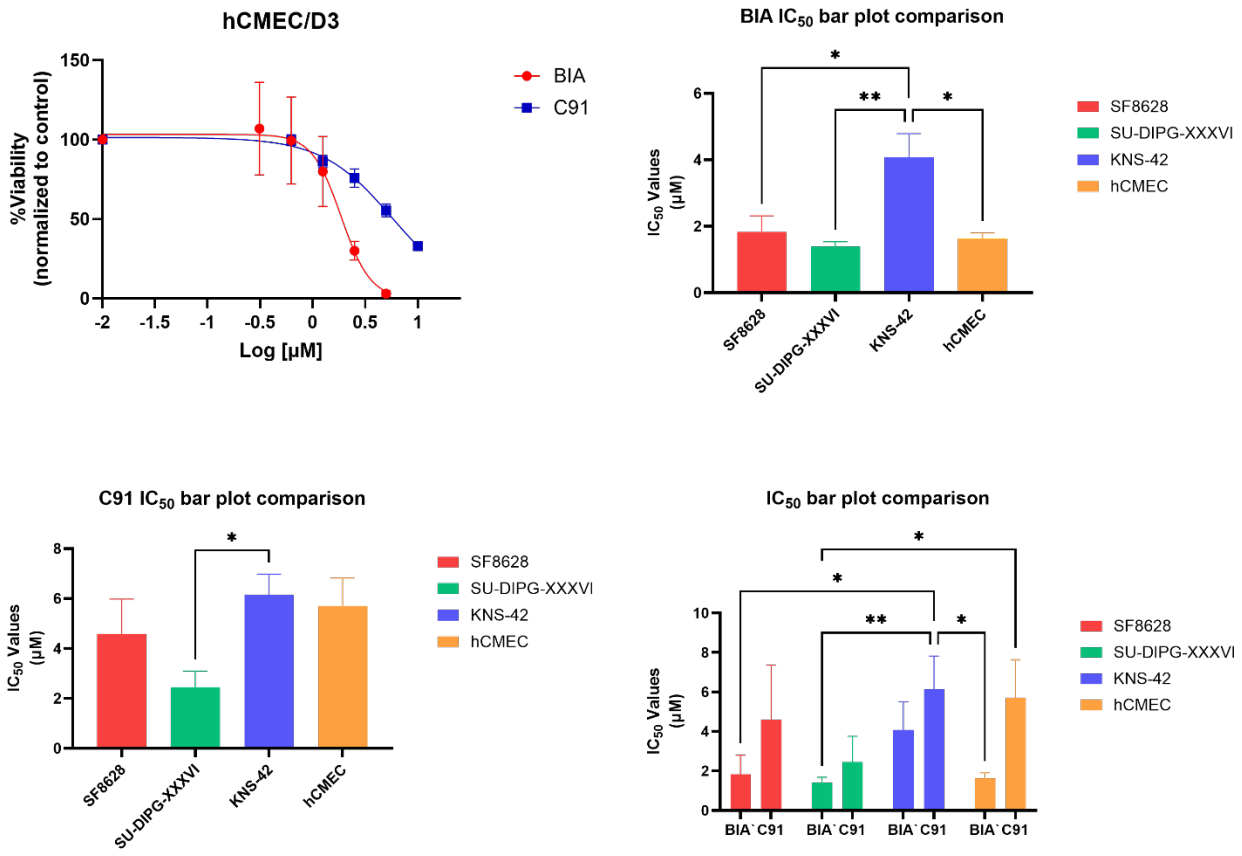

Figure 4.1: CTG viability IC_{50} curves for hCMECs with BIA and C91 compared to pHGG cell lines. (A) Dose-response curves from CellTiter-Glo endpoint assay (72h). **(B)** Comparison of IC_{50} values for BIA-treated cells among the hCMEC and pHGG cell lines. **(C)** Comparison of IC_{50} values for C91-treated cells among the hCMEC/D3 and pHGG cell lines. Nonlinear regression (log[inhibitor] vs response) yields IC_{50} values. **(D)** IC_{50} comparisons between hCMEC and pHGG cell lines. Mean ± SEM, n=3 triplicates.

4.2.2 BIA and C91 reduce endothelial motility

Endothelial invasion and motility are significant drivers of glioma progression and inevitable recurrence, and understanding their role is crucial for improving treatment options for DMG. To evaluate the impact of GSK-3 inhibition on endothelial cell motility, the scratch wound-healing and transwell assays were performed. The scratch wound-healing assays assess collective cell migration patterns and wound closure, while the transwell evaluates individual endothelial cell invasion/migration through a membrane in response to a chemoattractant. The transwell assay more closely mimics endothelial cell migration through

the brain's ECM. With these experiments, I hoped to differentiate how BIA and C91 influence endothelial cell behavior as it relates to their migrative capacity. To conduct the scratch wound-healing assay, confluent monolayers of hCMECs were scratched with a sterile 1mm pipette tip and treated with either BIA/C91 or vehicle control in endothelial cell culture medium. Plates were immediately transferred to the IncuCyte S3 live cell imaging system, and phase-contrast images of the wounds were acquired every hour for 24 hours at 4x magnification to capture the entire well. Interestingly, similar to the pHGG cell lines, wound healing in hCMECs was impaired over 12 hours, with % wound closure reaching only 33.21% with BIA treatment and 43.73% with C91 treatment, compared to the control at 69.16% (**Fig. 4.2A**). Using Two-way ANOVA, it was observed that both BIA and C91 significantly impaired hCMEC migration, despite C91's reduced sensitivity in hCMEC viability, similar to the KNS-42s. These robust anti-migratory results suggest that the impact of GSK-3 inhibition on migration/invasion impairment is independent of their effects on viability.

To further validate and complement these findings in a more physiologically relevant system, I conducted transwell assays with hCMECs (**Fig. 4.2B**). To do this, endothelial cells were seeded at 50,000 cells per transwell insert in media containing either BIA, C91 or the vehicle control. Media containing 10% FBS was placed in the well beneath the insert to act as a chemoattractant to drive endothelial migration through the membrane, and cells were left to migrate for 6 hours. Endothelial cells that migrated through to the basal side of the insert were fixed in ice-cold 70% methanol or ethanol and stained with a DAPI nuclear stain. Membranes were affixed to coverslips for imaging using the Olympus VS200 Slide Scanner, and migrated nuclei were counted using Fiji/Image J x86-64. Fiji/Image J x86-64 analysis of the coverslip affixed membranes showed results consistent with the scratch assay, with both

BIA and C91-treated cells exhibiting slower rates of migration than the control. These findings were further corroborated when compared to the pHGG cell lines using Two-way ANOVA, showing significant interactions of compound efficacy in inhibiting migration across all cell lines. Remaining consistent with all previous assays, BIA had a more potent effect than C91 in inhibiting migration in the hCMECs, suggesting that BIA's multi-kinase activity might offer a greater therapeutic advantage overall.

Further two-way ANOVA analysis comparing the compounds' effects in the hCMECs and pHGG cell lines revealed significant interactions in the efficacy of migration inhibition across all cell lines, with a stronger, more pronounced effect observed in the DMG cell lines. Despite the stronger effect on DMG cell lines, the observed reduction in endothelial cell migration has clinical promise, as this effect remains evident without reaching cytotoxic concentrations. This was further supported by the reduction in migration seen by the C91-treated cells despite their less potent effects on viability compared to BIA-treated cells. These findings support a targeted approach of reducing endothelial cell migration and motility without any cytotoxic effects. This is especially evident with C91 treatment, which exhibits a selective profile that preferentially targets tumor-associated pathways of migration/invasion without excessive endothelial cell toxicity. This approach is advantageous for developing a therapeutic strategy for diffuse midline glioma.

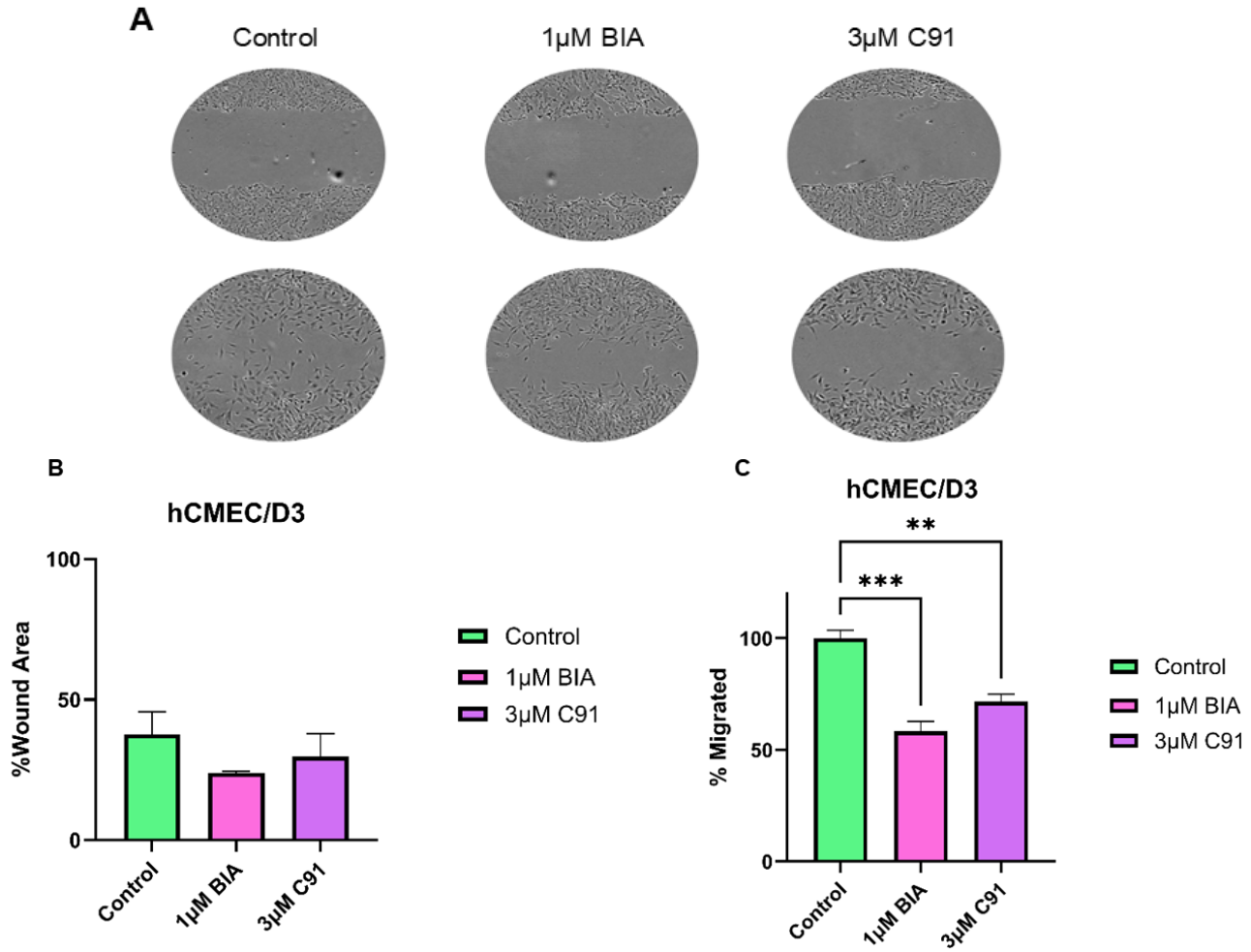

Figure 4.2: Scratch and Transwell migration assays on hCMEC/D3. (A) Representative images of wound healing at beginning and endpoint (12H). **(B)** Wound-healing scratch assay. % Wound closure was calculated as the length of the wound at t_n/t_0 *100. Bar plots show mean ± SEM of n=3 individual experiments performed with each condition in triplicate, with 3 length measurements per technical triplicate. **(C)** Transwell migration assay. Cells were seeded at $5x10^4$ cells/well in 24-well transwell inserts. Cells were treated with BIA or C91 (1μM/3μM, respectively). Migration was measured over 6 hours, and % migrated was calculated as the number of migrated cells normalized to the vehicle control (vehicle control = 100%). Graphs show mean ± SEM of n=2 individual experiments performed with each condition in triplicate.

4.2.3 BIA and C91 disrupt Endothelial Tube Formation

To directly assess the effects of GSK-3 inhibitors on endothelial network formation, a tube formation assay was conducted. This is directly relevant for cortical pHGG gliomas that exhibit higher expression of VEGF-A and PDFRα, resulting in abnormal vessel morphology and BBB disruption [65,69]. HBMECs were plated at a density of 15,000 cells per well in pre-equilibrated 96-well plates containing 50 µL of growth factor-reduced Matrigel. HBMECs were plated in 100 µL volumes containing either vehicle control, 50 ng/mL VEGF-A, 500nM BIA, 1 µM BIA, 1 µM C91, or 3 µM C91. HBMECs were immediately transferred to the IncuCyte S3 live-imaging analysis system to acquire hourly 4x magnification, phase-contrast images of each well over 24 hours. At 12 hours, differential impairment of tube formation was observed with BIA and C91, with VEGF-A-treated wells exhibiting extensive interconnected tubule networks and elongating, protruding branches characteristic of mature endothelial tubular structures (**Fig. 4.3**). Observed with both doses of BIA was a striking disruption of tube formation, with no observed branching or interconnected network assembly. At a low dose of C91 (1 µM), partial network disruption was observed, with reduced branching and less extensive network formation. Whereas higher-dose C91 (3 µM) resulted in near-complete disruption of tube formation, with extremely shortened branching and almost no interconnected tube networks observed. These results establish both BIA and C91 as potent anti-angiogenic agents that impair tube formation and could have a clinical impact for overcoming the hyper-vascularized BTB of cortical pHGGs.

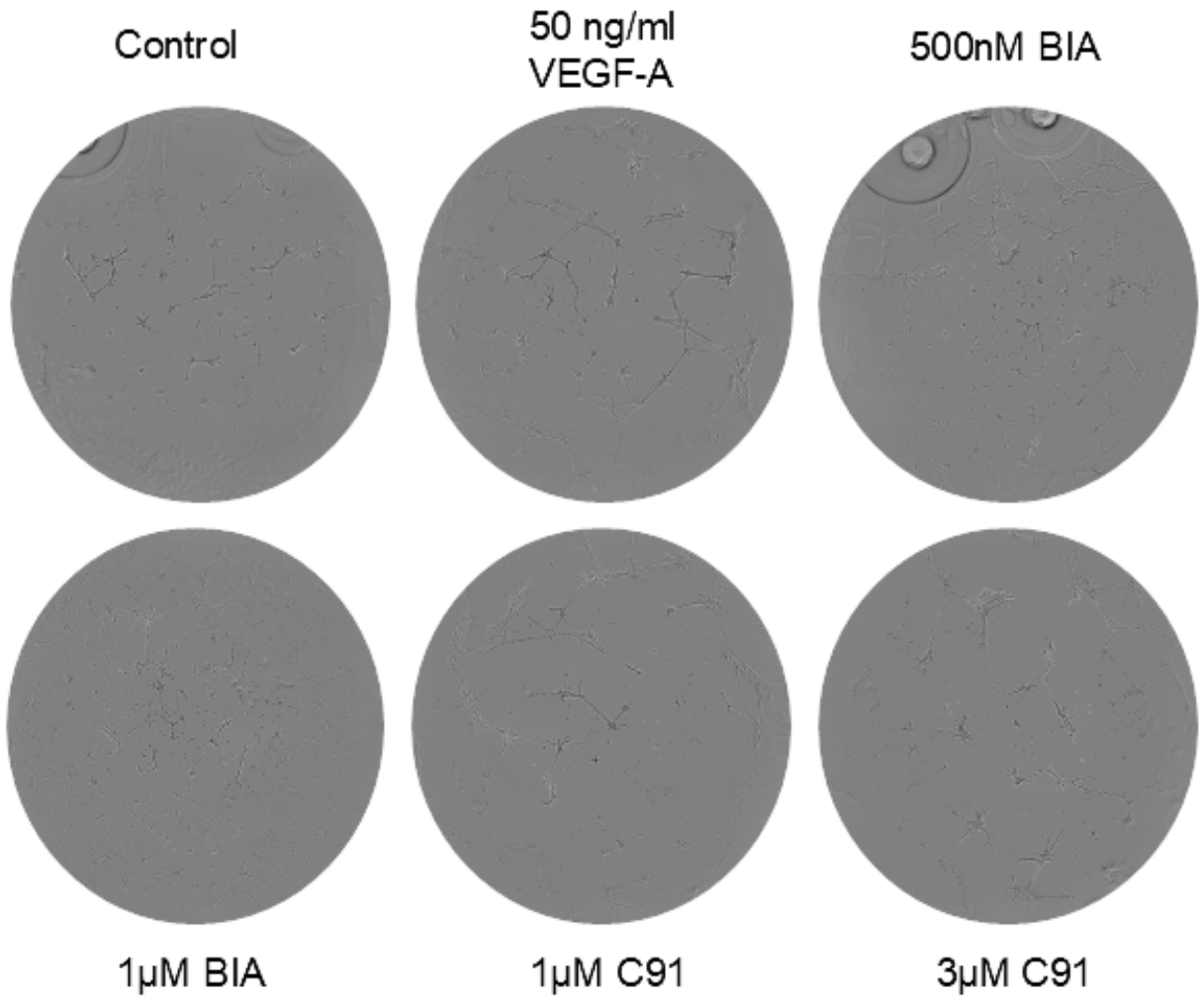

Figure 4.3: Tube Formation assay on HBMEC cells at 12 hours. Tube formation assay completed using growth factor-reduced Matrigel. Observed impaired tube formation with both BIA and C91 treatment over 12 hours compared to the VEGF-A positive control. All conditions were performed in triplicate.

4.2.3 BIA and C91 differentially modulate endothelial barrier integrity

Although endothelial motility and invasion are crucial aspects driving pHGG resistance mechanisms, the BBB/BTB continues to remain an impermeable barrier, limiting drug delivery and reducing the efficacy of chemotherapeutic treatments. The previously identified impact of BIA on tight junction formation and TEER by our lab laid the groundwork for our comparative study. To dissect whether BIA's previously established effects are mediated through GSK-3 inhibition, I first measured trans endothelial electrical resistance on

monolayer hCMEC/D3 cells in response to BIA and C91 treatment. Sub-IC_{50} doses of BIA and C91 were chosen to ensure any drops in resistance that were observed were not a result of any cytotoxic effects of the drugs. The resistance was recorded and plotted beginning with the resistance plateau and simultaneous time of drug addition (**Fig. 4.4**). Treatment with both compounds caused a gradual decline in barrier integrity of hCMEC/D3 cells, shown by their reduction in trans endothelial electrical resistance, indicating a modulation of barrier integrity over time with sustained treatment.

We also assessed whether these effects would persist post-drug washout and observed immediate differences in resistance in cells treated with both BIA and C91. Once the drug was removed and cells were replaced with fresh media, the C91-treated monolayers maintained a TEER reduction similar to that observed during treatment, whereas BIA-treated monolayers continued to decrease TEER, indicating that these compounds differentially modulate barrier permeability. The extended effect of BIA's reduction in resistance suggests that BIA might have more long-term effects on endothelial barrier stability. This is also evidenced by the previously reported RNA sequencing that the lab conducted on BIA-treated hCMECs, showing a downregulation in key junctional proteins such as CDH5 and ZO-1. Altogether, these findings suggest that GSK-3 inhibition can compromise brain endothelial barrier integrity over time, potentially creating a more drug-permeable environment, although the kinetics of the two drugs appear to differ. Further exploration of these differential modulatory effects on 3D barrier permeability became the next step in elucidating these differences on BBB/BTB permeability.

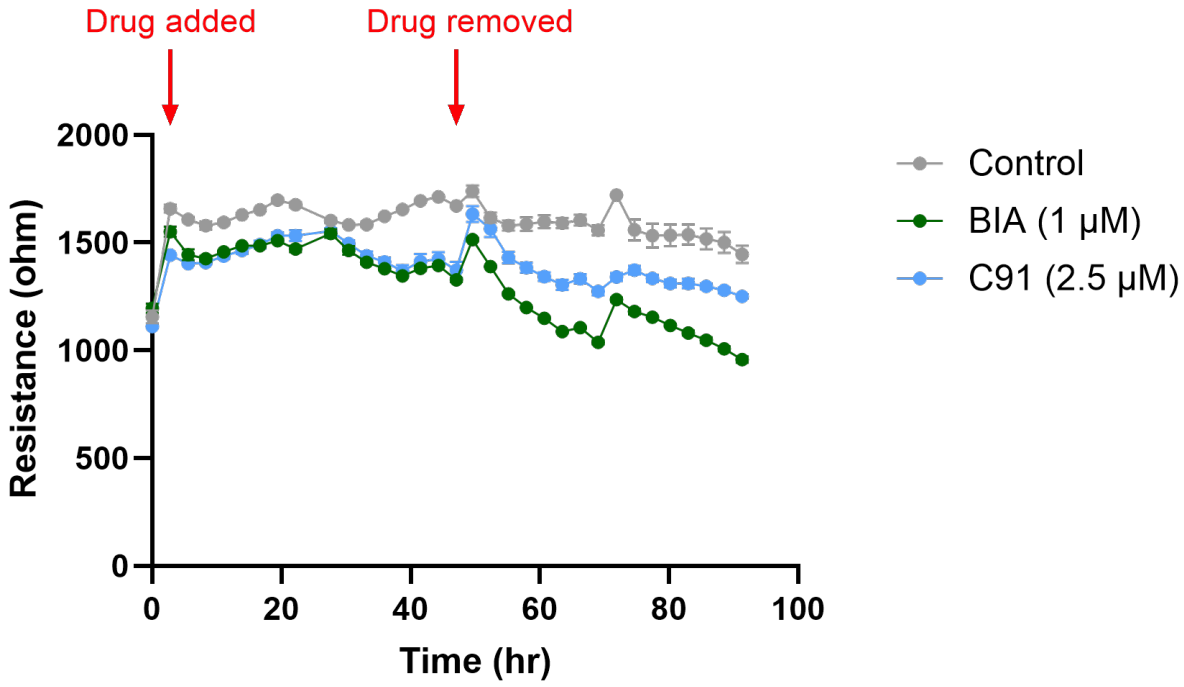

Figure 4.4: Barrier function assay on monolayer hCMEC/D3 cells using ECIS. Representative ECIS (n=3 independent experiments) traces showing trans endothelial electrical resistance of vehicle-control, BIA, and C91 treated endothelial monolayers. BIA and C91 treated monolayers both showed reduced TEER compared to the control. Following drug washout, BIA-treated monolayers showed a progressive decline in resistance, whereas C91-treated monolayers maintained a stable TEER reduction.

4.3 Experimental models of the BTB

4.3.1 In vitro models

The continuous recreation of the BBB is widely achieved using 2D *in vitro* cell cultures of perivascular cells, such as transwell-grown multicellular BBB platforms that reproduce BBB breakdown and molecular permeability effects upon perturbant exposure. Furthermore, these models reveal the importance of the immune microenvironment in establishing the vascular niche status in brain tumors. For instance, a breast brain-metastasis BTB *in vitro* transwell model, comprising human brain endothelial cells on the luminal side of the chamber and pericytes, astrocytes, and/or 231-BR cells on the abluminal side, showed increased

doxorubicin penetration and diminished TEER [147]. This BTB permeability disruption was caused by astrocytic S1P3-CCL2/IL6, which in turn diminished endothelial barrier properties. IL6 secretion by tumor cells can induce an immunosuppressive environment that promotes tumor growth, confirming the relationship between the BTB, immune microenvironment remodeling, and tumor progression [148].

Induced pluripotent stem cells (iPSCs) iPSCs serve as powerful tools to generate brain endothelial cells or other fundamental members of the neurovascular unit, recapitulating human disease. Studies have examined iPSC-derived human brain microvascular endothelial cells (iBMECs) cultured in microvessels of a polydimethylsiloxane (PDMS) chip [149]. These endothelial cells surround the microvessels and exhibit tight junctions and efflux pump activity. The addition of the breast cancer cell line JIMT-1-BR revealed kinetics of tumor integration within BBB microvessels and generated a BTB model that recapitulated vascular integrity disruption in brain metastases. Bulk RNA-seq revealed marked upregulation of pro-inflammatory and cholesterol-metabolism genes. This model was also effective for antibody penetration quantification and study of myeloid-BTB integration, by addition of a differentiated monocytic cell line to the model, which induced secretion of IL-8, IL-1β, and TNF-α pro-inflammatory cytokines typically elevated in patients [149].

Microfluidic devices enable the establishment of BBB-like flow systems to study compound penetration properties across the BBB [150]. Astrocyte cells and/or brain tumor cells can be grown in the inner sections of the chamber, while brain endothelial cells in the outer compartments. The outer and inner sections are separated by a porous wall that permits the exchange of compounds and nutrients between the endothelial outer wall and the

astrocyte/tumor regions. This enables flow and stationary assays to assess different approaches to compound delivery across the BTB, such as ultrasound-mediated, cavitation-enhanced drug delivery, as well as CAR-T cell extravasation and anti-cancer cytotoxic capacity in a GBM/BTB context [150,151]. These models could be further developed and analyzed by examining transcriptional heterogeneity in tumor cells during flow assays at different rates, providing insight into how blood flow can impact tumor cell behavior.

Three-dimensional BBB models, such as BBB spheroids, consist of astrocytes, pericytes, and brain endothelial cells grown under ultra-low attachment conditions. These spheroids present higher TJ and efflux pump expression than 2D models, and are responsive to the addition of VEGF-A, showing increased permeability of fluorescent dextran [152]. Engraftment of patient-derived GBM cell lines in these BBB spheroids promoted stemness and mesenchymal transcriptional signatures in the tumor cells above neurospheres, mimicking what has been seen *in vivo* and in the clinic [152]. These BTB spheroid models could be leveraged to understand tumor aggressiveness in the presence of the perivascular niche, as well as cell-cell interactions between the BTB and the tumoral compartments.

4.3.2 In vivo pre-clinical models

Studying the BBB *in vivo* is crucial for understanding its role in health and disease and for developing strategies to deliver therapeutic agents to the brain. Several murine GBM cell lines have been engrafted in syngeneic mice to study GBM across various contexts, including its immune and vascular microenvironments [153]. Patient-derived xenograft (PDX), syngeneic, and genetically engineered (GEE) murine models remain the gold standard for drug delivery and BBB permeability studies, given their utility for testing multiple routes of administration

and conducting pharmacokinetic and pharmacodynamic analyses. However, the application of murine models is not limited to drug delivery. Mouse models have been used to understand the interaction between tumor cells and the vasculature, and how this communication impacts tumor migration and progression [154].

Non-human primate (NHP) models are more similar to humans in BBB structure and function, making them valuable for translational research and preclinical testing of therapeutic agents. However, NHP models of GBM are not widely used, mainly due to ethical considerations given their similarity to humans. NHPs can help model brain tumorigenesis by utilizing whole-brain radiation therapy (5-day treatment for 2 days at 350 cGy) to induce GBM [155]. This is instrumental for studying the early stages of brain tumor development and could also inform the initial interactions between neoplasms and their vascular and immune microenvironment, a process that remains fundamental to disease progression [155].

Zebrafish are gaining popularity as an experimental model for BBB research due to their transparent bodies and easy genetic manipulation, making them suitable for high-throughput imaging screening. Transgenic zebrafish models with vascular reporters have shown the functional relevance of the WNT pathway in vascular-tumor interactions, and inhibition of this pathway decreases migration and interaction of glioma cells with the vasculature [156]. This model is effective at highlighting vascular co-option phenotypes in tumor cells and could be further leveraged to assess changes in cellular-state heterogeneity and therapeutic responses during interactions with the vascular niche, using live imaging with fluorescent reporters.

Canine models are typically employed in BBB studies due to their size and the ability to perform advanced imaging and surgical techniques, making them particularly useful for studying brain tumors and evaluating BBB disruption techniques. Moreover, extracellular vesicles (EVs) derived from canine GBM can be used as therapeutic delivery vehicles, given their stability and *in vivo* BBB-penetrating properties [157]. In a similar manner, porcine models are advantageous due to the brain size and anatomy similarity to humans, making them suitable for studying BBB physiology. Pigs are used in neuroimaging experiments, such as focused ultrasound BBB disruption studies [157]. Induction of spinal gliomas in mini pigs yields neoplasms with rich immune and vascular microenvironments, rendering this model useful for further studies of the BBB and BTB in GBM. Given the greater similarity between the porcine and human brains, further studies of the perivascular TME and its effects on brain tumor progression and survival are warranted.

4.3.3 Clinical-based data and modeling

Biopsies and other specimens obtained directly from patients in the clinic remain fundamental and rich sources of data for dissecting different biological layers of brain tumors. This is primarily generated through high-throughput molecular profiling, including RNA sequencing, whole-genome sequencing, proteomics, and multimodal imaging, among other methods. Several datasets are publicly available to researchers worldwide; for instance, the Ivy Glioblastoma Atlas Project provides access to bulk RNA-seq data from specific anatomical GBM sections obtained by laser microdissection [93]. This resource permits interrogation of gene expression at the cellular tumor, pseudopalisades, infiltrating tumor, the leading edge, and microvascular proliferation, a site of intense angiogenic vasculature expansion.

Several teams are now leveraging these resources and applying various analytical methods to dissect the vascular microenvironment of gliomas. For example, a 2019 study from Dusart et al. used bulk RNA-seq data from the Cancer Genome Atlas (TCGA), the Genotype-Tissue Expression (GTEx), and the Accelerating Medicines Partnership-Alzheimer's disease consortium (AMP-AD) for identifying endothelial markers of the brain [155]. This approach identified brain endothelial markers that were selectively present in the vasculature of low- and high-grade gliomas, including CD34, CLEC14A, and VWF. They further identified vascular function genes present in GBM, including *CDH5* (VE-cadherin), *ESAM (*endothelial cell-selective adhesion molecule), *TIE1* (tyrosine kinase with Immunoglobulin/EGF-like domains 1), *ENG* (Endoglin), *ERG* (ETS Transcription factor ERG), *ACE* Angiotensin I Converting Enzyme), *PLXDC1* (Plexin Domain Containing 1), *and PCDH12* (Protocadherin 12) [155]. Further histological analysis confirmed the presence *of ACE, CD93, and ANGPT2* (Angiopoietin 2) in the GBM vasculature but not in the healthy brain, highlighting these genes as relevant biological features of the brain tumor-associated vasculature [155].

Single-cell transcriptomics represents an instrumental tool for identifying perivascular features with potential clinical implications. scRNAseq analysis from primary-recurrent GBM paired clinical samples showed that tumor-associated pericytes, abundant in microvascular proliferation regions, express high gene expression levels of extracellular remodeling matrix genes, mainly *COL1A1* (Collagen Type I Alpha 1 Chain) [158]. This was confirmed by its staining co-localization with PDGFR-β+. These findings are consistent with GBM patients at recurrence who present with high ECM remodeling signatures having shorter overall survival

and progression-free survival than patients with low ECM signature enrichment.

Recently, a comprehensive single-cell and spatial transcriptomic atlas of the vasculature of the brain has been generated, comparing healthy states of fetal brain, adult brain, and its pathological states, vascular malformations, and high-grade gliomas [159]. Immunofluorescence staining confirmed endothelial expression and vascular localization. Their findings showed that brain diseases, including malignancies, reactivate fetal/ developmental programs in the brain endothelium, increasing permeability and promoting disease progression. Notably, the human fetal brain and pathologies such as brain tumors express higher levels of the barrier permeability modulators *PLVAP* (Plasmalemma Vesicle-Associated Protein) and *ESM1* (Endothelial Cell-Specific Molecule 1) than the healthy adult brain. Targeting endothelial transcriptional programs in the BTB endothelium induces permeability modulation and enhanced drug delivery [93]. Interestingly, increased expression of MHC class II molecules was observed across pathologies but not in the healthy brain, supporting the importance of the vasculature in modulating immune infiltration and its activity in CNS diseases. A graphical summary of the models discussed in this section is shown in **Fig. 4.5**.

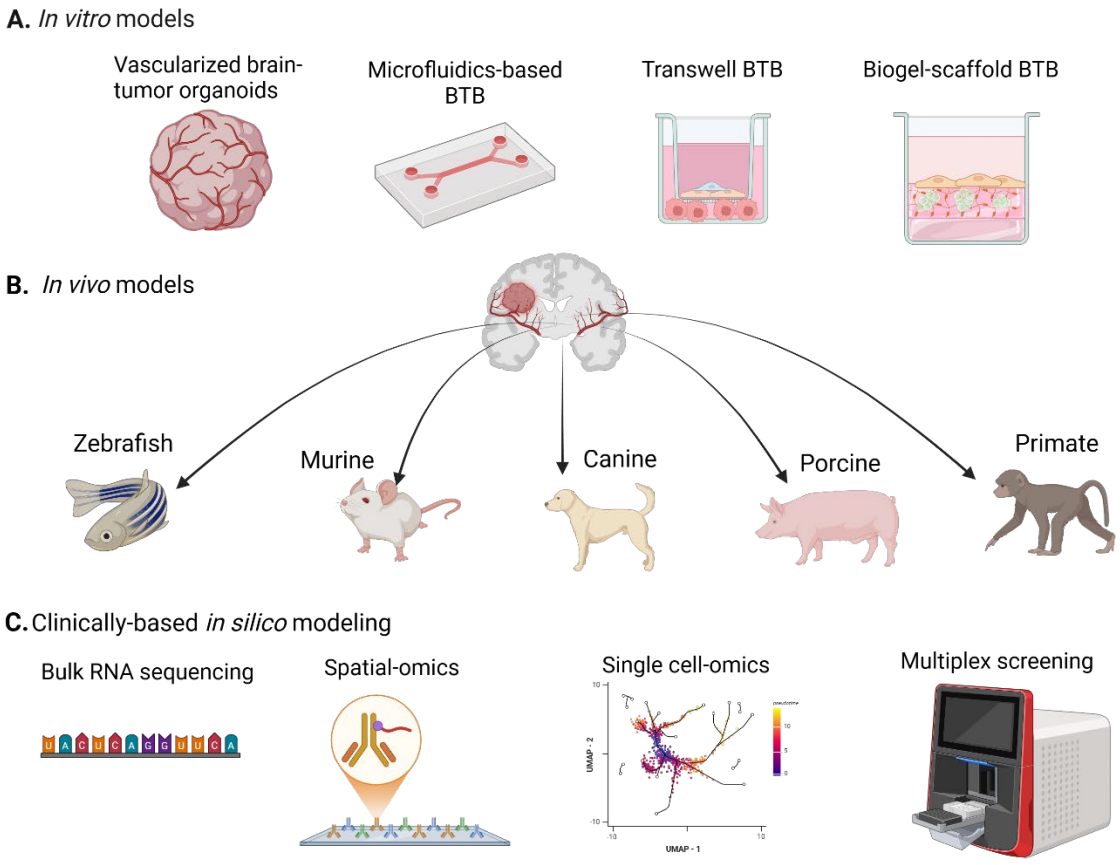

Figure 4.5: Experimental models of the BTB. To elucidate the cellular and molecular characteristics of the BTB, researchers are using a wide range of preclinical and clinically based modeling systems. **(A)** *In vitro* systems have enabled the mechanistic interrogation of tumor-endothelial cell interactions and effects of therapeutics on BTB permeability and tumor-vessel co-option. **(B)** *In vivo* models, including large animals, have elucidated vascular formation and association with brain tumors, mainly for testing drug therapy efficacy and capacity to reach the brain. **(C)** Clinical-based *in silico* modeling has offered multi-omic characterization of the molecular and cellular composition of vascular-tumoral niches. This modality has enabled the identification of how the vasculature alters tumoral cell organization and cell state, demonstrating its effectiveness in revealing the role of the perivascular niche in brain tumor state and progression [132]. Created in https://BioRender.com.

4.4 3D BBB/BTB co-culture models

4.4.1 BBB/BTB 3D spheroid model generation

Although endothelial cells serve as the primary physical barrier of the BBB, and characterizing their response to GSK-3 inhibition is important for ultimately improving drug delivery, astrocytes and pericytes also serve as critical components to barrier integrity and

overall BBB permeability. Astrocytes and pericytes regulate endothelial cell behavior, driving the formation of the tight, impermeable BBB, and understanding their interactions is crucial to properly developing therapeutic treatments that can overcome this barrier. To better understand these complex interactions and the impact of the structural makeup on permeability, 3D BBB co-culture spheroids containing (hCMEC/D3), human primary astrocytes, and pericytes were developed **(Fig. 4.6A)**. These 3D BBB co-culture spheroid models were developed in accordance with a previous model established in Cho et al. (2017), in which they characterized the development and structure of how the co-culture formed. They observed that the endothelial cells lined the outer surface of the spheroid, pericytes formed direct contact with the endothelial cells, and the astrocytes were found mostly in the core of the spheroid [160]. They also confirmed the high expression of several tight junction proteins, such as ZO-1, CDH5, and occludin, on the surface of the spheroids, indicating tight barrier formation, which is essential for controlling transport into the spheroid [160]. In this study, BBB spheroids were developed by culturing endothelial cells, astrocytes, and pericytes in equal ratios of 1,000 cells per well (3,000 cells total per well) in a customized BBB media (BBB media recipe described in chapter 2) in low-adherent round-bottom 96-well plates and allowed to self-assemble over 48-72 hours.

To utilize these 3D barrier models to assess permeability fluctuations due to GSK-3 inhibition, dextran uptake (FITC-dextran, 70 kDa) and antibody uptake (AlexaFluor-488 IgG antibody) were used. Dextran uptake was used to measure paracellular permeability and tight junction disruption, whereas antibody uptake served as a measure of receptor-mediated transcytosis and intracellular uptake/transport. The 3D nature of this model allows for a closer recapitulation of the *in vivo* microenvironment where complex interactions between these

different cell types facilitate the tight barrier formation, limiting the penetration of different molecules. This is especially important for studying the effects of GSK-3 inhibition on BBB integrity and penetration, to better understand how these interactions may affect their efficacy. It's also important to understand how these cells interact with tumor cells to capture the complexity of the BBB and how these multicellular interactions affect barrier permeability and drug uptake. To develop our BTB model, the DMG cell line SF8628 was seeded into low-adherence plates at 300-500 cells per well and allowed to form a spheroid over 24 hours. This was followed by the addition of our BBB co-culture system (hCMEC/D3, astrocytes, and pericytes, each at 1,000 cells per well), and allowed to form a new BTB co-culture system over an additional 48 hours **(Fig. 4.6B)**. Several ratios of DMG cells to endothelial cells, astrocytes, and pericytes were tested in order to determine the optimal co-culture conditions. This allowed us to draw direct comparisons on GSK-3 mediated integrity disruptions of both the BBB and BTB and blood-tumor barriers through treatments with BIA and C91 over 24 hours.

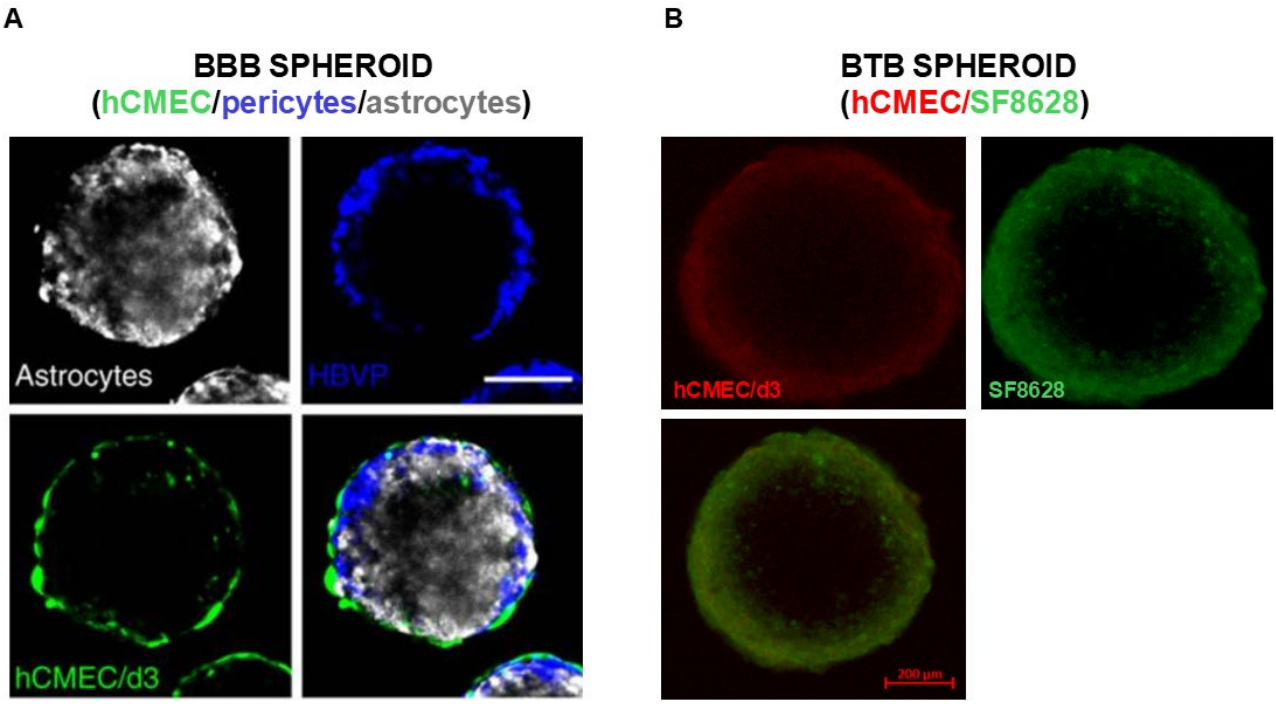

Figure 4.6: BBB/BTB Spheroid Cell Organization. **(A)** Representative confocal images taken from Cho et al. (2017) showing the organization of human astrocytes (white), HBVP (blue), and immortalized human cerebral microvascular ECs (hCMEC/D3; green) when co-cultured to form the BBB spheroid [148]. Astrocytes were pre-labeled with VivoTrack 680 Fluorescent Imaging Agent, HBVP with CellTracker Violet, HBMEC with CellTracker Orange, and hCMEC/D3 with CellTracker Green for 1 h before co-culturing on 1% agarose for 48 h. **(B)** Representative confocal images showing the organization of human astrocytes, HBVP, immortalized human cerebral microvascular ECs (hCMEC/D3; red), and SF8628 (H3.3K27M) when co-cultured to form the BTB spheroid. All spheroids were imaged using confocal microscopy.

4.4.2 Differential uptake observed by BIA and C91 treatment in BBB/BTB spheroids

To determine the effect of GSK-3-mediated permeability in 3D BBB co-culture models, I quantified uptake of 70 kDa FITC-dextran and an AlexaFluor488-IgG antibody as measures of paracellular flux and transcytosis, respectively. Two doses of both BIA (500 nM, 1 µM) and C91 (1 µM, 3 µM) were tested to determine whether the effects of GSK-3-mediated permeability were dose-dependent **(Fig. 4.7A-B)**. To assess the effects of BIA and C91 on paracellular permeability, after 24 hours of spheroid treatment with either drug or vehicle, fresh media containing a 1:1000 dilution of 70kDa FITC-dextran was added to the spheroids

and incubated for 4 hours at 37 °C prior to fixation with 10% formalin. Quantification of mean fluorescence intensity (n=5 spheroids per group) showed a significant dose-dependent increase in dextran uptake was observed with BIA treatment, with 500 nM BIA showing a fold change of 5.78 ± 1.38 and 1 μM BIA showing a fold change of 10.16 ± 2.54 vs the vehicle. C91 did not show the same effect as BIA, with 1 μM C91 showing a fold change of 0.852 ± 0.18 and 3 μM C91 a fold change of 1 ± 0.13 compared to vehicle. This dramatic difference in dextran uptake suggests that BIA's modulation of paracellular permeability is not GSK-3-mediated and may reflect additional kinase activity, although the exact mechanism still needs to be elucidated.

As an additional measure of barrier permeability, an AlexaFluor-488 IgG antibody was used to determine GSK-3-mediated effects on transcytosis. Similar to dextran uptake, after 24 hours of treatment with either drug or vehicle, a 1:500 dilution of the AlexaFluor-488 IgG antibody was added to the spheroids, and they were incubated for an additional 24 hours at 37 °C prior to fixation with 10% formalin. Again, quantification of mean fluorescence intensity showed BIA having a significant dose-dependent increase in AlexaFluor-488 IgG uptake, with 500 nM showing a fold change of 9.99 ± 5.10 and 1 μM BIA showing a fold change of 22.31 ± 13.36 vs the vehicle. Interestingly, C91 also showed a significant increase in antibody uptake, with 3 μM C91 showing a fold change of 8.42 ± 4.73. Although not statistically significant, there was also an observed increase in uptake with 1 μM C91, with a fold change of 4.97 ± 2.88 compared to vehicle. BIA's barrier modulation, occurring both paracellularly as previously reported due to tight junction breakdown and via endothelial vesicle transport, and C91's greater selectivity for endothelial vesicle transport without dextran leakage, highlight their differential modulation of barrier permeability [93].

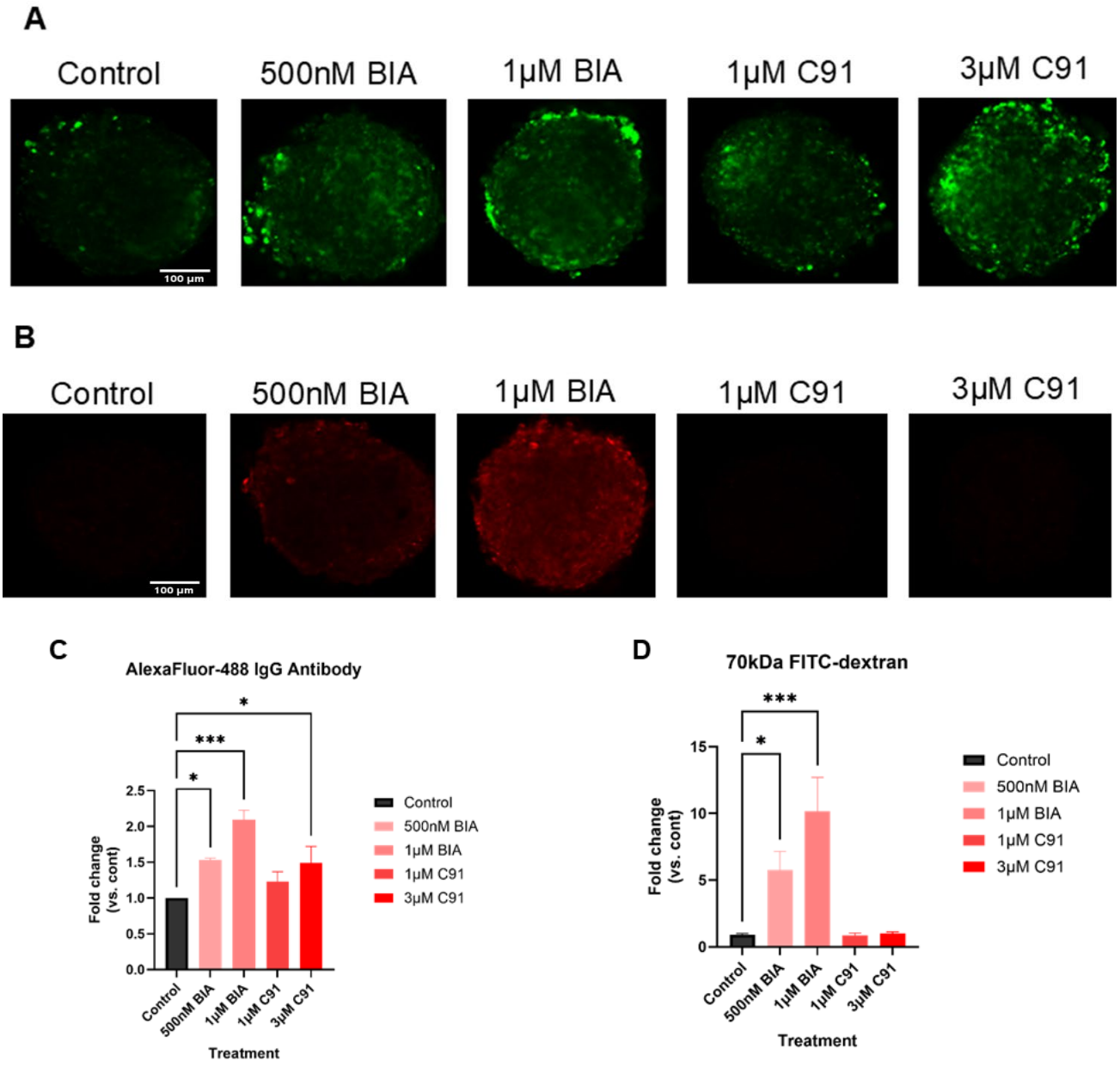

Figure 4.7: FITC-conjugated dextran (70kDa) and AlexaFluor-488 IgG permeability assay in BBB spheroids. (A) Confocal microscopy imaging of BBB spheroids with AlexFluor-488 IgG antibody uptake. **(B)** Confocal microscopy imaging of BBB spheroids with 70 kDa dextran uptake. **(C)** Bar plot of AlexaFluor-488 IgG antibody uptake showed a significant dose-dependent increase compared to control with both doses of BIA (500nM and 1 μM) and the higher dose of C91 (3 μM) (*p=0.0183, ***p=0.0002, *p=0.0289, respectively). **(D)** Bar plot of Dextran uptake showed a significant dose-dependent increase compared to control with treatments of 500nM BIA and 1 μM BIA (*p=0.0293, ***p=0.0003, respectively). n=3 independent experiments, n=5 spheroids per condition.

To assess whether these effects were still present with DMG cells interacting with the BBB, I investigated them in BTB spheroids **(Fig. 4.8A-B)**. 70 kDa FITC-dextran and AlexaFluor-488 IgG antibody uptake assays were conducted in the same fashion as the BBB spheroids, with 24-hour treatment of either BIA, C91, or vehicle, and then either a 4-hour incubation for dextran uptake or a 24-hour incubation for antibody uptake. After dextran or antibody uptake, cells were fixed in 10% formalin, and uptake was measured using an $n \geq 4$ spheroids per condition. 1 μM BIA treatment significantly increased the uptake of both FITC-dextran and IgG antibody (Dextran fold change 21.50, ***p=0.0004 and IgG fold change 1.85 ± 0.17, *p= 0.0291), similar to the BBB spheroid uptake results. Although increased IgG uptake was observed with both 500nM BIA and 3 μM C91, the results were not statistically significant (fold changes of 1.30 ± 0.04 and 1.37 ± 0.25, respectively). These results support the growing evidence that BIA is the more potent modulator of both BBB and BTB permeability, with consistent IgG antibody uptake across both models. The results of C91 on the BTB spheroids were similar to those seen in the BBB spheroids, with IgG antibody uptake increasing with no preliminary observed increase in dextran uptake. (3 μM C91 fold change 1.82). These results support the notion that BIA disrupts the integrity of both the BBB and BTBin a non-specific manner, targeting tight junction formation whilst utilizing intracellular transport to enhance uptake, whereas C91 has a more selective mechanism via GSK-3 inhibition that may be more suitable for drug delivery without inducing long-term barrier disruption.

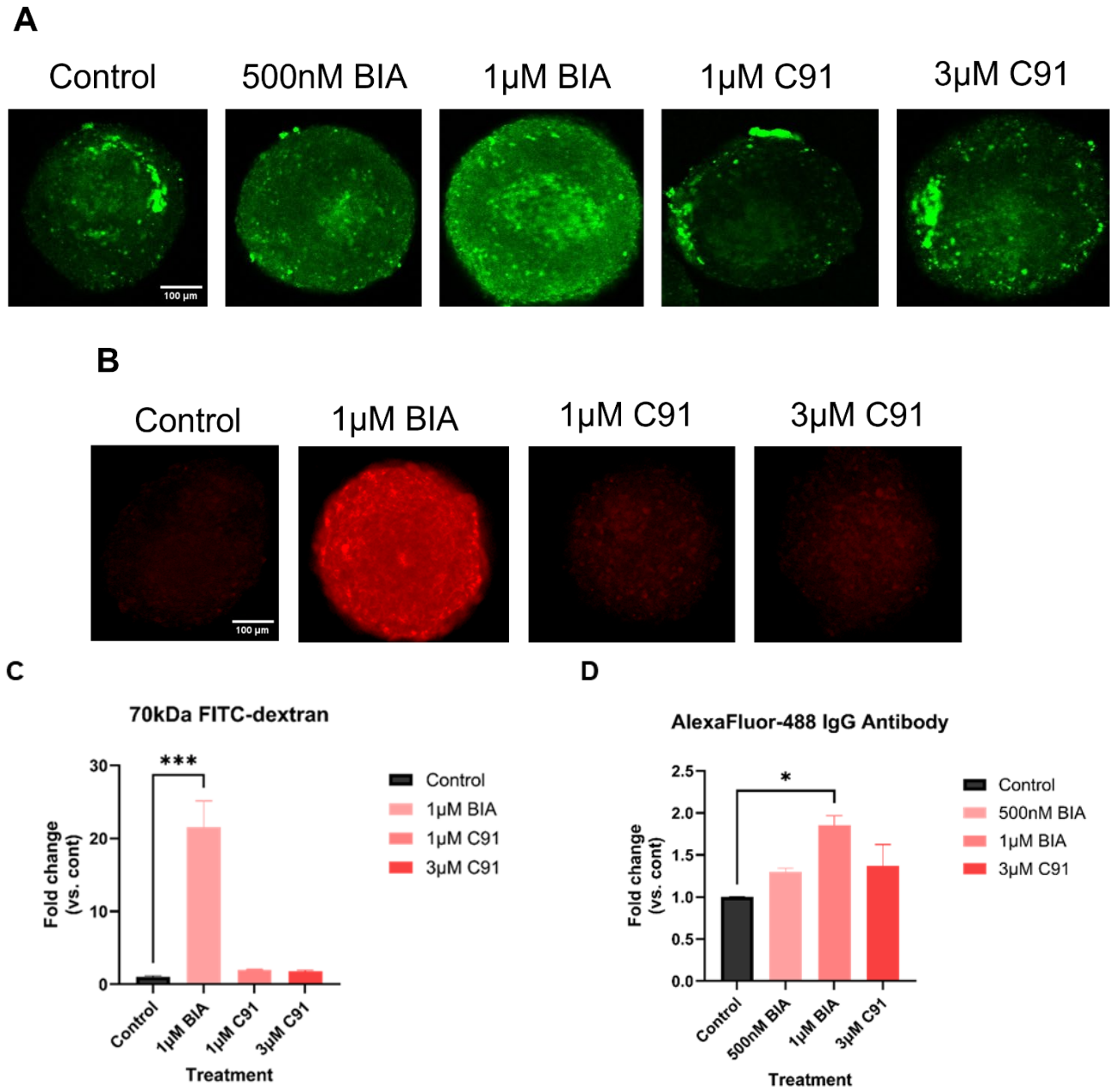

Figure 4.8: FITC-conjugated dextran (70kDa) and AlexaFluor-488 IgG permeability assay in BTB spheroids. (A) Confocal microscopy imaging of BTB spheroids with AlexFluor-488 IgG antibody uptake. **(B)** Confocal microscopy imaging of BTB spheroids with 70 kDa dextran uptake. **(C)** Bar plot of dextran uptake showed a significant increase compared to control with treatment of 1 μM BIA (***p=0.0003). **(D)** Bar plot of AlexaFluor-488 IgG antibody uptake showed a significant increase compared to control with 1 μM BIA (*p=0.0289). n=2 independent experiments, n=5 spheroids per condition.

4.5 Chapter 4 Summary and Discussion

The purpose of this chapter was to highlight the role of GSK-3 inhibition as a therapeutic agent in modulating BBB function and to illustrate the depth of its role in mediating the effects of BIA on reducing endothelial cell viability and motility, while increasing permeability. These results demonstrated that, while both compounds exhibited differential effects on endothelial cell behavior, BIA consistently showed greater potency across all assays, including viability, migration, and permeability. These results work to highlight how, although GSK-3 inhibition is an effective method for modulating barrier function and influencing endothelial migratory behavior, BIA's multi-kinase activity offers an edge and provides a deeper understanding of how GSK-3 inhibition can be used to modulate BBB/BTB function for DMG therapy.

Using CTG cell viability assays on hCMECs, I observed differences in BIA and C91 treatments over 72 hours compared with the pHGG cell lines. These differences showed that BIA elicited similar cytotoxicity profiles on both hCMECs and DMG cell lines. This suggests that BIA's multi-kinase activity can target both endothelial and DMG cell populations. In contrast, C91 had higher IC_{50}s and was less potent against endothelial cell populations than against DMG cell populations. The hCMEC monolayer TEER assay demonstrated that there is an inverse relationship between permeability and resistance following the treatment with BIA and C91. BIA and C91 decreased TEER, indicating their ability to increase permeability. BIA was shown to have a greater effect than C91, suggesting that BIA's mechanism is not solely through GSK-3 inhibition but may also involve other mechanisms. Following drug removal, TEER reduction remained stable in the C91-treated monolayers, whereas the BIA-treated monolayers continued to decrease in resistance, suggesting long-term effects.

In 3D BBB spheroids, BIA treatment showed dose-dependent increases in both paracellular permeability (dextran uptake) and transcytotic flux (antibody uptake). Treatment with 500 nM BIA showed 5.78 ± 1.38-fold and 9.992 ± 5.099-fold increases in dextran and antibody uptake, respectively. Treatment with 1 μM BIA showed a greater fold increase than 500 nM BIA for dextran uptake (10.16 ± 2.54) and antibody uptake (22.31 ± 13.36). In contrast, C91 was shown to have selective effects on antibody uptake, with 3 μM C91 increasing antibody uptake by 8.417 ± 4.73-fold without any dextran leakage, and 1 μM C91 increasing antibody uptake by 4.97 ± 2.88-fold. Although this was not statistically significant, it suggests a trend towards increased intracellular uptake. This suggests that BIA has broad effects on both tight junctions and receptor-mediated vesicular transport, whereas C91 specifically modulates the transcytosis process without affecting tight junction integrity.

Both drugs were shown to affect endothelial cell motility and migration in scratch and transwell assays at sub-IC_{50} concentrations, indicating that BIA and C91 are potential therapeutic agents for the treatment of DMG. Tube formation assays further revealed that BIA visually disrupted endothelial network formation at both low and high doses, and that C91 exhibited a dose-dependent effect, with the higher dose causing tubule disruption and the lower dose only partial disruption. This suggests that GSK-3 inhibition can modulate both the barrier and tumor cell invasion. In the DMG paradigm, where the BBB/BTB acts as a significant barrier to drug delivery, these data show that both BIA and C91 have the potential to enhance drug delivery into the tumor microenvironment without inducing significant endothelial toxicity. The multi-kinase activity of BIA may be useful for disrupting tight junction formation at the BBB/BTB to facilitate rapid drug delivery, whereas the more selective activity of C91 on transcytosis may be useful for enhancing long-term drug delivery without impairing

the barrier. Overall, these data show that GSK-3 inhibition by both BIA and C91 can modulate BBB/BTB integrity and endothelial cell behavior, with BIA showing broad-spectrum activity and C91 exerting a more selective effect on transcytosis. This suggests that these two compounds could be used strategically alongside other DMG therapies to enhance drug delivery and efficacy while minimizing adverse effects on the BBB.

CHAPTER 5: DRUG SCREENING AND MECHANISTIC STUDIES

5.1 Overview and Significance

DMGs are highly resistant to standard therapies due to their effects on the BTB, intrinsic resistance mechanisms, and rapid ability to invade critical brain structures. These tumors exhibit a high degree of genomic instability and aberrant dysregulation of key signaling and developmental pathways, contributing to their resistance and adaptability and driving their progression. Additionally, the impermeability of the BTB severely limits chemotherapeutic treatment options, leaving radiotherapy as the only standard of care. Due to their highly adaptive nature, radiotherapy only extends progression-free survival by approximately 6 months, with most patients succumbing to the disease within a year.

The previous chapters established that single-agent GSK-3 inhibition can suppress tumor cell proliferation and migration in DMG cell lines. They also established that GSK-3 inhibition modulates BBB permeability and inhibits endothelial motility and migration, thereby targeting critical processes in DMG progression and enabling two distinct approaches to BBB targeting and regulation of endothelial behavior. However, monotherapies can be limited by glioma cells' ability to develop resistance and drive recurrence, emphasizing the importance of identifying potential combination therapies to maximize clinical impact. Previous studies by our lab have shown that BIA can synergize with DNA-damaging chemotherapy to enhance toxicity and, in combination with cisplatin, promote DNA damage in adult glioma cell lines, prompting our investigation of this potential combinatorial efficacy in DMG cell lines [93]. Extended survival of mouse xenografts was also observed with those treated with BIA and cisplatin, with a significant accumulation of cisplatin in the tumor tissue. These results suggest that combining BIA with other chemotherapeutic agents may sensitize DMG cells and increase the permeability of drugs that otherwise cannot cross the BBB. Therefore, I

tested whether GSK-3 inhibitors can enhance the efficacy of chemotherapeutic treatments in pHGG models. This was done through extensive screening of FDA-approved agents, including some currently under early-stage clinical investigation for the treatment of DMG, such as gemcitabine (a DNA synthesis inhibitor) and vorinostat (a histone deacetylase inhibitor). This chapter helps to characterize the combination potential of GSK-3 inhibitors in DMG.

5.2 Results

5.2.1 Drug Screen

To translate the effects of GSK-3-mediated barrier modulation and pHGG anti-tumor effects into more clinically impactful findings, a high-throughput drug screen of 176 NIH FDA-approved therapeutics was conducted in SU-DIPG-36 and KNS-42s +/- BIA. Cells were seeded in 96-well, black-walled, clear-bottomed TC plates at a density of 1,500 cells per well and incubated overnight at 37°C with 5% CO_2 to allow for adherence. Post-adherence, cells were treated with 1 μM BIA and the NIH FDA-approved drug library at 1 μM concentrations for 72 and 96 hours **(Fig. 5.1)**. The cytotoxic efficacy of these combinations against pHGG cell lines was assessed using the luminescent ATP-based CellTiter-Glo assay, and the top hits were plotted using GraphPad Prism v10.6.1.

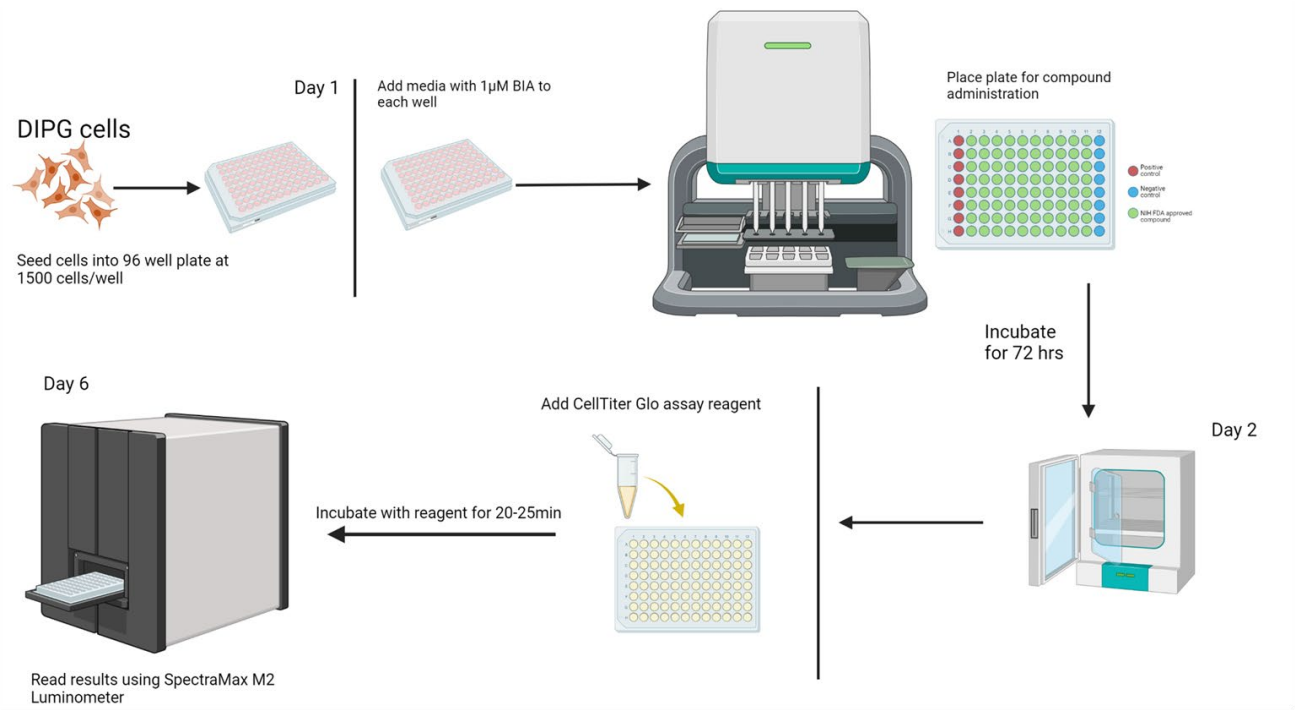

Figure 5.1: Schematic of High-throughput drug screening of the FDA-approved drug library in combination with 1 μM BIA. Made in Biorender.

This screening revealed several potential combinations in which BIA dramatically enhanced chemosensitivity across pHGG cell lines **(Fig. 5.2A-D)**, supporting prior data indicating that BIA enhanced the sensitivity of GBM cells to cisplatin. Top hits spanned different classes of chemotherapeutics, showing BIA's capacity to sensitize cells to several types of therapeutic agents. Overall, the SU-DIPG-36s showed higher sensitivity across combinations at both time points compared to the KNS-42s, which exhibited continued resistance, with only slight reductions in viability at both time points. Two interesting compounds identified in this screen that, in combination with BIA, showed enhanced cytotoxicity were Vorinostat and Gemcitabine. Gemcitabine and Vorinostat stood out as hits in both the SU-DIPG-36s and the KNS-42s, showing promise as a therapeutic combination across pHGG subtypes. These hits were further validated in follow-up experiments across a wider range of concentrations.

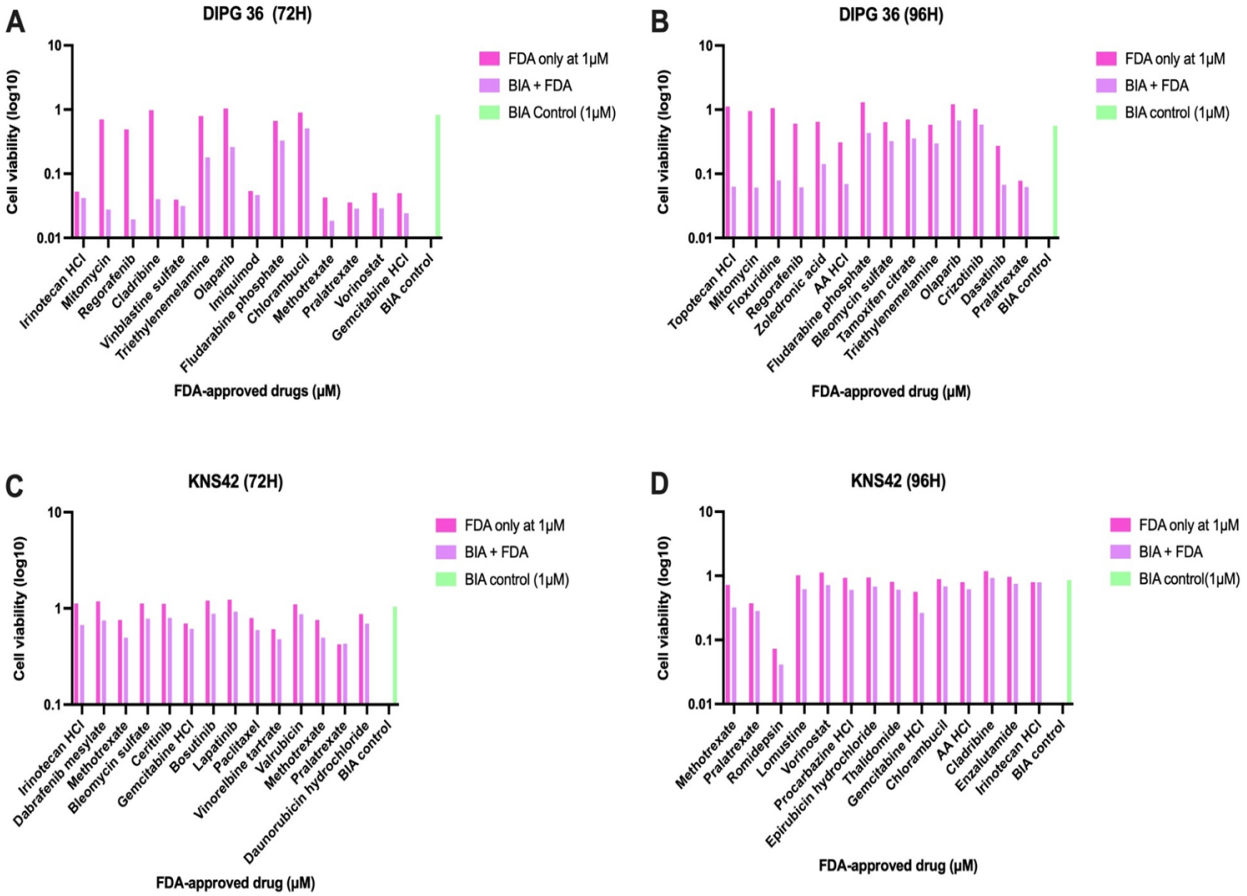

Figure 5.2: High-throughput drug screening of 176 FDA-approved chemotherapeutics in combination with 1 μM BIA. (A-B) Top 14 hits from the drug screen, presented as change in viability +/- 1 μM BIA in SU-DIPG-36 cell line over 72 and 96 hours (n=1). **(C-D)** Top 14 hits from the drug screen, presented as change in viability +/- 1 μM BIA in KNS-42 cell line over 72 and 96 hours (n=1).

5.2.2 Vorinostat Biology and combination with the GSK-3 inhibitor BIA

Vorinostat (suberoylanilide hydroxamic acid/SAHA), a histone deacetylase inhibitor (HDACi), was first given FDA approval for the treatment of T-cell lymphoma and has been investigated and widely used in the treatment of many other solid tumors [161,162]. Vorinostat alters chromatin structure by promoting histone acetylation and the activity of various transcription factors, ultimately manipulating gene expression. This alteration promotes upregulation of proapoptotic genes and downregulation of antiapoptotic genes, thereby inhibiting proliferation and promoting cell death [163,164]. In glioma, Vorinostat was found to increase p21 levels and induce G2-phase cell-cycle arrest and apoptosis through transcriptional downregulation of cyclin B1 [165]. Modulation of GSK-3 can potentiate some of these effects, as its inhibition induces G2/M-phase cell-cycle arrest and apoptosis in various cancers, including those of the CNS [166]. Prior studies have demonstrated strong synergy between GSK-3 inhibitors and Vorinostat in myeloma cells, prompting investigation in glioma[167]. Further validation of the combination seen in the drug screen of BIA and Vorinostat in SU-DIPG-36s yielded potent cytotoxic enhancement over a 96-hour treatment period (**Fig. 5.3A).** Vorinostat alone yielded an IC_{50} of 1.84 μM, whereas in combination with 1 μM BIA, the IC_{50} dropped to 0.24 μM, indicating a significant increase in DMG sensitivity to Vorinostat when in combination with BIA. This effect did not extend to the KNS-42s, with no observed enhancement of Vorinostat toxicity with the addition of 1 μM BIA in these cells (**Fig. 5.3B**).

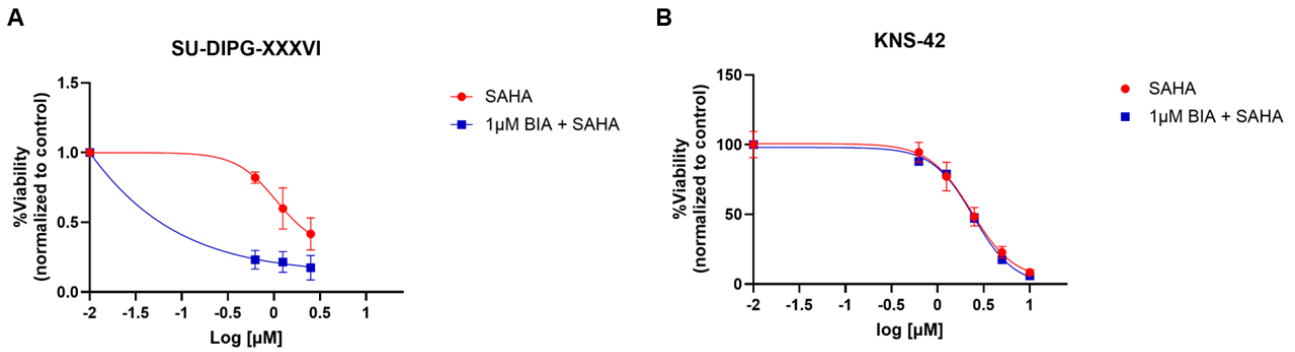

Figure 5.3: CTG viability IC_{50} curves for pHGG cell lines with BIA in combination with Vorinostat (SAHA). Dose-response curves from CellTiter-Glo endpoint assay (72h) in **(A)** SU-DIPG-36 and **(B)** KNS-42. Nonlinear regression (inhibitor vs response) for IC_{50} calculations. Mean ± SEM, n=3 triplicates.

5.2.3 Gemcitabine Biology and combination with the GSK-3 inhibitor BIA

Gemcitabine, a nucleoside analog, is a highly potent anticancer agent currently approved for the treatment of various solid tumors. Gemcitabine inhibits cellular DNA synthesis by incorporating into DNA and terminating DNA strand elongation, causing DNA fragmentation, and ultimately leading to cell death via apoptosis [168,169]. This apoptotic cell death is mediated through an increase in DNA cleavage, seen through activation of caspase-3 [170]. In glioma, gemcitabine can induce a bystander effect, in which its toxicity can diffuse and transfer between cells [171]. Carpinelli et al. (2006) investigated the effect of gemcitabine on cell-cycle phase distribution in C6 rat malignant glioma models and found that it induces S-phase accumulation and elicits apoptotic effects [172]. Gemcitabine has also been shown to be a potent radiosensitizer, particularly in a murine GBM model, where, in combination with radiotherapy, it improved survival compared to radiotherapy alone [173].

Despite these findings, clinical trials investigating gemcitabine pre-treatment before radiotherapy showed that this combination was not an effective treatment strategy for GBM [169]. This lack of translational impact in the clinic could be due to its hydrophilic nature, which

prevents adequate penetration of the BBB. Combining it with other small-molecule drugs, such as GSK-3 inhibitors that can successfully cross the BBB, may increase its clinical impact. Fixed-concentration designs of BIA (500 nM) and C91 (1 μM) were tested across a gemcitabine dose range tailored to each specific cell line (SU-DIPG-36: 5 nM-0.13 nM; SF8628: 100nM-6.25nM). Further validation of the combination of BIA/C91 and Gemcitabine revealed cell line-specific potency, in which the SU-DIPG-36s combination of 500 nM BIA and 1 μM C91 yielded dramatic shifts in IC_{50} compared to monotherapy, along with a dramatically more effective monotherapy baseline compared to the other pHGG cell lines (**Fig. 5.4A**). SF8628s yielded pronounced but submaximal sensitization with 72-hour treatment (**Fig. 5.4B**). Although an IC_{50} could not be generated within the tested concentrations (6.25-100 nM), the combination of Gemcitabine with 500 nM BIA produced an evident potency shift, indicating increased sensitivity to Gemcitabine in the DMG cell lines. The same trend of increased chemosensitivity of DMG cells to Gemcitabine treatment was observed when combined with 1 μM C91, with the highest concentrations of both BIA and C91 achieving a >55% reduction in viability.

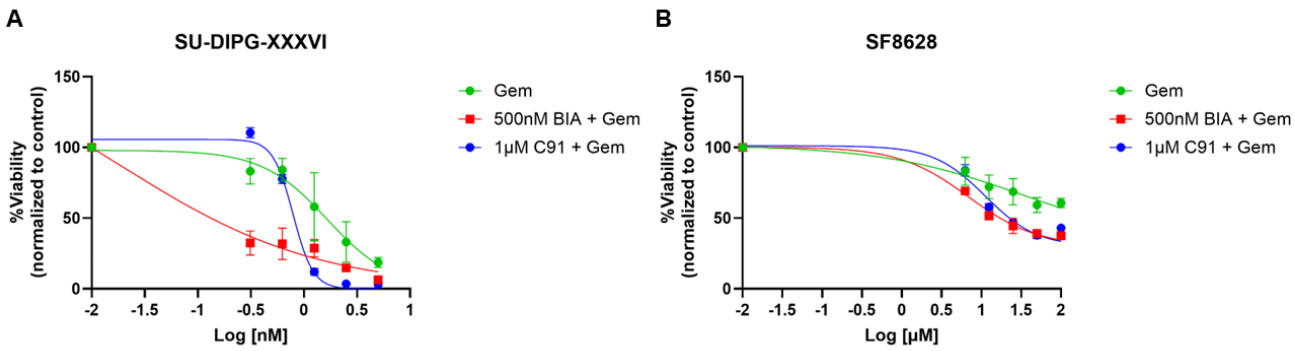

Figure 5.4: CTG viability IC_{50} curves for pHGG cell lines with BIA in combination with Gemcitabine. Dose-response curves from CellTiter-Glo endpoint assay (72h) in **(A) SU-DIPG-36** and **(B)** SF8628. Nonlinear regression (inhibitor vs response) for IC_{50} calculations. Mean ± SEM, n=3 triplicates.

5.2.3 Mechanistic Studies: WNT/β-Catenin Signaling

To elucidate certain mechanisms associated with GSK-3 inhibition in pHGG, the WNT/β-catenin signaling pathway was investigated using the DMG cell lines, SF8628 and SU-DIPG-36. Immunofluorescence staining of DMG monolayers treated with BIA and C91 for 24 hours revealed visual observation of enhanced β-catenin signal intensity in both SF8628 (**Fig. 5.5A**) and SU-DIPG-36s (**Fig. 5.5B**). Control cells showed baseline β-catenin distribution, and co-staining with phalloidin showed thick, organized stress fibers. Treatment with both BIA and C91 resulted in global β-catenin signal amplification, showing both nuclear and diffuse cytoplasmic accumulation, confirming the GSK-3 inhibition mechanism associated with β-catenin stabilization in DMG cell lines. Phalloidin staining of BIA and C91 treated cells demonstrated overall thinning of F-actin, disrupted filament structure, and cell rounding in both treatments relative to the controls, which could contribute to the migration inhibition observed in Chapter 3. This was further validated through Western blotting, in which there was a confirmed upregulation in total β-catenin expression in both the SF8628 (**Fig. 5.6A**) and the SU-DIPG-36s (**Fig. 5.6B**). Total GSK3-β remained stable across the suggestions, consistent with pharmacological inhibition blocking functional expression without reducing GSK-3β protein levels.

Another method used to confirm functional WNT/β-catenin transcriptional signaling was the TCF/LEF Top Flash assay. This assay measures the luminescent signal driven by β-catenin accumulation. When GSK-3 is active, it targets β-catenin for ubiquitination and subsequent degradation. When GSK-3 is inhibited, β-catenin does not get degraded, and it begins to accumulate in the nucleus, where it binds to TCF/LEF transcription factors, driving luminescence expression. This assay was completed using G9-pCDH glioma cells that were

transfected with the TCF/LEF reporter plasmid. With both BIA and C91 treatments, there was a significant increase in luminescence, with 1 μM BIA exhibiting a 1.95 fold increase and 3 μM C91 exhibiting a 2.07 fold increase compared to the control (**Fig. 5.6C**). Altogether, these results confirm the pharmacological inhibition of GSK-3 expected from both BIA and C91, as well as activation of the WNT/β-catenin pathway.

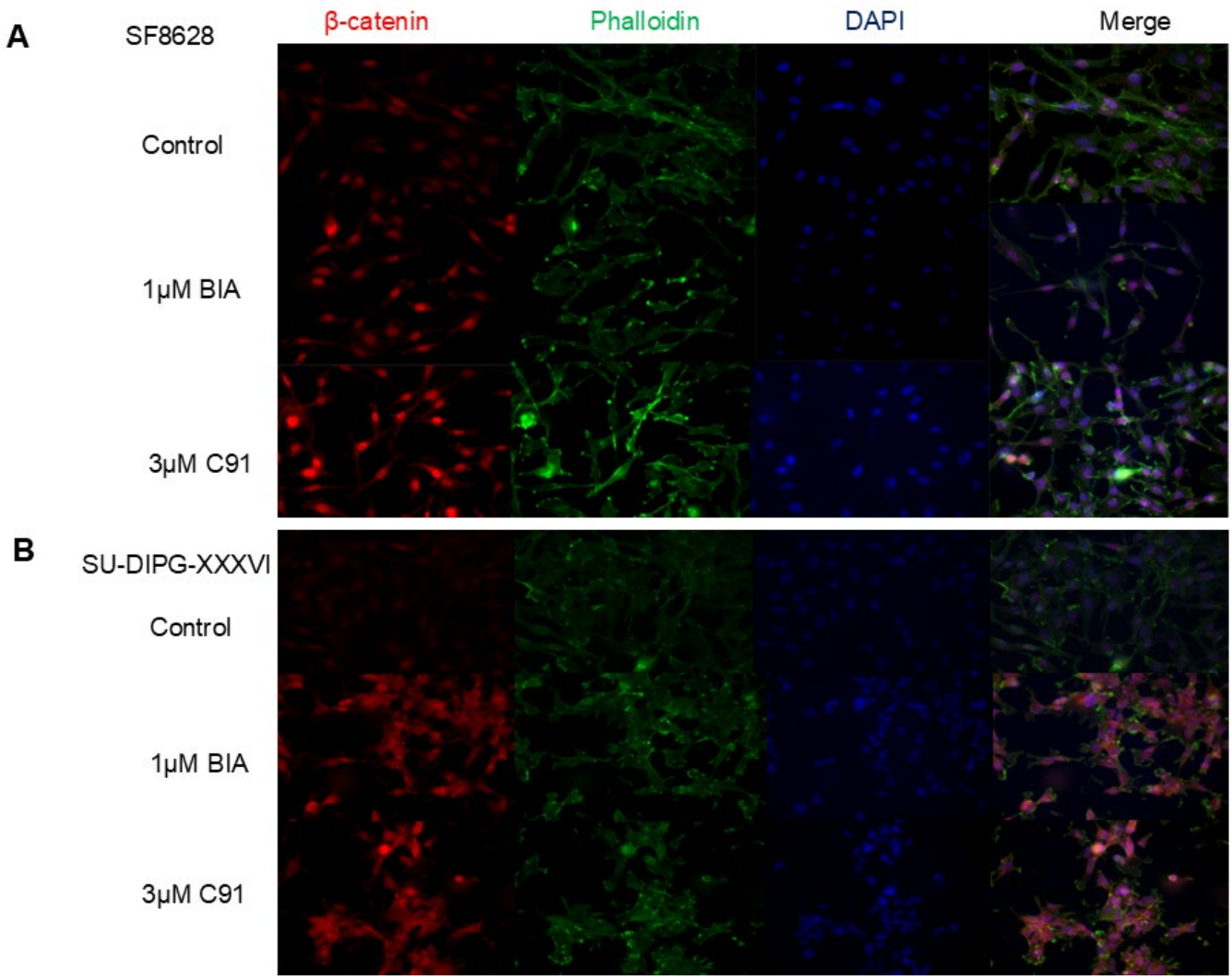

Figure 5.5: Canonical WNT/β-Catenin Signaling pathway active with BIA and C91 treatment. Immunofluorescence staining of **(A)** SF8628 and **(B)** SU-DIPG-36 monolayers treated with 1 μM BIA and 3 μM C91 for 24 hours. Representative image from n=3 individual experiments.

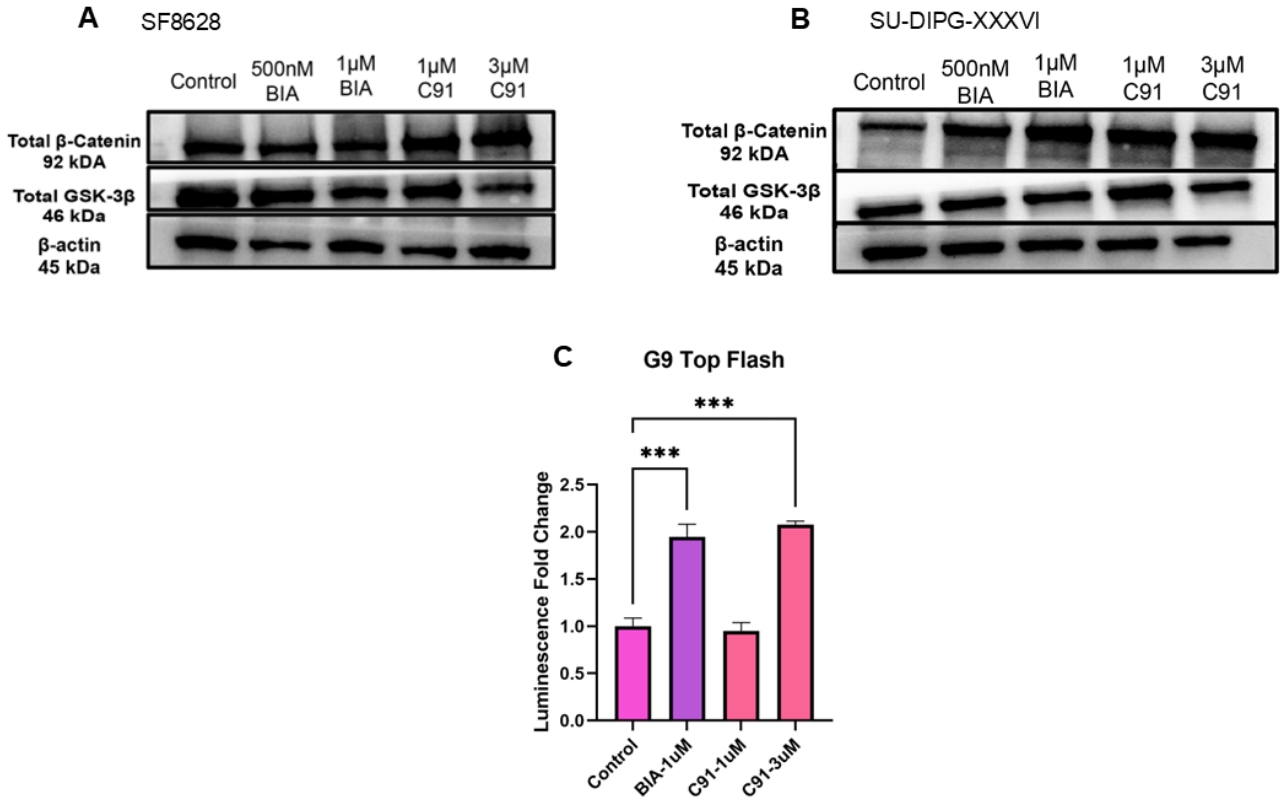

Figure 5.6: Canonical WNT/B-Catenin Signaling pathway active with BIA and C91 treatment. Western blots show increased total β-catenin in **(A) SU-DIPG-36** and **(B)** SF8628. **(C)** TopFlash luciferase reporter assay showing fold change response to GSK-3 inhibition. One-way ANOVA using Dunnett's showed significant luminescence increase with 1 μM BIA (***p= 0.0003) and 3 μM C91 (***p=0.0001) vs control.

5.3 Chapter 5 Summary and Discussion

This chapter worked to establish GSK-3 inhibition as a potent chemosensitizer for DMG therapy. Through high-throughput screening of a panel of 176 FDA-approved drugs, several potential combinations were identified with two leading hits, Vorinostat (HDAC inhibitor) and Gemcitabine (nucleoside analog), validated in pHGG cell lines. Vorinostat validation in the SU-DIPG-36 and KNS-42 cell lines portrayed higher H3K27M DMG-specific sensitivity with both BIA and C91 treatment combinations. This response did not extend to the KNS-42s, which showed no significant response to monotherapy or combination therapy. This specificity of response suggests a mutation-specific vulnerability in those harboring the H3K27M mutation and positions these combinations as powerful pharmacotherapeutic agents for DMG.

Gemcitabine treatment demonstrated efficacy in both DMG cell lines, with more pronounced shifts in IC_{50} observed in SU-DIPG-36s, particularly with BIA treatment. Although there were no significant differences observed between BIA or C91 combinations in the SF8628s, and IC_{50} could not be generated, both combinations showed noticeable, yet submaximal effects, with the highest concentration tested achieving a reduction to ~40% viability. These observations, along with the effects shown in the prior chapters, in which BIA and C91 inhibit DMG and endothelial cell motility and migration whilst simultaneously modulating BBB permeability and increasing the chemosensitivity of DMG cells, highlight the potential of GSK-3 inhibition as a powerful target for focus in DMG pharmacotherapeutic development. Altogether, chapters 3 and 4 established the potent effects of these inhibitors on pediatric glioma proliferation and migration, endothelial motility and migration, barrier function, and BBB permeability across 2D and 3D models. This chapter expands on those

findings by demonstrating these compounds' ability to enhance chemosensitivity in DMG cells, providing the rationale for combinatorial investigations. Utilizing the potent anti-tumorigenic effects of BIA/C91, in combination with a compound that can further enhance those effects through a different mechanism of action, could prove useful for the mechanistically elusive midline glioma by targeting additional compensatory signaling.

To elucidate the underlying mechanisms primarily associated with BIA and C91 treatment, the WNT/β-catenin signaling pathway was examined in the DMG cell lines. Immunofluorescence staining after 24 hour BIA/C91 treatment revealed a marked visual increase in global β-catenin stabilization with both nuclear and diffuse cytoplasmic accumulation compared to their controls. Despite the observed nuclear accumulation of β-catenin in both DMG cell lines, migration was shown to be impaired with treatment of both inhibitors, suggesting a paradoxical engagement in this pathway. Phalloidin staining showed robust actin thinning, disruption of filament structure, and more rounded cell morphology, likely contributing to the observed inhibition of migration, although deeper mechanistic studies investigating this morphological disruption are needed for full confirmation. Western blotting further confirmed these findings, with an observed total β-catenin increase in both cell lines, with total GSK-3β protein levels remaining stable, confirming the pharmacological inhibitory activity of these compounds. Confirmation of functional WNT/β-catenin transcriptional activation was assessed using the TCF/LEF TopFlash luciferase assay in G9-pCDH glioma cells transfected with the TCF/LEF reporter plasmid. 24 hour treatment with both BIA and C91 revealed a significant luminescence signal, with 1 μM BIA showing a fold change of 1.95 and 3 μM C91 showing a fold change of 2.07 relative to their respective controls. This additional preliminary mechanistic exploration helped to establish GSK-3β

inhibition through β-catenin stabilization, as well as the observed cytoskeletal disruption, provided some molecular correlation with the observed anti-migratory effects across pHGG models.

CHAPTER 6: OVERALL DISCUSSION AND CONCLUSIONS

6.1 Overall Discussion and Conclusions

pHGGs represent the leading cause of cancer-related deaths in children, with DMGs representing a particularly devastating subtype [2,3,6,20]. These tumors typically arise from midline brain structures, such as the pons, cerebellum, thalamus, brainstem, and spinal cord, and have a median survival of approximately 9-11 months and a patient survival rate of less than 10% beyond 2 years from diagnosis[21]. Radiotherapy, the current and only standard of care treatment, is only partially effective in treating these tumors, and traditional chemotherapeutics have also been shown to be ineffective at improving survival [58,65]. This is due to their unique anatomical location and infiltrative nature, which typically prevent surgical resection, as well as the BBB and BTB, which prevent systemic chemotherapies from entering the brain [59,145,146,174]. New therapeutic strategies that effectively target tumor behavior and enhance drug delivery across the BBB are urgently needed to improve long-term patient survival. This thesis demonstrates that GSK-3 inhibition can suppress tumor growth and migration while modulating barrier function, establishing a therapeutic strategy that targets both tumor-intrinsic resistance and drug-delivery barriers.

Phenotypic profiling across 2D and 3D models of tumor and endothelial behavior revealed that both BIA and C91 were potent inhibitors of key hallmarks of DMG progression. Using IncuCyte live-cell imaging, pHGG cell lines were shown to be highly sensitive to BIA treatment, with the most pronounced effect observed in the SU-DIPG-36 cell line, where confluence was suppressed at all tested BIA concentrations as early as 12 hours. C91 treatment induced a dose-dependent decrease in confluence across the pHGG cell lines however, the effects were less potent than those of BIA. These effects were also observed in viability assays, in which both BIA and C91 exhibited greater cytotoxicity at higher

concentrations, leading to increased cell death across all cell lines. The effects of GSK-3 inhibition on migration across pHGG cell lines were observed using the wound-healing scratch assay. Both compounds showed a significant reduction in migration across all cell lines, confirming that GSK-3 inhibition can affect the invasive behavior of these glioma cell lines. These results were also seen in the transwell migration assay and continued to support the observed superior potency of BIA in the DMG cell lines. Overall, these findings support a role for GSK-3 in mediating these responses and highlight the enhanced efficacy of multi-kinase inhibition.

Given these observed tumor intrinsic effects, whether GSK-3 inhibition had a similar impact on endothelial cell behavior and barrier function was assessed next. Wound-healing scratch and transwell migration assays showed significant inhibition of endothelial cell motility and migration at sub-IC_{50} concentrations. Tube formation assays demonstrated that HBMECs treated with both BIA and C91 showed reduced network formation of HBMECs compared to those stimulated with the VEGF-A control. BIA treatment elicited a more potent response at both doses (500 nM and 1 μM), leading to near complete endothelial network disruption. The higher dose of C91 (3 μM) also resulted in near complete network disruption, this effect was not observed at either dose, with the lower dose of C91 (1 μM) resulting only in partial network disruption.

The effects of both inhibitors on endothelial cell behavior and barrier function were further assessed in additional 2D/3D models to provide additional validation of BBB/BTB disruption with GSK-3 inhibition. Initially, the hCMEC monolayer TEER assay demonstrated that both BIA and C91 modulated endothelial barrier function, resulting in decreased

resistance compared to the control. Importantly, post-drug washout revealed an initial divergence in their abilities to continuously modulate barrier function, where monolayers treated with BIA showed a continued TEER reduction, and the C91 treated monolayers maintained a stable reduction in resistance compared to the initial treatment addition, suggesting that the multi-kinase activity of BIA may elicit additional long-term effects on barrier function. These effects were further assessed using 3D BBB/BTB spheroid models and assessing 70 kDa dextran and IgG antibody uptake. BBB/BTB spheroids treated with BIA showed enhanced uptake for both dextran and the IgG antibody, while the C91 treated spheroids selectively enhanced only IgG antibody uptake. These results were consistent with prior studies from the lab, which showed that BIA decreased tight junction expression (ZO-1, CDH5, etc.) in hCMEC monolayers, as assessed by RNA sequencing and immunofluorescence staining [93]. Altogether, these findings suggest that inhibition of GSK-3 can effectively modulate BBB/BTB integrity and endothelial cell behavior, with BIAs multi-kinase activity affecting tight junction formation and C91 more selectively modulating permeability. These findings establish GSK-3 inhibitors as viable therapeutic candidates that exhibit anti-proliferative and anti-migrative effects in glioma and enhance barrier permeability.

Next, to better understand the molecular mechanisms underlying the effects seen across the pHGG and endothelial cell lines, downstream signaling pathways associated with GSK-3 inhibition were assessed. Immunofluorescence staining of the DMG cell lines showed global β-catenin stabilization, with nuclear and diffuse cytoplasmic accumulation, following 24 hours of treatment with both inhibitors compared to the control. Phalloidin co-staining further demonstrated effects on cytoskeletal organization, as cells treated with both BIA and C91 showed actin thinning, disruption of filament structure, and a slightly more rounded cell

morphology, consistent with the anti-migratory effects observed in Chapter 3. β-catenin pathway engagement was additionally confirmed through western blot analysis and showed marked increases in total β-catenin levels in both BIA and C91 treated DMG cell lines alongside stable total GSK-3β levels reflecting a pharmacological reduction in functional GSK-3β activity. Transcriptional activation of the WNT/β-catenin pathways was further validated using the TCF/LEF TopFlash luciferase assay. G9-pCDH cells were transfected with the TCF/LEF TopFlash plasmid and treated with either BIA or C91 for 24 hours. Both BIA and C91 elicited significant increases in luminescence (1.95 and 2.07 fold, respectively), confirming GSK-3 inhibition consistent with β-catenin nuclear accumulation, which drives TCF/LEF transcription.

Finally, this thesis worked to establish GSK-3 inhibition as a potent chemosensitizer for DMG therapy through high-throughput drug screening in pHGG cell lines. The drug screen revealed several potential chemotherapeutics that were enhanced by the BIA combination, and further validation of both the BIA and C91 combinations increased chemosensitivity in DMG cell lines to gemcitabine and vorinostat, suggesting overall additive effects. This comprehensive phenotypic study established GSK-3 inhibition as a dual-mechanism therapeutic agent that combats infiltrative resistance and BBB drug impermeability. This was seen through proliferation arrest, cytoskeletal disruption, migration suppression, and increased BBB permeability and DMG chemosensitivity. The consistently greater potency of BIA over C91 across all assays highlights the additional potential of multi-kinase inhibitors that can recruit additional pathway engagement to amplify the GSK-3-mediated effects. The central hypothesis that multi-kinase and/or selective GSK-3 inhibition can reduce DMG aggressiveness and modulate BBB/BTB permeability to enhance chemotherapeutic efficacy

was validated across several functional endpoints.

Most chemotherapeutics cannot access brainstem tumors because of the rigorously intact BBB/BTB, with radiotherapy only extending progression-free survival by 6 months due to their invasive nature, evading therapeutic intervention and driving eventual tumor recurrence. GSK-3 inhibition offers a multimodal therapeutic approach that directly suppresses tumor proliferation and migration, reduces endothelial motility, and modulates barrier permeability to enhance chemotherapeutic drug delivery into the brain. This directly targets the mechanisms underlying DMG therapeutic resistance, positioning GSK-3 inhibition as a powerful focus for DMG pharmacotherapy development. Altogether, this thesis characterized the potent effects of these inhibitors on pediatric glioma growth and migration, endothelial motility, barrier function, and selective barrier permeability, establishing a preclinical foundation for the use of GSK-3 inhibitors for DMG treatment. Further investigation into these compounds and their effects is encouraged, as they offer an intriguing path toward combating DMG resistance.

6.1.1 Limitations

This study has several limitations that should be addressed in future studies. First, these experiments were conducted *in vitro* and may not fully capture the complexity of multicellular interactions within the intact BBB/BTB in DMG, which can only be recapitulated *in vivo*. Although the 3D BBB/BTB spheroids helped to improve the physiological relevance of the barrier studies, they cannot fully recapitulate the *in vivo* microenvironment. Next, the number of cell lines used should be expanded to account for the additional mutations present in these glioma cell lines and to ensure that this proposed therapeutic is truly beneficial for

all DMG tumor types. Another limitation is that, because of BIA's multi-kinase activity, a full mechanistic investigation of its potential off-target effects is needed to ensure its safety profile. As such, the observed differences in this work should be interpreted as primarily phenotypic rather than mechanistic. Also, further investigation of additional clinically relevant agents in combination with these compounds should be conducted to assess whether synergistic combinations can slow disease progression by leveraging the effects of GSK-3 inhibition on invasion and barrier integrity.

6.1.2 Future Directions

This dissertation provides a foundation for future mechanistic investigations that are critical to optimizing the translational potential of GSK-3 inhibition as a DMG treatment. To understand the complex role that GSK-3 plays in modulating barrier function and endothelial and tumor cell biology, deeper pathway investigation should be conducted using RNA sequencing, western blots, and immunofluorescence staining. These will help to distinguish the phenotypic differences observed in this study. *In vivo* validation should also be prioritized as this remains a critical next step towards tangible clinical impact. DMG-luciferase cells need to be injected into the pons to enable visualization and monitoring of tumor growth. Use of an *in vivo* model to validate these findings in the context of all multicellular interactions present is imperative in determining the therapeutic impact of GSK-3 inhibition for DMG treatment. A zebrafish model would also enable faster, more cost-effective screening of the vascular effects of GSK-3 inhibition, and studies investigating these effects on vascular formation and blood flow are currently underway. Furthermore, additional selective GSK-3 inhibitors and indirubin derivatives will be tested to help confirm pathway engagement in a larger panel of pediatric high-grade glioma cell lines, with an emphasis on DMG cell lines

harboring additional mutations, such as ACVR1. These future studies are critical next steps to build on the phenotypic framework established in this work and ultimately translate it into the clinic. In conclusion, this work extensively assessed the therapeutic potential of GSK-3 inhibition, providing compelling evidence for further development as a DMG treatment. While current limitations necessitate progression to *in vivo* models, the findings highlight GSK-3 as a promising therapeutic target to address the biological complexity of DMG.

Appendices

Supplementary Figure 5.1 Full Drug Screen Reports

Report #1
Drug screening for searching for FDA approved drugs (1μM) in combination with BIA

Shengliang Zhang

Drug discovery shared resource, Legorreta Cancer Center, Brown University Date: 11-05-2023

We set up this drug screening for Dr. Sean Lawler lab to look for FDA approved oncology drugs(1μM) that may synergize or sensitize tumor cells to the BIA killing cancer cells.

Methods

DIPG and KNS-42 were seeded on 96-well plates at Dr. Sean Lawler lab and subjected to the drug screening at the core facility.

The cells were treated with BIA and the FDA approved drugs from the library (FDA drug plate #1) or the FDA drugs (Plate #1) alone.

The cells were treated with 1μM of FDA approved oncology drugs for 72 hours.

Cell viability was examined by Celltiter-Glo assay, and the data was normalized to the DMSO treatment as a control.

Results

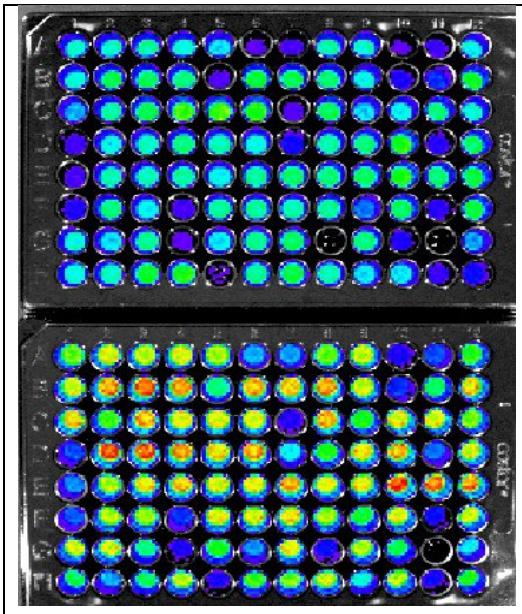

Figure 1. **Imaging CellTiter-Glo bioluminescence cell viability of DIPG cells treated with 1μM of FDA approved drugs from the drug plate#1.** The upper plate was treated with the BIA+FDA approved drugs. The bottom plate was treated with FDA approved drug alone.

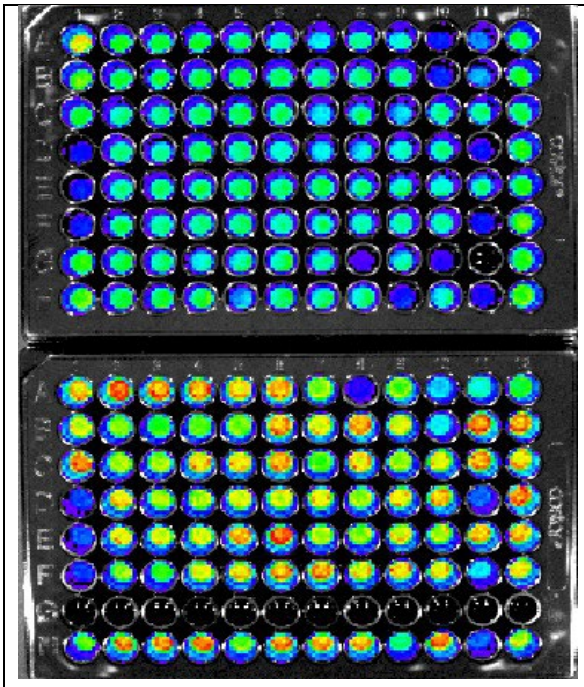

Figure 2**. Imaging CellTiter-Glo bioluminescence cell viability of KNS-42S cells treated with 1μM of FDA approved drugs from the drug plate#1.** The upper plate was
treated with the BIA+FDA approved drugs. The bottom plate was
treated with FDA approved drug alone.
Note: No cells were seeded on the wells through G1 to G12 of the "FDA" cell culture plate (bottom).

Table 1. Drug screening on the FDA approved drugs (Plate #1, 1μM) using DIPG cells

Relative cell viability	Relative cell viability	Change of the cell viability	NSC	CAS	DRUG NAME (USAN)	MW
FDA drug	BIA+FDA	FDA/Comb				
0.21	0.03	6.89	279836	65271-80-9	Mitoxantrone	444.49
0.04	0.07	0.54	754143	128517-07-7	Romidepsin	540.69
0.20	0.13	1.60	609699	119413-54-6	Topotecan hydrochloride	457.91
0.16	0.13	1.24	613327	122111-03-9	Gemcitabine hydrochloride	299.65
0.44	0.15	2.98	701852	149647-78-9	Vorinostat	264.32
0.17	0.16	1.10	66847	50-35-1	Thalidomide	258.23
0.69	0.17	4.01	105014	4291-63-8	Cladribine	285.69
0.19	0.18	1.06	606869	123318-82-1	Clofarabine	303.68
0.42	0.19	2.28	26980	50-07-7	Mitomycin	334.33
0.32	0.19	1.66	763932	755037-03-7	Regorafenib	482.8
0.26	0.22	1.22	63878	69-74-9	Cytarabine hydrochloride	279.7
0.32	0.23	1.39	Cisplatin Ctl			
0.17	0.23	0.74	758253	26833-87-4	Omacetaxine mepesuccinate	545.63
0.34	0.26	1.32	256439	57852-57-0	Idarubicin hydrochloride	533.96
0.20	0.26	0.76	747973	219989-84-1	Ixabepilone	506.7
0.27	0.27	1.02	732517	863127-77-9	Dasatinib	488.01
0.63	0.27	2.31	754230	146464-95-1	Pralatrexate	477.48

0.51	0.33	1.55	758774	414864-00-9	Belinostat	318.35
0.70	0.37	1.92	761431	1029872-54-5	Vemurafenib	489.91
0.72	0.54	1.32	747974	84449-90-1	Raloxifene	473.59
1.06	0.69	1.53	85998	18883-66-4	Streptozocin	265.22
0.83	0.70	1.18	755384	357166-30-4	Pemetrexed disodium salt	471.38
1.07	0.73	1.48	BIA Ctrl			
0.93	0.76	1.23	6396	52-24-4	Thiotepa	189.22
0.48	0.76	0.63	740	59-05-2	Methotrexate	454.44
0.74	0.77	0.96	218321	53910-25-1	Pentostatin	268.27
1.08	0.77	1.40	753686	763113-22-0	Olaparib	434.46
0.85	0.77	1.10	755605	915087-33-1	Enzalutamide	464.42
1.09	0.78	1.41	737754	635702-64-6	Pazopanib hydrochloride	473.98
1.13	0.79	1.44	102816	320-67-2	Azacitidine	244.21
1.09	0.79	1.38	718781	183319-69-9	Erlotinib hydrochloride	429.9
0.92	0.79	1.16	27640	50-91-9	Floxuridine	246.19
1.28	0.80	1.59	752	154-42-7	Thioguanine	167.19
1.11	0.81	1.37	32065	127-07-1	Hydroxyurea	76.05
1.06	0.82	1.30	122758	302-79-4	Tretinoin	300.44
1.22	0.82	1.48	719345	112809-51-5	Letrozole	285.3
1.07	0.87	1.24	45388	4342-03-4	Dacarbazine	182.18
0.97	0.87	1.11	312887	75607-67-9	Fludarabine phosphate	365.21
1.27	0.89	1.43	750	55-98-1	Busulfan	246.3
1.07	0.90	1.19	13875	645-05-6	Altretamine	210.28
0.88	0.91	0.97	19893	51-21-8	Fluorouracil	130.08
0.35	0.91	0.39	18509	5451-09-2	Aminolevulinic acid hydrochloride	167.59
1.16	0.92	1.26	119875	15663-27-1	Cisplatin	300.06
0.95	0.92	1.03	755	50-44-2	Mercaptopurine	152.18
0.88	0.94	0.95	715055	184475-35-2	Gefitinib	446.9
0.82	0.94	0.87	750690	557795-19-4	Sunitinib	398.47
1.07	0.95	1.12	71423	595-33-5	Megestrol acetate	384.51
1.13	0.95	1.18	34462	66-75-1	Uracil mustard	252.1
1.26	0.96	1.32	127716	2353-33-5	Decitabine	228.21
1.05	0.96	1.09	760766	443913-73-3	Vandetanib	475.36
1.03	0.97	1.06	169780	24584-09-6	Dexrazoxane	268.27
1.25	0.98	1.28	712807	154361-50-9	Capecitabine	359.35
0.93	0.98	0.94	757441	319460-85-0	Axitinib	386.47
1.08	0.99	1.09	747972	191732-72-6	Lenalidomide	259.26
0.59	0.99	0.60	45923	298-81-7	Methoxsalen	216.19
0.74	0.99	0.75	3088	305-03-3	Chlorambucil	304.22
1.03	1.00	1.04	755985	121032-29-9	Nelarabine	297.27

0.36	1.00	0.36	775351	19171-19-8	Pomalidomide	273.25

1.11	1.00	1.11	755986	879085-55-9	Vismodegib	421.3
1.31	1.00	1.30	92859	1327-53-3	Arsenic trioxide	197.84
1.23	1.01	1.22	26271	6055-19-2	Cyclophosphamide	261.09
1.25	1.01	1.24	1390	315-30-0	Allopurinol	136.11
0.93	1.02	0.91	762	55-86-7	Mechlorethamine hydrochloride	192.52
1.15	1.04	1.11	747599	641571-10-0	Nilotinib	529.51
1.03	1.04	0.99	756655	179324-69-7	Bortezomib	384.24
1.21	1.04	1.16	38721	53-19-0	Mitotane	320.04
0.89	1.05	0.85	761910	936563-96-1	Ibrutinib	440.5
1.22	1.07	1.15	719627	169590-42-5	Celecoxib	381.37
1.05	1.08	0.97	759224	870281-82-6	Idelalisib	415.42
1.22	1.09	1.12	362856	85622-93-1	Temozolomide	194.15
1.15	1.09	1.06	25154	54-91-1	Pipobroman	356.06
0.98	1.09	0.90	750691	439081-18-2	Afatinib	485.94
0.99	1.09	0.91	138783	3543-75-7	Bendamustine hydrochloride	394.73
1.24	1.11	1.12	713563	107868-30-4	Exemestane	296.4
0.79	1.16	0.68	241240	41575-94-4	Carboplatin	371.25
0.61	1.18	0.51	79037	13010-47-4	Lomustine	233.7
1.16	1.20	0.97	743414	152459-95-5	Imatinib	493.61
0.87	1.24	0.71	77213	366-70-1	Procarbazine hydrochloride	257.76
1.11	1.25	0.89	719344	120511-73-1	Anastrozole	293.37
1.23	1.25	0.98	747971	284461-73-0	Sorafenib	464.82
1.14	1.27	0.90	109724	3778-73-2	Ifosfamide	261.09
1.14	1.29	0.88	409962	154-93-8	Carmustine	214.05

Table 2. Drug screening on the FDA approved drugs (Plate #1, 1μM) using KNS-42 cells

Relative cell viability	Relative cell viability	Change of the cell viability	NSC	CAS	DRUG NAME (USAN)	MW
FDA drug	BIA+FDA	FDA/Comb				
#####	0.05	#####	754143	128517-07-7	Romidepsin	540.69
#####	0.17	#####	279836	65271-80-9	Mitoxantrone	444.49
#####	0.21	#####	754230	146464-95-1	Pralatrexate	477.48
0.28	0.25	1.12	256439	57852-57-0	Idarubicin hydrochloride	533.96
0.25	0.27	0.91	758253	26833-87-4	Omacetaxine mepesuccinate	545.63
0.23	0.29	0.81	Cisplatin Ctrl			
0.44	0.30	1.48	609699	119413-54-6	Topotecan hydrochloride	457.91
0.46	0.30	1.54	732517	863127-77-9	Dasatinib	488.01
0.39	0.30	1.28	747973	219989-84-1	Ixabepilone	506.7
0.51	0.32	1.63	740	59-05-2	Methotrexate	454.44
0.56	0.45	1.25	763932	755037-03-7	Regorafenib	482.8
1.13	0.49	2.31	761431	1029872-54-5	Vemurafenib	489.91
0.69	0.54	1.26	613327	122111-03-9	Gemcitabine hydrochloride	299.65
0.83	0.56	1.49	755384	357166-30-4	Pemetrexed disodium salt	471.38
0.92	0.60	1.52	26980	50-07-7	Mitomycin	334.33
0.79	0.62	1.27	606869	123318-82-1	Clofarabine	303.68
0.84	0.63	1.34	750690	557795-19-4	Sunitinib	398.47
0.95	0.63	1.51	758774	414864-00-9	Belinostat	318.35
0.90	0.68	1.33	718781	183319-69-9	Erlotinib hydrochloride	429.9
#####	0.69	#####	66847	50-35-1	Thalidomide	258.23
0.81	0.71	1.13	750	55-98-1	Busulfan	246.3
0.93	0.72	1.30	755986	879085-55-9	Vismodegib	421.3
0.94	0.72	1.30	747599	641571-10-0	Nilotinib	529.51
#####	0.72	#####	761910	936563-96-1	Ibrutinib	440.5
0.88	0.73	1.21	757441	319460-85-0	Axitinib	386.47
0.91	0.73	1.24	719345	112809-51-5	Letrozole	285.3
1.13	0.74	1.53	701852	149647-78-9	Vorinostat	264.32
0.79	0.74	1.07	747971	284461-73-0	Sorafenib	464.82
1.02	0.74	1.36	71423	595-33-5	Megestrol acetate	384.51
1.01	0.75	1.36	719627	169590-42-5	Celecoxib	381.37
1.05	0.75	1.40	760766	443913-73-3	Vandetanib	475.36
0.18	0.75	0.24	312887	75607-67-9	Fludarabine phosphate	365.21

0.86	0.76	1.14	750691	439081-18-2	Afatinib	485.94
0.83	0.77	1.08	19893	51-21-8	Fluorouracil	130.08
#####	0.77	#####	138783	3543-75-7	Bendamustine hydrochloride	394.73
0.87	0.77	1.13	755	50-44-2	Mercaptopurine	152.18
0.93	0.77	1.21	755605	915087-33-1	Enzalutamide	464.42
0.90	0.77	1.17	759224	870281-82-6	Idelalisib	415.42
0.78	0.77	1.01	756655	179324-69-7	Bortezomib	384.24
0.98	0.78	1.26	755985	121032-29-9	Nelarabine	297.27
0.98	0.79	1.25	743414	152459-95-5	Imatinib	493.61
0.89	0.79	1.13	747974	84449-90-1	Raloxifene	473.59
0.92	0.79	1.16	753686	763113-22-0	Olaparib	434.46
0.93	0.80	1.17	737754	635702-64-6	Pazopanib hydrochloride	473.98
0.80	0.80	1.00	362856	85622-93-1	Temozolomide	194.15
#####	0.80	#####	218321	53910-25-1	Pentostatin	268.27
0.92	0.80	1.15	752	154-42-7	Thioguanine	167.19
0.98	0.80	1.22	38721	53-19-0	Mitotane	320.04

1.09	0.81	1.35	712807	154361-50-9	Capecitabine	359.35
0.87	0.82	1.07	34462	66-75-1	Uracil mustard	252.1
0.63	0.82	0.77	27640	50-91-9	Floxuridine	246.19
1.04	0.82	1.26	85998	18883-66-4	Streptozocin	265.22
0.87	0.83	1.05	63878	69-74-9	Cytarabine hydrochloride	279.7
0.86	0.83	1.04	13875	645-05-6	Altretamine	210.28
0.70	0.83	0.84	762	55-86-7	Mechlorethamine hydrochloride	192.52
1.08	0.83	1.30	719344	120511-73-1	Anastrozole	293.37
0.72	0.83	0.86	92859	1327-53-3	Arsenic trioxide	197.84
0.91	0.84	1.08	241240	41575-94-4	Carboplatin	371.25
0.90	0.85	1.07	119875	15663-27-1	Cisplatin	300.06
#####	0.85	#####	45923	298-81-7	Methoxsalen	216.19
1.07	0.86	1.25	747972	191732-72-6	Lenalidomide	259.26
1.13	0.86	1.30	45388	4342-03-4	Dacarbazine	182.18
1.17	0.87	1.34	32065	127-07-1	Hydroxyurea	76.05
0.88	0.88	1.00	715055	184475-35-2	Gefitinib	446.9
0.99	0.88	1.13	409962	154-93-8	Carmustine	214.05
1.12	0.88	1.27	102816	320-67-2	Azacitidine	244.21
1.10	0.88	1.24	713563	107868-30-4	Exemestane	296.4
0.78	0.88	0.89	1390	315-30-0	Allopurinol	136.11
0.90	0.89	1.01	169780	24584-09-6	Dexrazoxane	268.27
0.77	0.91	0.85	127716	2353-33-5	Decitabine	228.21
0.98	0.91	1.07	122758	302-79-4	Tretinoin	300.44
#####	0.92	#####	775351	19171-19-8	Pomalidomide	273.25
#####	0.92	#####	6396	52-24-4	Thiotepa	189.22
0.97	0.93	1.05	109724	3778-73-2	Ifosfamide	261.09
0.82	0.93	0.88	26271	6055-19-2	Cyclophosphamide	261.09
0.84	0.93	0.90	105014	4291-63-8	Cladribine	285.69
0.85	0.94	0.90	25154	54-91-1	Pipobroman	356.06
0.92	0.95	0.97	3088	305-03-3	Chlorambucil	304.22
0.90	0.96	0.93	79037	13010-47-4	Lomustine	233.7
0.93	0.97	0.96	77213	366-70-1	Procarbazine hydrochloride	257.76
0.87	0.98	0.89	18509	5451-09-2	Aminolevulinic acid hydrochloride	167.59
1.00	1.16	0.86	BIA Ctrl			

####, data is not available to read out because no cells were seeded on the wells through G1 to G12 of the cell culture plate.

Report #2
Drug screening for searching for FDA approved drugs (1μM) in combination with BIA

Shengliang Zhang

Drug discovery shared resource, Legorreta Cancer Center, Brown University Date: 11-13-2023

We set up this drug screening for Dr. Sean Lawler lab to look for FDA approved oncology drugs(1μM) that may synergize or sensitize tumor cells to the BIA killing cancer cells.

Methods

DIPG and KNS-42 were seeded on 96-well plates at Dr. Sean Lawler lab and subjected to the drug screening at the core facility.

The cells were treated with BIA and the FDA approved drugs from the library (FDA drug plate #1 and #2) or the FDA drugs (Plate #1 and #2) alone.

The cells were treated with 1μM of FDA approved oncology drugs for 72 hours.

Cell viability was examined by Celltiter-Glo assay, and the data was normalized to the DMSO treatment as a control.

Results

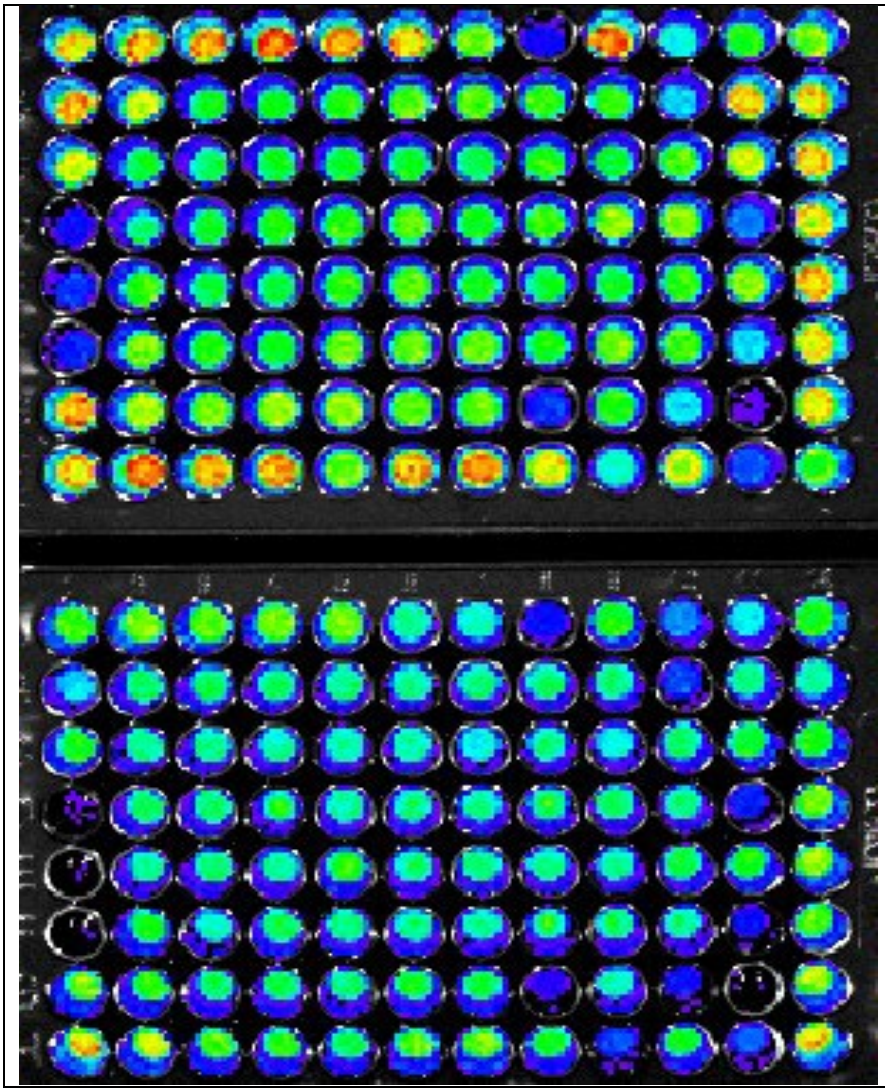

Figure 1**. Imaging CellTiter-Glo bioluminescence cell viability of KNS-42 cells treated with 1μM of FDA approved drugs from the drug plate#1.** The upper plate was treated with the FDA approved drugs. The bottom plate was treated with the BIA+FDA approved drugs

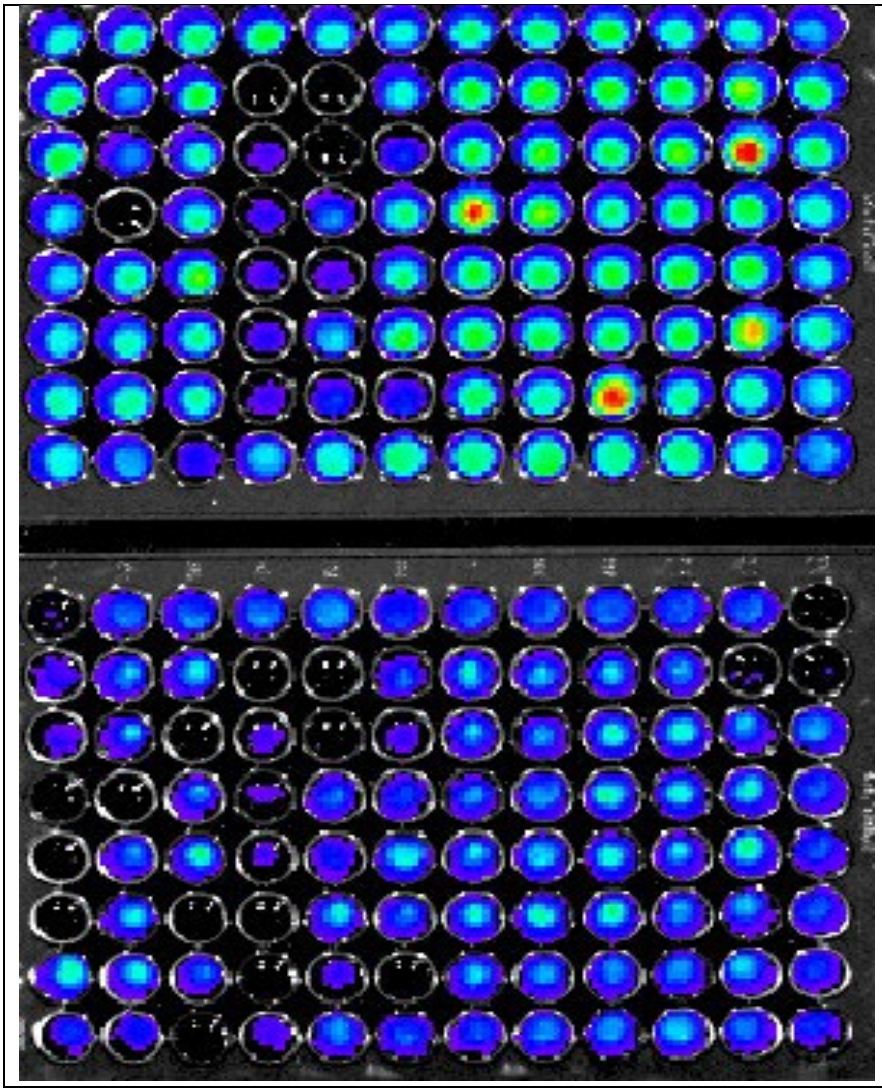

Figure 2. **Imaging CellTiter-Glo bioluminescence cell viability of DIPG cells treated with 1μM of FDA approved drugs from the drug plate#2.** The upper plate was treated with the FDA approved drugs. The bottom plate was treated with the BIA+FDA approved drugs

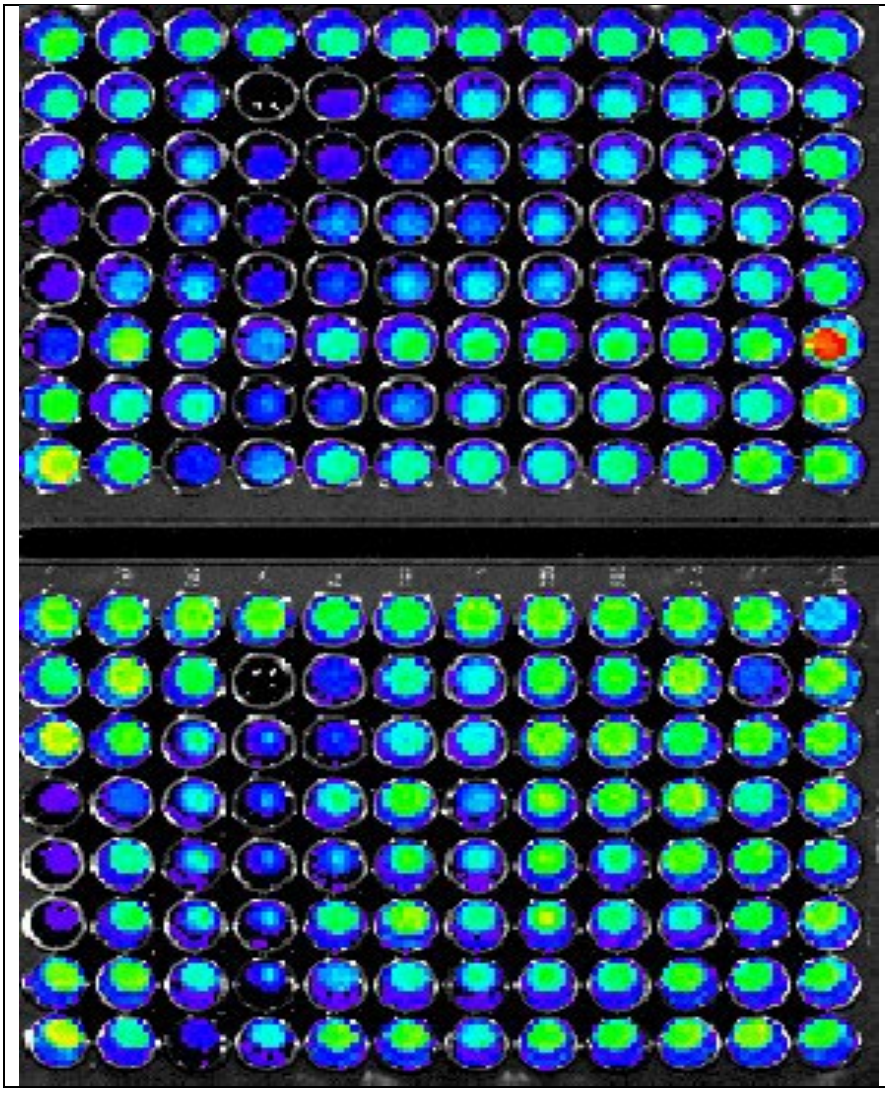

Figure 3. Imaging CellTiter-Glo bioluminescence cell viability of KNS42 cells treated with 1μM of FDA approved drugs from the drug plate#2. The upper plate was treated with the FDA approved drugs. The bottom plate was treated with the BIA+FDA approved drugs

Table 1. Drug screening on the FDA approved drugs (Plate #1, 1μM) using KNS-42 cells

Relative cell viability	Relative cell viability	Change of the cell viability	NSC	CAS	DRUG NAME (USAN)	MW
FDA drug	BIA+FDA	FDA/Comb				
0.20	0.08	2.61	cisplatin ctrl			
0.09	0.08	1.06	754143	128517-07-7	Romidepsin	540.69
0.23	0.19	1.21	279836	65271-80-9	Mitoxantrone	444.49
0.42	0.23	1.85	747973	219989-84-1	Ixabepilone	506.7

0.42	0.24	1.79	754230	146464-95-1	Pralatrexate	477.48
0.31	0.30	1.03	256439	57852-57-0	Idarubicin hydrochloride	533.96
0.17	0.31	0.55	312887	75607-67-9	Fludarabine phosphate	365.21
0.51	0.32	1.60	740	59-05-2	Methotrexate	454.44
0.30	0.33	0.88	758253	26833-87-4	Omacetaxine mepesuccinate	545.63
0.38	0.37	1.01	732517	863127-77-9	Dasatinib	488.01
0.45	0.51	0.87	609699	119413-54-6	Topotecan hydrochloride	457.91
0.68	0.61	1.13	27640	50-91-9	Floxuridine	246.19
0.70	0.62	1.14	761910	936563-96-1	Ibrutinib	440.5
0.58	0.63	0.92	755384	357166-30-4	Pemetrexed disodium salt	471.38
0.59	0.64	0.92	606869	123318-82-1	Clofarabine	303.68
0.75	0.65	1.14	750691	439081-18-2	Afatinib	485.94
0.66	0.66	1.00	757441	319460-85-0	Axitinib	386.47
0.68	0.66	1.02	763932	755037-03-7	Regorafenib	482.8
0.77	0.66	1.16	71423	595-33-5	Megestrol acetate	384.51
0.70	0.68	1.03	755	50-44-2	Mercaptopurine	152.18
0.64	0.68	0.94	26271	6055-19-2	Cyclophosphamide	261.09
0.56	0.68	0.83	34462	66-75-1	Uracil mustard	252.1
0.60	0.69	0.88	759224	870281-82-6	Idelalisib	415.42
0.76	0.69	1.10	45923	298-81-7	Methoxsalen	216.19
0.83	0.70	1.19	218321	53910-25-1	Pentostatin	268.27
0.78	0.71	1.10	747974	84449-90-1	Raloxifene	473.59
0.59	0.71	0.83	409962	154-93-8	Carmustine	214.05
0.82	0.71	1.16	66847	50-35-1	Thalidomide	258.23
0.81	0.71	1.13	743414	152459-95-5	Imatinib	493.61
0.77	0.71	1.07	755985	121032-29-9	Nelarabine	297.27
0.76	0.73	1.04	747972	191732-72-6	Lenalidomide	259.26
0.60	0.73	0.81	756655	179324-69-7	Bortezomib	384.24
0.65	0.73	0.89	758774	414864-00-9	Belinostat	318.35
0.59	0.74	0.81	109724	3778-73-2	Ifosfamide	261.09
0.67	0.74	0.91	719627	169590-42-5	Celecoxib	381.37
0.70	0.74	0.95	119875	15663-27-1	Cisplatin	300.06
0.61	0.74	0.82	719344	120511-73-1	Anastrozole	293.37
0.77	0.74	1.04	169780	24584-09-6	Dexrazoxane	268.27
0.73	0.74	0.99	719345	112809-51-5	Letrozole	285.3
0.56	0.74	0.75	13875	645-05-6	Altretamine	210.28
0.52	0.74	0.70	362856	85622-93-1	Temozolomide	194.15
0.82	0.75	1.09	613327	122111-03-9	Gemcitabine hydrochloride	299.65
0.58	0.76	0.77	19893	51-21-8	Fluorouracil	130.08
0.58	0.76	0.77	750	55-98-1	Busulfan	246.3
0.73	0.76	0.95	713563	107868-30-4	Exemestane	296.4
0.95	0.77	1.24	761431	1029872-54-5	Vemurafenib	489.91
0.64	0.77	0.82	25154	54-91-1	Pipobroman	356.06

0.45	0.78	0.58	752	154-42-7	Thioguanine	167.19
0.78	0.78	1.00	26980	50-07-7	Mitomycin	334.33
0.72	0.78	0.92	750690	557795-19-4	Sunitinib	398.47
0.98	0.78	1.24	755605	915087-33-1	Enzalutamide	464.42
0.78	0.79	0.99	138783	3543-75-7	Bendamustine hydrochloride	394.73
0.78	0.79	0.98	775351	19171-19-8	Pomalidomide	273.25
0.97	0.80	1.22	715055	184475-35-2	Gefitinib	446.9
0.81	0.80	1.01	755986	879085-55-9	Vismodegib	421.3
0.66	0.80	0.82	105014	4291-63-8	Cladribine	285.69
0.58	0.80	0.73	127716	2353-33-5	Decitabine	228.21
0.74	0.81	0.92	38721	53-19-0	Mitotane	320.04
0.64	0.81	0.79	63878	69-74-9	Cytarabine hydrochloride	279.7
0.66	0.81	0.82	753686	763113-22-0	Olaparib	434.46
0.69	0.82	0.84	712807	154361-50-9	Capecitabine	359.35
1.08	0.82	1.32	77213	366-70-1	Procarbazine hydrochloride	257.76
0.81	0.83	0.98	1390	315-30-0	Allopurinol	136.11
0.71	0.83	0.85	747971	284461-73-0	Sorafenib	464.82
0.59	0.83	0.71	92859	1327-53-3	Arsenic trioxide	197.84
0.70	0.83	0.84	737754	635702-64-6	Pazopanib hydrochloride	473.98
0.99	0.84	1.19	701852	149647-78-9	Vorinostat	264.32
0.86	0.86	1.00	6396	52-24-4	Thiotepa	189.22
0.78	0.87	0.90	762	55-86-7	Mechlorethamine hydrochloride	192.52
1.07	0.89	1.21	79037	13010-47-4	Lomustine	233.7
0.91	0.90	1.01	BIA CTRL			
0.69	0.92	0.76	122758	302-79-4	Tretinoin	300.44
1.08	0.92	1.17	3088	305-03-3	Chlorambucil	304.22
0.81	0.93	0.87	747599	641571-10-0	Nilotinib	529.51
0.83	0.94	0.89	760766	443913-73-3	Vandetanib	475.36
1.11	0.99	1.11	241240	41575-94-4	Carboplatin	371.25
1.17	1.04	1.12	18509	5451-09-2	Aminolevulinic acid hydrochloride	167.59
1.08	1.09	0.99	718781	183319-69-9	Erlotinib hydrochloride	429.9
1.03	1.22	0.84	45388	4342-03-4	Dacarbazine	182.18
0.97	1.23	0.79	32065	127-07-1	Hydroxyurea	76.05
1.11	1.25	0.89	102816	320-67-2	Azacitidine	244.21
1.04	1.28	0.82	85998	18883-66-4	Streptozocin	265.22

Table 2. Drug screening on the FDA approved drugs (Plate #2, 1µM) using DIPG cells

Relative cell viability	Relative cell viability	Change of the cell viability	NSC	CAS	DRUG NAME (USAN)	MW
FDA drug	BIA+FDA	FDA/Comb				
0.02	0.03	0.74	24559	18378-89-7	Plicamycin	1085.16
0.01	0.03	0.47	758252	868540-17-4	Carfilzomib	719.92
0.74	0.03	24.08	Cisplatin CTRL			
0.02	0.04	0.68	82151	23541-50-6	Daunorubicin hydrochloride	563.98
0.02	0.04	0.49	3053	50-76-0	Dactinomycin	1255.43
0.22	0.10	2.31	49842	143-67-9	Vinblastine sulfate	909.06
0.31	0.13	2.44	122819	29767-20-2	Teniposide	656.66
0.34	0.15	2.29	756645	877399-52-5	Crizotinib	450.34
0.20	0.16	1.28	67574	2068-78-2	Vincristine sulfate	923.04
0.81	0.16	5.04	758246	871700-17-3	Trametinib	615.4
0.70	0.16	4.32	776422	1032900-25-6	Ceritinib	558.14
0.22	0.34	0.63	761432	183133-96-2	Cabazitaxel	835.94
0.20	0.36	0.55	125973	33069-62-4	Paclitaxel	853.92
0.18	0.42	0.43	628503	114977-28-5	Docetaxel	807.89
0.35	0.46	0.75	266046	61825-94-3	Oxaliplatin	397.29
0.35	0.48	0.73	369100	99011-02-6	Imiquimod	240.31
0.74	0.50	1.47	226080	53123-88-9	Sirolimus	914.18
0.91	0.51	1.77	BIA Ctrl			
0.69	0.68	1.01	256942	56390-09-1	Epirubicin hydrochloride	579.99
0.20	0.77	0.27	608210	125317-39-7	Vinorelbine tartrate	1079
0.80	0.84	0.96	764134	1195768-06-9	Dabrafenib mesylate	615.65
0.77	0.90	0.85	616348	100286-90-6	Irinotecan hydrochloride	623.15
0.77	0.91	0.85	296961	20537-88-6	Amifostine	214.22
0.89	0.91	0.98	721517	118072-93-8	Zoledronic acid	272.09
0.49	0.97	0.51	765694	380843-75-4	Bosutinib	530.45
0.88	0.98	0.89	123127	25316-40-9	Doxorubicin hydrochloride	579.99
0.49	0.99	0.49	125066	9041-93-4	Bleomycin sulfate	1512.61
0.79	1.02	0.78	9706	51-18-3	Triethylenemelamine	204.23
1.04	1.07	0.97	749226	154229-19-3	Abiraterone	349.51
0.56	1.17	0.48	758487	943319-70-8	Ponatinib	532.55
0.92	1.18	0.78	761388	110078-46-1	Plerixafor	502.79
0.85	1.18	0.72	761068	849217-68-1	Cabozantinib	501.51
0.83	1.25	0.66	141540	33419-42-0	Etoposide	588.56
0.91	1.26	0.72	702294	52205-73-9	Estramustine phosphate sodium	564.35
0.96	1.27	0.75	180973	54965-24-1	Tamoxifen citrate	563.65

0.67	1.34	0.50	683864	162635-04-3	Temsirolimus	1030.29

1.03	1.34	0.77	246131	56124-62-0	Valrubicin	723.64
0.91	1.35	0.67	745750	231277-92-2	Lapatinib	581.06
1.04	1.40	0.74	719276	129453-61-8	Fulvestrant	606.75
0.81	1.52	0.53	733504	159351-69-6	Everolimus	958.24
0.86	1.68	0.51	8806	3223-07-2	Melphalan hydrochloride	341.66

Table 3. Drug screening on the FDA approved drugs (Plate #2, 1μM) using KNS-42 cells

Relative cell viability	Relative cell viability	Change of the cell viability	NSC	CAS	DRUG NAME (USAN)	MW
FDA drug	BIA+FDA	FDA/Comb				
0.04	0.07	0.52	758252	868540-17-4	Carfilzomib	719.92
0.19	0.10	1.80	cisplatin Ctrl			
0.28	0.17	1.63	122819	29767-20-2	Teniposide	656.66
0.21	0.21	0.99	125973	33069-62-4	Paclitaxel	853.92
0.19	0.22	0.89	628503	114977-28-5	Docetaxel	807.89
0.16	0.22	0.71	24559	18378-89-7	Plicamycin	1085.16
0.28	0.22	1.24	67574	2068-78-2	Vincristine sulfate	923.04
0.20	0.24	0.83	761432	183133-96-2	Cabazitaxel	835.94
0.43	0.25	1.72	49842	143-67-9	Vinblastine sulfate	909.06
0.14	0.29	0.47	3053	50-76-0	Dactinomycin	1255.43
0.27	0.31	0.88	608210	125317-39-7	Vinorelbine tartrate	1079
0.14	0.34	0.41	82151	23541-50-6	Daunorubicin hydrochloride	563.98
0.41	0.39	1.06	719276	129453-61-8	Fulvestrant	606.75
0.76	0.39	1.93	758246	871700-17-3	Trametinib	615.4
0.28	0.41	0.69	369100	99011-02-6	Imiquimod	240.31
0.36	0.44	0.82	616348	100286-90-6	Irinotecan hydrochloride	623.15
0.42	0.44	0.95	226080	53123-88-9	Sirolimus	914.18
0.41	0.46	0.89	776422	1032900-25-6	Ceritinib	558.14
0.56	0.50	1.12	764134	1195768-06-9	Dabrafenib mesylate	615.65
0.37	0.55	0.68	756645	877399-52-5	Crizotinib	450.34
0.36	0.59	0.62	125066	9041-93-4	Bleomycin sulfate	1512.61
0.94	0.60	1.55	256942	56390-09-1	Epirubicin hydrochloride	579.99
0.25	0.64	0.40	266046	61825-94-3	Oxaliplatin	397.29
1.03	0.64	1.60	141540	33419-42-0	Etoposide	588.56
0.44	0.67	0.66	123127	25316-40-9	Doxorubicin hydrochloride	579.99
0.43	0.69	0.62	8806	3223-07-2	Melphalan hydrochloride	341.66

0.66	0.71	0.93	683864	162635-04-3	Temsirolimus	1030.29
0.32	0.73	0.44	296961	20537-88-6	Amifostine	214.22

0.70	0.81	0.87	761388	110078-46-1	Plerixafor	502.79
0.46	0.83	0.55	745750	231277-92-2	Lapatinib	581.06
0.62	0.87	0.71	180973	54965-24-1	Tamoxifen citrate	563.65
0.68	0.89	0.77	733504	159351-69-6	Everolimus	958.24
0.56	0.93	0.61	765694	380843-75-4	Bosutinib	530.45
0.69	0.95	0.73	9706	51-18-3	Triethylenemelamine	204.23
0.37	0.97	0.38	721517	118072-93-8	Zoledronic acid	272.09
0.75	1.00	0.74	749226	154229-19-3	Abiraterone	349.51
0.66	1.01	0.65	BIA Ctrl			
0.67	1.07	0.63	761068	849217-68-1	Cabozantinib	501.51
0.83	1.11	0.74	246131	56124-62-0	Valrubicin	723.64
0.74	1.14	0.65	702294	52205-73-9	Estramustine phosphate sodium	564.35
0.56	1.17	0.48	758487	943319-70-8	Ponatinib	532.55

References

1. Parikh K, Sait SF. Pediatric CNS tumors: Overview and treatment paradigms. *Semin Pediatr Neurol.* 2025; 53:101186.

2. Ostrom QT, Cioffi G, Waite K, Kruchko C, Barnholtz-Sloan JS. CBTRUS Statistical Report: Primary Brain and Other Central Nervous System Tumors Diagnosed in the United States in 2014–2018. *Neuro-Oncology.* 2021; 23(Supplement_3):iii1–iii105.

3. Ostrom QT, de Blank PM, Kruchko C, et al. Alex's Lemonade Stand Foundation Infant and Childhood Primary Brain and Central Nervous System Tumors Diagnosed in the United States in 2007–2011. *Neuro-Oncology.* 2014; 16(suppl_10):x1–x36.

4. Yoel A, Adjumain S, Liang Y, Daniel P, Firestein R, Tsui V. Emerging and Biological Concepts in Pediatric High-Grade Gliomas. *Cells.* 2024 Sep 5; 13(17).

5. Buccoliero AM, Giunti L, Moscardi S, et al. Pediatric High Grade Glioma Classification Criteria and Molecular Features of a Case Series. *Genes (Basel).* 2022; 13(4).

6. Thorbinson C, Kilday J-P. Childhood Malignant Brain Tumors: Balancing the Bench and Bedside. *Cancers.* 2021; 13(23):6099.

7. Huang J, Yu J, Tu L, Huang N, Li H, Luo Y. Isocitrate Dehydrogenase Mutations in Glioma: From Basic Discovery to Therapeutics Development. *Front Oncol.* 2019; 9:506.

8. Vallero SG, Bertero L, Morana G, et al. Pediatric diffuse midline glioma H3K27- altered: A complex clinical and biological landscape behind a neatly defined tumor type. *Frontiers in Oncology.* 2023; Volume 12 - 2022.

9. Sturm D, Pfister SM, Jones DTW. Pediatric Gliomas: Current Concepts on Diagnosis, Biology, and Clinical Management. *J Clin Oncol.* 2017; 35(21):2370–2377.

10. Louis DN, Perry A, Wesseling P, et al. The 2021 WHO Classification of Tumors of the Central Nervous System: a summary. *Neuro Oncol.* 2021; 23(8):1231–1251.

11. Kim JW, Choi SA, Lee S, et al. Revisiting pediatric HGGs and PNETs according to the WHO CNS5 criteria: A clinical and genomic retrospective analysis. *Neurooncol Adv.* 2025; 7(1):vdaf175.

12. Kurokawa R, Baba A, Kurokawa M, et al. Neuroimaging features of diffuse hemispheric glioma, H3 G34-mutant: A case series and systematic review. *J Neuroimaging.* 2022; 32(1):17–27.

13. Tauziède-Espariat A, Debily MA, Castel D, et al. The pediatric supratentorial MYCN-amplified high-grade gliomas methylation class presents the same radiological, histopathological and molecular features as their pontine counterparts. *Acta Neuropathol Commun.* 2020; 8(1):104.

14. Tauziède-Espariat A, Debily MA, Castel D, et al. An integrative radiological, histopathological and molecular analysis of pediatric pontine histone-wildtype glioma with MYCN amplification (HGG-MYCN). *Acta Neuropathol Commun.* 2019; 7(1):87.

15. Park YW, Vollmuth P, Foltyn-Dumitru M, et al. The 2021 WHO Classification for Gliomas and Implications on Imaging Diagnosis: Part 2—Summary of Imaging Findings on Pediatric-Type Diffuse High-Grade Gliomas, Pediatric-Type Diffuse Low-Grade Gliomas, and Circumscribed Astrocytic Gliomas. *Journal of Magnetic Resonance Imaging.* 2023; 58(3):690–708.

16. Bagchi A, Chiang J, Pinto S, Dhanda S, Gajjar A. Infant-Type Hemispheric Gliomas: A

Review of Clinical, Radiologic, Histopathologic, and Molecular Features. *J Natl Compr Canc Netw.* 2025; 23(11).
17. Yoel A, Adjumain S, Liang Y, Daniel P, Firestein R, Tsui V. Emerging and Biological Concepts in Pediatric High-Grade Gliomas. *Cells.* 2024; 13(17).
18. Thomas BC, Staudt DE, Douglas AM, Monje M, Vitanza NA, Dun MD. CAR T cell therapies for diffuse midline glioma. *Trends in Cancer.* 2023; 9(10):791–804.
19. Vitanza N, Monje M. Diffuse intrinsic pontine glioma: from diagnosis to next-generation clinical trials. *Curr Treat Options Neurol.* 2019; 21:37.
20. Arms LM, Duchatel RJ, Jackson ER, Sobrinho PG, Dun MD, Hua S. Current status and advances to improving drug delivery in diffuse intrinsic pontine glioma. *Journal of Controlled Release.* 2024/06/01; 370.
21. Al Sharie S, Abu Laban D, Al-Hussaini M. Decoding Diffuse Midline Gliomas: A Comprehensive Review of Pathogenesis, Diagnosis and Treatment. *Cancers (Basel).* 2023; 15(19).
22. Buczkowicz P, Bartels U, Bouffet E, Becher O, Hawkins C. Histopathological spectrum of paediatric diffuse intrinsic pontine glioma: diagnostic and therapeutic implications. *Acta Neuropathologica.* 2014; 128(4):573–581.
23. Fisher P, Breiter S, Carson B, Wharam M, Williams J, Weingart J. A clinicopathologic reappraisal of brain stem tumor classification. Identification of pilocystic astrocytoma and fibrillary astrocytoma as distinct entities. *Cancer.* 2000; 89:1569–1576.
24. Louis D, Perry A, Reifenberger G, von Deimling A, Figarella-Branger D, Cavenee W. The 2016 World Health Organization Classification of Tumors of the Central Nervous System: a summary. *Acta Neuropathol.* 2016; 131:803–820.
25. Pfister SM, Reyes-Múgica M, Chan JKC, et al. A Summary of the Inaugural WHO Classification of Pediatric Tumors: Transitioning from the Optical into the Molecular Era. *Cancer Discovery.* 2022; 12(2):331–355.
26. El-Hashash AHK. Histone H3K27M Mutation in Brain Tumors. In: Fang D, Han J, eds. *Histone Mutations and Cancer*. Singapore: Springer Singapore; 2021:43–52.
27. Kluiver TA, Alieva M, van Vuurden DG, Wehrens EJ, Rios AC. Invaders Exposed: Understanding and Targeting Tumor Cell Invasion in Diffuse Intrinsic Pontine Glioma. *Front Oncol.* 2020; 10:92.
28. Kim HJ, Suh C-O. Radiotherapy for Diffuse Intrinsic Pontine Glioma: Insufficient but Indispensable. *Brain Tumor Research and Treatment.* 2023; 11(2):79–85.
29. Williams JR, Young CC, Vitanza NA, et al. Progress in diffuse intrinsic pontine glioma: advocating for stereotactic biopsy in the standard of care. *Neurosurgical Focus.* 2020; 48(1):E4.
30. Rashed WM, Maher E, Adel M, Saber O, Zaghloul MS. Pediatric diffuse intrinsic pontine glioma: where do we stand? *Cancer and Metastasis Reviews.* 2019; 38(4):759–770.
31. Robison NJ, Kieran MW. Diffuse intrinsic pontine glioma: a reassessment. *Journal of Neuro-Oncology.* 2014; 119(1):7–15.
32. Lassiter KR, Alexander E, Jr., Davis CH, Jr., Kelly DL, Jr. Surgical treatment of brain stem gliomas. *J Neurosurg.* 1971; 34(6):719–725.
33. Bradley KA, Zhou T, McNall-Knapp RY, et al. Motexafin-gadolinium and involved field radiation therapy for intrinsic pontine glioma of childhood: a children's oncology group phase 2 study. *Int J Radiat Oncol Biol Phys.* 2013; 85(1):e55–60.

34. Hargrave D, Bartels U, Bouffet E. Diffuse brainstem glioma in children: critical review of clinical trials. *Lancet Oncol.* 2006; 7(3):241–248.
35. Himes BT, Zhang L, Daniels DJ. Treatment Strategies in Diffuse Midline Gliomas With the H3K27M Mutation: The Role of Convection-Enhanced Delivery in Overcoming Anatomic Challenges. *Frontiers in Oncology.* 2019; Volume 9 - 2019.
36. Parsels LA, Wahl DR, Koschmann C, Morgan MA, Zhang Q. Developing H3K27M mutant selective radiosensitization strategies in diffuse intrinsic pontine glioma. *Neoplasia (New York, N.Y.).* 2023; 37:100881.
37. Khuong-Quang D-A, Buczkowicz P, Rakopoulos P, et al. K27M mutation in histone H3.3 defines clinically and biologically distinct subgroups of pediatric diffuse intrinsic pontine gliomas. *Acta Neuropathologica.* 2012; 124(3):439–447.
38. Schwartzentruber J, Korshunov A, Liu X-Y, et al. Driver mutations in histone H3.3 and chromatin remodelling genes in paediatric glioblastoma. *Nature.* 2012; 482(7384):226–231.
39. Lewis PW, Müller MM, Koletsky MS, et al. Inhibition of PRC2 activity by a gain-of-function H3 mutation found in pediatric glioblastoma. *Science (New York, N.Y.).* 2013; 340(6134):857–861.
40. Yang Y, Li G. Post-translational modifications of PRC2: signals directing its activity. *Epigenetics & Chromatin.* 2020; 13(1):47.
41. Wiles ET, Selker EU. H3K27 methylation: a promiscuous repressive chromatin mark. *Current opinion in genetics & development.* 2017; 43:31–37.
42. Jiao L, Liu X. Structural basis of histone H3K27 trimethylation by an active polycomb repressive complex 2. *Science (New York, N.Y.).* 2015; 350(6258):aac4383.
43. Bender S, Tang Y, Lindroth AM, et al. Reduced H3K27me3 and DNA hypomethylation are major drivers of gene expression in K27M mutant pediatric high-grade gliomas. *Cancer Cell.* 2013; 24(5):660–672.
44. Wierzbicki K, Ravi K, Franson A, et al. Targeting and Therapeutic Monitoring of H3K27M-Mutant Glioma. *Current Oncology Reports.* 2020; 22(2).
45. Lowe BR, Maxham LA, Hamey JJ, Wilkins MR, Partridge JF. Histone H3 Mutations: An Updated View of Their Role in Chromatin Deregulation and Cancer. *Cancers (Basel).* 2019; 11(5).
46. Taylor KR, Mackay A, Truffaux N, et al. Recurrent activating ACVR1 mutations in diffuse intrinsic pontine glioma. *Nature Genetics.* 2014; 46(5):457–461.
47. Venneti S, Kawakibi AR, Ji S, et al. TMET-02. CLINICAL EFFICACY OF ONC201 IN H3K27M-MUTANT DIFFUSE MIDLINE GLIOMAS IS DRIVEN BY DISRUPTION OF INTEGRATED METABOLIC AND EPIGENETIC PATHWAYS. *Neuro-Oncology.* 2023; 25(Supplement_5):v272–v272.
48. Gardner SL, Tarapore RS, Allen J, et al. Phase I dose escalation and expansion trial of single agent ONC201 in pediatric diffuse midline gliomas following radiotherapy. *Neurooncol Adv.* 2022; 4(1):vdac143.
49. Monje M, Mahdi J, Majzner R, et al. Intravenous and intracranial GD2-CAR T cells for H3K27M+ diffuse midline gliomas. *Nature.* 2025; 637(8046):708–715.
50. Nguyen AV, Soto JM, Gonzalez S-M, et al. H3G34-Mutant Gliomas—A Review of Molecular Pathogenesis and Therapeutic Options. *Biomedicines.* 2023; 11(7):2002.
51. Cartmill M, Punt J. Diffuse brain stem glioma. A review of stereotactic biopsies. *Childs*

Nerv Syst. 1999; 15(5):235–237; discussion 238.
52. Pincus DW, Richter EO, Yachnis AT, Bennett J, Bhatti MT, Smith A. Brainstem stereotactic biopsy sampling in children. *J Neurosurg.* 2006; 104(2 Suppl):108–114.
53. Roujeau T, Machado G, Garnett MR, et al. Stereotactic biopsy of diffuse pontine lesions in children. *J Neurosurg.* 2007; 107(1 Suppl):1–4.
54. Greuter L, Frank N, Guzman R, Soleman J. The Clinical Applications of Liquid Biopsies in Pediatric Brain Tumors: A Systematic Literature Review. *Cancers (Basel).* 2022; 14(11).
55. Noon A, Galban S. Therapeutic avenues for targeting treatment challenges of diffuse midline gliomas. *Neoplasia (New York, N.Y.).* 2023/06; 40.
56. Duca S, Parvar SJ, Kumeta L, et al. Drug delivery strategies for paediatric diffuse midline gliomas. *Advanced Drug Delivery Reviews.* 2025; 226:115695.
57. Gallitto M, Lazarev S, Wasserman I, et al. Role of radiation therapy in the management of diffuse intrinsic pontine glioma: a systematic review. *Advances in Radiation Oncology.* 2019; 4(3):520–531.
58. Mathew RK, Rutka JT. Diffuse Intrinsic Pontine Glioma : Clinical Features, Molecular Genetics, and Novel Targeted Therapeutics. *Journal of Korean Neurosurgical Society.* 2018; 61(3):343–351.
59. Warren KE. Beyond the Blood:Brain Barrier: The Importance of Central Nervous System (CNS) Pharmacokinetics for the Treatment of CNS Tumors, Including Diffuse Intrinsic Pontine Glioma. *Frontiers in Oncology.* 2018; 8:239.
60. Michalski A, Bouffet E, Taylor RE, et al. The addition of high-dose tamoxifen to standard radiotherapy does not improve the survival of patients with diffuse intrinsic pontine glioma. *Journal of Neuro-Oncology.* 2010; 100(1):81–88.
61. Jansen MHA, van Vuurden DG, Vandertop WP, Kaspers GJL. Diffuse intrinsic pontine gliomas: A systematic update on clinical trials and biology. *Cancer Treatment Reviews.* 2012; 38(1):27–35.
62. Rao JS. Molecular mechanisms of glioma invasiveness: the role of proteases. *Nature Reviews Cancer.* 2003; 3(7):489–501.
63. Heinonen T, Verfaillie C. Chapter 5.1 - The Development and Application of Key Technologies and Tools. In: Balls M, Combes R, Worth A, eds. *The History of Alternative Test Methods in Toxicology*: Academic Press; 2019:265–278.
64. Demuth T, Berens ME. Molecular Mechanisms of Glioma Cell Migration and Invasion. *Journal of Neuro-Oncology.* 2004; 70(2):217–228.
65. Wei X, Meel MH, Breur M, Bugiani M, Hulleman E, Phoenix TN. Defining tumor-associated vascular heterogeneity in pediatric high-grade and diffuse midline gliomas. *Acta Neuropathologica Communications.* 2021; 9:142.
66. Wang R, Sun S, Wang Z, et al. MCPIP1 promotes cell proliferation, migration and angiogenesis of glioma via VEGFA-mediated ERK pathway. *Experimental Cell Research.* 2022; 418(1):113267.
67. Onishi M, Ichikawa T, Kurozumi K, Date I. Angiogenesis and invasion in glioma. *Brain Tumor Pathology.* 2011; 28(1):13–24.
68. Kim S, Bell K, Mousa SA, Varner JA. Regulation of angiogenesis in vivo by ligation of integrin alpha5beta1 with the central cell-binding domain of fibronectin. *Am J Pathol.* 2000; 156(4):1345–1362.

69. Ollauri-Ibáñez C, Astigarraga I. Use of Antiangiogenic Therapies in Pediatric Solid Tumors. *Cancers (Basel).* 2021; 13(2).
70. Taylor J, Gerstner ER. Anti-angiogenic therapy in high-grade glioma (treatment and toxicity). *Curr Treat Options Neurol.* 2013; 15(3):328–337.
71. Beurel E, Grieco SF, Jope RS. Glycogen synthase kinase-3 (GSK3): regulation, actions, and diseases. *Pharmacology & therapeutics.* 2015; 148:114–131.
72. Zhao J, Wei M, Guo M, et al. GSK3: A potential target and pending issues for treatment of Alzheimer's disease. *CNS Neurosci Ther.* 2024; 30(7):e14818.
73. Ali A, Hoeflich KP, Woodgett JR. Glycogen Synthase Kinase-3: Properties, Functions, and Regulation. *Chemical Reviews.* 2001; 101(8):2527–2540.
74. Hoeflich KP, Luo J, Rubie EA, Tsao M-S, Jin O, Woodgett JR. Requirement for glycogen synthase kinase-3β in cell survival and NF-κB activation. *Nature.* 2000; 406(6791):86–90.
75. Force T, Woodgett JR. Unique and overlapping functions of GSK-3 isoforms in cell differentiation and proliferation and cardiovascular development. *J Biol Chem.* 2009; 284(15):9643–9647.
76. ter Haar E, Coll JT, Austen DA, Hsiao H-M, Swenson L, Jain J. Structure of GSK3β reveals a primed phosphorylation mechanism. *Nature Structural Biology.* 2001; 8(7):593–596.
77. Fang X, Yu SX, Lu Y, Bast RC, Jr., Woodgett JR, Mills GB. Phosphorylation and inactivation of glycogen synthase kinase 3 by protein kinase A. *Proc Natl Acad Sci U S A.* 2000; 97(22):11960–11965.
78. Damodharan S, Lara-Velazquez M, Williamsen BC, Helgager J, Dey M. Diffuse Intrinsic Pontine Glioma: Molecular Landscape, Evolving Treatment Strategies and Emerging Clinical Trials. *Journal of Personalized Medicine.* 2022; 12(5):840.
79. Pedersen H, Schmiegelow K, Hamerlik P. Radio-Resistance and DNA Repair in Pediatric Diffuse Midline Gliomas. *Cancers.* 2020; 12(10):2813.
80. Wu YL, Maachani UB, Schweitzer M, et al. Dual Inhibition of PI3K/AKT and MEK/ERK Pathways Induces Synergistic Antitumor Effects in Diffuse Intrinsic Pontine Glioma Cells. *Translational Oncology.* 2017; 10(2):221–228.
81. Cross DAE, Alessi DR, Cohen P, Andjelkovich M, Hemmings BA. Inhibition of glycogen synthase kinase-3 by insulin mediated by protein kinase B. *Nature.* 1995; 378(6559):785–789.
82. Pai SG, Carneiro BA, Mota JM, et al. Wnt/beta-catenin pathway: modulating anticancer immune response. *Journal of Hematology & Oncology.* 2017; 10(1).
83. Nowicki MO, Dmitrieva N, Stein AM, et al. Lithium inhibits invasion of glioma cells; possible involvement of glycogen synthase kinase-3. *Neuro-Oncology.* 2008; 10(5):690–699.
84. Sun Y, Bailey CP, Sadighi Z, Zaky W, Chandra J. Pediatric high-grade glioma: aberrant epigenetics and kinase signaling define emerging therapeutic opportunities. *J Neurooncol.* 2020; 150(1):17–26.
85. Duchatel RJ, Savary C, Germon ZP, et al. Beyond base camp: PI3K/mTOR inhibition for the treatment of pediatric high-grade gliomas. *Neuro Oncol.* 2025; 27(11):2789–2803.
86. Skinner KR, Koga T, Miki S, et al. Cooperativity between H3.3K27M and PDGFRA poses multiple therapeutic vulnerabilities in human iPSC-derived diffuse midline glioma

avatars. *bioRxiv.* 2023.
87. Alves M, Borges DdP, Kimberly A, et al. Glycogen Synthase Kinase-3 Beta Expression Correlates With Worse Overall Survival in Non-Small Cell Lung Cancer—A Clinicopathological Series. *Frontiers in Oncology.* 2021; Volume 11 - 2021.
88. Wu D, Pan W. GSK3: a multifaceted kinase in Wnt signaling. *Trends Biochem Sci.* 2010; 35(3):161–168.
89. McCubrey JA, Steelman LS, Bertrand FE, et al. GSK-3 as potential target for therapeutic intervention in cancer. *Oncotarget.* 2014; 5(10):2881–2911.
90. Brüning-Richardson A, Shaw GC, Tams D, et al. GSK-3 Inhibition Is Cytotoxic in Glioma Stem Cells through Centrosome Destabilization and Enhances the Effect of Radiotherapy in Orthotopic Models. *Cancers (Basel).* 2021; 13(23).
91. Kotliarova S, Pastorino S, Kovell LC, et al. Glycogen synthase kinase-3 inhibition induces glioma cell death through c-MYC, nuclear factor-kappaB, and glucose regulation. *Cancer Res.* 2008; 68(16):6643–6651.
92. Cockle JV, Picton S, Levesley J, et al. Cell migration in paediatric glioma; characterisation and potential therapeutic targeting. *Br J Cancer.* 2015; 112(4):693–703.
93. Jimenez-Macias JL, Vaughn-Beaucaire P, Bharati A, et al. Modulation of blood-tumor barrier transcriptional programs improves intratumoral drug delivery and potentiates chemotherapy in GBM. *Sci Adv.* 2025; 11(9):eadr1481.
94. Miyashita K, Kawakami K, Nakada M, et al. Potential Therapeutic Effect of Glycogen Synthase Kinase 3β Inhibition against Human Glioblastoma. *Clinical Cancer Research.* 2009; 15(3):887–897.
95. Bhat RV, Andersson U, Andersson S, Knerr L, Bauer U, Sundgren-Andersson AK. The Conundrum of GSK3 Inhibitors: Is it the Dawn of a New Beginning? *Journal of Alzheimer's Disease.* 2018; 64(s1):S547–S554.
96. Cohen P, Goedert M. GSK3 inhibitors: development and therapeutic potential. *Nature Reviews Drug Discovery.* 2004; 3(6):479–487.
97. Rinnab L, Schütz SV, Diesch J, et al. Inhibition of glycogen synthase kinase-3 in androgen-responsive prostate cancer cell lines: are GSK inhibitors therapeutically useful? *Neoplasia.* 2008; 10(6):624–634.
98. Brail LH, Gray JE, Burris H, et al. A phase I dose-escalation, pharmacokinetic (PK), and pharmacodynamic (PD) evaluation of intravenous LY2090314 a GSK3 inhibitor administered in combination with pemetrexed and carboplatin. *Journal of Clinical Oncology.* 2011; 29(15_suppl):3030–3030.
99. Pecoraro C, Faggion B, Balboni B, et al. GSK3β as a novel promising target to overcome chemoresistance in pancreatic cancer. *Drug Resistance Updates.* 2021; 58:100779.
100. Chen S, Sun K-X, Feng M-X, Sang X-B, Liu B-L, Zhao Y. Role of glycogen synthase kinase-3β inhibitor AZD1080 in ovarian cancer. *Drug Design, Development and Therapy.* 2016; 10(null):1225–1232.
101. Ding L, Madamsetty VS, Kiers S, et al. Glycogen Synthase Kinase-3 Inhibition Sensitizes Pancreatic Cancer Cells to Chemotherapy by Abrogating the TopBP1/ATR-Mediated DNA Damage Response. *Clinical Cancer Research.* 2019; 25(21):6452–6462.
102. Mackay A, Burford A, Carvalho D, et al. Integrated Molecular Meta-Analysis of 1,000 Pediatric High-Grade and Diffuse Intrinsic Pontine Glioma. *Cancer Cell.* 2017; 32(4):520–537.e525.

103. Shankar G. M, Alex VV, Nisthul A. A, et al. Pre-clinical evidences for the efficacy of tryptanthrin as a potent suppressor of skin cancer. *Cell Proliferation.* 2020; 53(1):e12710.
104. Tu P, Tian R, Lu Y, et al. Beneficial effect of Indigo Naturalis on acute lung injury induced by influenza A virus. *Chinese Medicine.* 2020; 15(1):128.
105. Pharmacological properties of indirubin and its derivatives. *Biomedicine & Pharmacotherapy.* 2022/07/01; 151.
106. Williams SP, Nowicki MO, Liu F, et al. Indirubins Decrease Glioma Invasion by Blocking Migratory Phenotypes in Both the Tumor and Stromal Endothelial Cell Compartments. *Cancer Research.* 2011; 71(16):5374–5380.
107. Nam S, Buettner R, Turkson J, et al. Indirubin derivatives inhibit Stat3 signaling and induce apoptosis in human cancer cells. *Proceedings of the National Academy of Sciences.* 2005; 102(17):5998–6003.
108. Perabo FG, Frössler C, Landwehrs G, et al. Indirubin-3'-monoxime, a CDK inhibitor induces growth inhibition and apoptosis-independent up-regulation of survivin in transitional cell cancer. *Anticancer Res.* 2006; 26(3a):2129–2135.
109. Marko D, Schätzle S, Friedel A, et al. Inhibition of cyclin-dependent kinase 1 (CDK1) by indirubin derivatives in human tumour cells. *British Journal of Cancer.* 2001; 84(2):283–289.
110. Hoessel R, Leclerc S, Endicott JA, et al. Indirubin, the active constituent of a Chinese antileukaemia medicine, inhibits cyclin-dependent kinases. *Nature Cell Biology.* 1999; 1(1):60–67.
111. Sethi G, Ahn KS, Sandur SK, Lin X, Chaturvedi MM, Aggarwal BB. Indirubin Enhances Tumor Necrosis Factor-induced Apoptosis through Modulation of Nuclear Factor-κB Signaling Pathway *. *Journal of Biological Chemistry.* 2006; 281(33):23425–23435.
112. Scobie MR, Houke HR, Rice CD. Modulation of glioma-inflammation crosstalk profiles in human glioblastoma cells by indirubin-3'-(2,3 dihydroxypropyl)-oximether (E804) and 7-bromoindirubin-3′-oxime (7BIO). *Chemico-Biological Interactions.* 2019; 312:108816.
113. Zdioruk M, Jimenez-Macias JL, Nowicki MO, et al. PPRX-1701, a nanoparticle formulation of 6'-bromoindirubin acetoxime, improves delivery and shows efficacy in preclinical GBM models. *Cell Rep Med.* 2023; 4(5):101019.
114. Leclerc S, Garnier M, Hoessel R, et al. Indirubins Inhibit Glycogen Synthase Kinase-3β and CDK5/P25, Two Protein Kinases Involved in Abnormal Tau Phosphorylation in Alzheimer's Disease. *Journal of Biological Chemistry.* 2001; 276:251–260.
115. Babcock AS, Anderson AL, Rice CD. Indirubin-3′-(2,3 dihydroxypropyl)-oximether (E804) is a potent modulator of LPS-stimulated macrophage functions. *Toxicology and Applied Pharmacology.* 2013; 266(1):157–166.
116. Eldar-Finkelman H, Martinez A. GSK-3 Inhibitors: Preclinical and Clinical Focus on CNS. *Frontiers in Molecular Neuroscience.* 2011; 4.
117. Blažević T, Heiss EH, Atanasov AG, Breuss JM, Dirsch VM, Uhrin P. Indirubin and Indirubin Derivatives for Counteracting Proliferative Diseases. *Evidence-Based Complementary and Alternative Medicine.* 2015; 2015:654098.
118. Wang X, Liu Z. Prevention and treatment of viral respiratory infections by traditional Chinese herbs. *Chinese Medical Journal.* 2014; 127(7):1344–1350.
119. Korur S, Huber RM, Sivasankaran B, et al. GSK3β Regulates Differentiation and Growth

Arrest in Glioblastoma. *PLOS ONE.* 2009; 4(10):e7443.
120. Kaufmann L, Marinescu G, Nazarenko I, et al. LiCl induces TNF-α and FasL production, thereby stimulating apoptosis in cancer cells. *Cell Commun Signal.* 2011; 9:15.
121. Song L, Zhou T, Jope RS. Lithium facilitates apoptotic signaling induced by activation of the Fas death domain-containing receptor. *BMC Neurosci.* 2004; 5:20.
122. Baeza-Yates R, Sangal PM, Villoslada P. Burden of neurological diseases in the US revealed by web searches. *PLoS One.* 2017; 12(5):e0178019.
123. Hersh DS, Wadajkar AS, Roberts N, et al. Evolving Drug Delivery Strategies to Overcome the Blood Brain Barrier. *Curr Pharm Des.* 2016; 22(9):1177–1193.
124. Wu D, Chen Q, Chen X, Han F, Chen Z, Wang Y. The blood-brain barrier: structure, regulation, and drug delivery. *Signal Transduct Target Ther.* 2023; 8(1):217.
125. Sugiyama S, Sasaki T, Tanaka H, et al. The tight junction protein occludin modulates blood-brain barrier integrity and neurological function after ischemic stroke in mice. *Sci Rep.* 2023; 13(1):2892.
126. Stamatovic SM, Johnson AM, Keep RF, Andjelkovic AV. Junctional proteins of the blood-brain barrier: New insights into function and dysfunction. *Tissue Barriers.* 2016; 4(1):e1154641.
127. Arvanitis CD, Ferraro GB, Jain RK. The blood-brain barrier and blood-tumour barrier in brain tumours and metastases. *Nat Rev Cancer.* 2020; 20(1):26–41.
128. Arvanitis CD, Ferraro GB, Jain RK. The blood–brain barrier and blood–tumour barrier in brain tumours and metastases. *Nature reviews. Cancer.* 2019 Oct 10; 20(1).
129. Mosteiro A, Pedrosa L, Ferrés A, Diao D, Sierra À, González JJ. The Vascular Microenvironment in Glioblastoma: A Comprehensive Review. *Biomedicines.* 2022; 10(6).
130. Wu S, Wang J, Liu J, et al. Programmed cell death 10 increased blood-brain barrier permeability through HMGB1/TLR4 mediated downregulation of endothelial ZO-1 in glioblastoma. *Cell Signal.* 2023; 107:110683.
131. Manoranjan B, Provias JP. β-Catenin marks proliferating endothelial cells in glioblastoma. *J Clin Neurosci.* 2022; 98:203–206.
132. Jimenez Macias JL, Vaughn-Beaucaire P, Yan J, Clark J, Lawler SE. Decoding the biology of the blood-brain tumor barrier in brain cancer. *Mol Cancer Res.* 2026.
133. Claesson-Welsh L, Dejana E, McDonald DM. Permeability of the Endothelial Barrier: Identifying and Reconciling Controversies. *Trends Mol Med.* 2021; 27(4):314–331.
134. Delgado-Bellido D, Zamudio-Martínez E, Fernández-Cortés M, et al. VE-Cadherin modulates β-catenin/TCF-4 to enhance Vasculogenic Mimicry. *Cell Death Dis.* 2023; 14(2):135.
135. Luo J, Wang Z, Zhang X, et al. Vascular Immune Evasion of Mesenchymal Glioblastoma Is Mediated by Interaction and Regulation of VE-Cadherin on PD-L1. *Cancers (Basel).* 2023; 15(17).
136. Banan R, Akbarian A, Samii M, et al. Diffuse midline gliomas, H3 K27M-mutant are associated with less peritumoral edema and contrast enhancement in comparison to glioblastomas, H3 K27M-wildtype of midline structures. *PLoS One.* 2021; 16(8):e0249647.
137. Wei X, Meel MH, Breur M, Bugiani M, Hulleman E, Phoenix TN. Defining tumor-associated vascular heterogeneity in pediatric high-grade and diffuse midline gliomas.

Acta Neuropathol Commun. 2021; 9(1):142.
138. El-Khouly FE, Haumann R, Breur M, et al. The neurovascular unit in diffuse intrinsic pontine gliomas. *Free Neuropathol.* 2021; 2:17.
139. Shaik S, Kennis B, Maegawa S, et al. REST upregulates gremlin to modulate diffuse intrinsic pontine glioma vasculature. *Oncotarget.* 2018; 9(4):5233–5250.
140. Soni, Walke V, Joshi D, Sharma T, Shrivastava A, Agrawal A. The spectrum of microvascular patterns in adult diffuse glioma and their correlation with tumor grade. *J Pathol Transl Med.* 2024; 58(3):127–133.
141. Wang B, Khan S, Wang P, et al. A Highly Selective GSK-3β Inhibitor CHIR99021 Promotes Osteogenesis by Activating Canonical and Autophagy-Mediated Wnt Signaling. *Front Endocrinol (Lausanne).* 2022; 13:926622.
142. Fernando D, Ahmed AU, Williams BRG. Therapeutically targeting the unique disease landscape of pediatric high-grade gliomas. *Front Oncol.* 2024; 14:1347694.
143. Xia J, Feng S, Zhou J, et al. GSK3 inhibitor suppresses cell growth and metabolic process in FLT3-ITD leukemia cells. *Med Oncol.* 2022; 40(1):44.
144. Hargrave D, Bartels U, Bouffet E. Diffuse brainstem glioma in children: critical review of clinical trials. *The Lancet Oncology.* 2006; 7(3):241–248.
145. Upton DH, Ung C, George SM, Tsoli M, Kavallaris M, Ziegler DS. Challenges and opportunities to penetrate the blood-brain barrier for brain cancer therapy. *Theranostics.* 2022; 12(10):4734–4752.
146. Steeg PS. The blood–tumour barrier in cancer biology and therapy. *Nature Reviews Clinical Oncology.* 2021; 18(11):696–714.
147. Perelroizen R, Philosof B, Budick-Harmelin N, et al. Astrocyte immunometabolic regulation of the tumour microenvironment drives glioblastoma pathogenicity. *Brain.* 2022; 145(9):3288–3307.
148. Cho C-F, Zhuang P, Scott B, et al. *Blood-tumor barrier organoids recapitulate glioblastoma microenvironment and enable high-throughput modeling of therapeutic delivery*2024.
149. Haddad AF, Young JS, Amara D, et al. Mouse models of glioblastoma for the evaluation of novel therapeutic strategies. *Neurooncol Adv.* 2021; 3(1):vdab100.
150. Huang C, Xin X, Hao X, et al. Construction of a whole-brain panorama for glioma vasculature reveals tumor heterogeneity and blood-brain barrier disruption. *Sci Adv.* 2025; 11(30):eadw8330.
151. Lonser RR, Walbridge S, Vortmeyer AO, et al. Induction of glioblastoma multiforme in nonhuman primates after therapeutic doses of fractionated whole-brain radiation therapy. *J Neurosurg.* 2002; 97(6):1378–1389.
152. Umans RA, Ten Kate M, Pollock C, Sontheimer H. Fishing for Contact: Modeling Perivascular Glioma Invasion in the Zebrafish Brain. *ACS Pharmacol Transl Sci.* 2021; 4(4):1295–1305.
153. Hicks WH, Bird CE, Pernik MN, et al. Large Animal Models of Glioma: Current Status and Future Prospects. *Anticancer Res.* 2021; 41(11):5343–5353.
154. Puchalski RB, Shah N, Miller J, et al. An anatomic transcriptional atlas of human glioblastoma. *Science.* 2018; 360(6389):660–663.
155. Dusart P, Hallström BM, Renné T, Odeberg J, Uhlén M, Butler LM. A Systems-Based Map of Human Brain Cell-Type Enriched Genes and Malignancy-Associated Endothelial

Changes. *Cell Rep.* 2019; 29(6):1690–1706.e1694.
156. Hoogstrate Y, Draaisma K, Ghisai SA, et al. Transcriptome analysis reveals tumor microenvironment changes in glioblastoma. *Cancer Cell.* 2023; 41(4):678–692.e677.
157. Wälchli T, Ghobrial M, Schwab M, et al. Single-cell atlas of the human brain vasculature across development, adulthood and disease. *Nature.* 2024; 632(8025):603–613.
158. McDannold N, Wen PY, Reardon DA, Fletcher SM, Golby AJ. Cavitation monitoring, treatment strategy, and acoustic simulations of focused ultrasound blood-brain barrier disruption in patients with glioblastoma. *J Control Release.* 2024; 372:194–208.
159. Wu CC, Szalontay L, Pouliopoulos AN, et al. Blood-brain barrier opening with neuronavigation-guided focused ultrasound in pediatric patients with diffuse midline glioma. *Sci Transl Med.* 2025; 17(824):eadq6645.
160. Cho C-F, Wolfe JM, Fadzen CM, et al. Blood-brain-barrier spheroids as an in vitro screening platform for brain-penetrating agents. *Nature Communications.* 2017; 8(1):15623.
161. van Tilburg CM, Milde T, Witt R, et al. Phase I/II intra-patient dose escalation study of vorinostat in children with relapsed solid tumor, lymphoma, or leukemia. *Clinical Epigenetics.* 2019; 11(1):188.
162. Wawruszak A, Borkiewicz L, Okon E, Kukula-Koch W, Afshan S, Halasa M. Vorinostat (SAHA) and Breast Cancer: An Overview. *Cancers.* 2021; 13(18):4700.
163. Sawa H, Murakami H, Ohshima Y, et al. Histone deacetylase inhibitors such as sodium butyrate and trichostatin A induce apoptosis through an increase of the bcl-2-related protein Bad. *Brain Tumor Pathology.* 2001; 18(2):109–114.
164. Wang ZM, Hu J, Zhou D, Xu ZY, Panasci LC, Chen ZP. Trichostatin A inhibits proliferation and induces expression of p21WAF and p27 in human brain tumor cell lines. *Ai Zheng.* 2002; 21(10):1100–1105.
165. Xu J, Sampath D, Lang FF, et al. Vorinostat modulates cell cycle regulatory proteins in glioma cells and human glioma slice cultures. *J Neurooncol.* 2011; 105(2):241–251.
166. Dickey A, Schleicher S, Leahy K, Hu R, Hallahan D, Thotala DK. GSK-3β inhibition promotes cell death, apoptosis, and in vivo tumor growth delay in neuroblastoma Neuro-2A cell line. *J Neurooncol.* 2011; 104(1):145–153.
167. Kuhns MA, Kalaycio M, Reu FJ, Maciejewski JP, Cheriyath V. GSK-3β Inhibitors In Overcoming Chemoresistance In Multiple Myeloma. *Blood.* 2010; 116(21):3009–3009.
168. Huang P, Plunkett W. Induction of apoptosis by gemcitabine. Paper presented at: Seminars in Oncology1995.
169. Bastiancich C, Bastiat G, Lagarce F. Gemcitabine and glioblastoma: challenges and current perspectives. *Drug Discovery Today.* 2018; 23(2):416–423.
170. Nabhan C, Gajria D, Krett NL, Gandhi V, Ghias K, Rosen ST. Caspase activation is required for gemcitabine activity in multiple myeloma cell lines. *Mol Cancer Ther.* 2002; 1(13):1221–1227.
171. Cottin S, Ghani K, de Campos-Lima PO, Caruso M. Gemcitabine intercellular diffusion mediated by gap junctions: new implications for cancer therapy. *Molecular Cancer.* 2010; 9(1):141.
172. Carpinelli G, Bucci B, D'Agnano I, et al. Gemcitabine treatment of experimental C6 glioma: the effects on cell cycle and apoptotic rate. *Anticancer Res.* 2006; 26(4b):3017–3024.

173. Kim MM, Camelo-Piragua S, Schipper M, et al. Gemcitabine Plus Radiation Therapy for High-Grade Glioma: Long-Term Results of a Phase 1 Dose-Escalation Study. *Int J Radiat Oncol Biol Phys.* 2016; 94(2):305–311.

174. He Q, Liu J, Liang J, et al. Towards Improvements for Penetrating the Blood–Brain Barrier—Recent Progress from a Material and Pharmaceutical Perspective. *Cells.* 2018; 7(4):24.